HIGH EFFICIENCY PERFLUOROCYCLOBUTYL AIR-TRENCH SPLITTERS FOR USE IN COMPACT RING RESONATORS

by

NAZLI RAHMANIAN

A DISSERTATION

Submitted in partial fulfillment of the requirements
for the degree of Doctor of Philosophy
in
The Optical Science and Engineering Program
to
The School of Graduate Studies
of
The University of Alabama in Huntsville

HUNTSVILLE, ALABAMA

2007

In presenting this dissertation in partial fulfillment of the requirements for a doctoral degree from The University of Alabama in Huntsville, I agree that the Library of this University shall make it freely available for inspection. I further agree that permission for extensive copying for scholarly purposes may be granted by my advisor or, in his/her absence, by the Director of the Program or the Dean of the School of Graduate Studies. It is also understood that due recognition shall be given to me and to The University of Alabama in Huntsville in any scholarly use which may be made of any material in this dissertation.

_________________________ __________

(student signature) (date)

DISSERTATION APPROVAL FORM

Submitted by Nazli Rahmanian in partial fulfillment of the requirements for the degree of Doctor of Philosophy in Optical Science and Engineering and accepted on behalf of the Faculty of the School of Graduate Studies by the dissertation committee.

We, the undersigned members of the Graduate Faculty of The University of Alabama in Huntsville, certify that we have advised and/or supervised the candidate on the work described in this dissertation. We further certify that we have reviewed the dissertation manuscript and approve it in partial fulfillment of the requirements for the degree of Doctor of Philosophy in Optical Science & Engineering.

______________________________ Committee Chair

____

____

____

____

____

______________________________ Program Director

______________________________ College Dean

______________________________ Graduate Dean

ABSTRACT
School of Graduate Studies
The University of Alabama in Huntsville

Degree Doctor of Philosophy Program Optical Science and Engineering

Name of Candidate Nazli Rahmanian

Title High Efficiency Perfluorocyclobutyl Air-trench Splitters for Use in Compact Ring Resonators

Planar lightwave circuits with higher integration, lower cost, and added functionality can reduce costs in optical network components. To facilitate large scale integration of planar lightwave circuits the size of their fundamental building blocks such as splitters and bends needs to be reduced.

In this dissertation compact air trench splitters are demonstrated in perfluorocyclobutyl (PFCB) polymers. To realize these high efficiency splitters we have developed a very high aspect ratio (18:1) anisotropic PFCB etch for submicron features using a CO/O_2 etch chemistry in an inductively coupled plasma reactive ion etcher (ICP-RIE). A low loss of 0.45 dB/splitter (90.1% efficiency) has been measured on splitters fabricated on silicon substrates. The etch process was successfully transferred to Ultem substrates to reduce the effects of the coefficient of thermal expansion (CTE) mismatch between PFCB and silicon.

An ultra-compact ring resonator was demonstrated in PFCB with a splitting ratio of 85% to 15% (85-15) air-trench splitters and air-trench bends. The ring resonator size is only 70 μm x 100 μm. Measurements show a 7.2 nm free spectral range (FSR) in agreement with 2 dimensional finite difference time domain (2-D FDTD) simulation results. A 1.8 nm full width at half maximum

(FWHM) and ~10 dB insertion loss for the drop port was measured. The source of loss is explained with comparison to analytical calculations and measurement results. The ring resonator size is reduced by a factor of 1700 compared to a traditionally designed RR in the same material system due to the size reduction provided by the air-trench splitters and bends.

Abstract Approval: Committee Chair __________________________________
(Date)

Program Director __________________________________

Graduate Dean __________________________________

ACKNOWLEDGMENTS

I would like to thanks my advisor, Dr. Gregory Nordin, for his guidance and support throughout my academic studies. I thank him for everything he taught me and for the wonderful person that he is. I also would like to thank Dr. Robert Lindquist for his help and support. His support in the past year has been very important to me and the progress of my project. I also am very grateful to all my committee members for their valuable guidance and time. Very special thanks goes to Dr. Seunghyun Kim for being a good friend and always being ready for a scientific discussion. Additionally, I am thankful to all the students and staff at the Nano and Micro Devices Center (NMDC) at UAH.

I would like to thank my parents from the bottom of my heart for their love and support. I thank them for providing the best education for me in the hardest of times and for always loving and believing in me. They have always been my source of strength. I thank my Mom for traveling so long to be here with me for my graduation. I also thank my brother for being so amazing in everything, reminding me that if I look and search hard, I might find the same genes in me!

Finally I would like to thank Gevara, my best friend and my husband, for his love and for believing that I can do anything. None of this would have been possible without him.

The work presented in this dissertation was supported in part by DARPA Grant N66001-04-8933.

TABLE OF CONTENTS

Page

LIST OF FIGURES x

LIST OF TABLES xiv

Chapter

1 INTRODUCTION 1

1.1 Motivation 1

1.2 Dissertation Overview 3

1.3 New Contributions 4

2 BACKGROUND 5

2.1 PFCB Material 5

2.2 Plasma Etch Theory and Background 7

2.3 EBL on Top of PFCB Stack Process 10

2.4 Waveguide Beam Splitters 11

2.5 Ring Resonators 15

3 PFCB Small Feature Etch Development on Silicon Substrate 18

3.1 Introduction 19

3.2 SFE Development with Optically Patterned Features 23

3.2.1 SF6/O2 Etch 23

3.2.2 CO/O2 Etch 25

3.3 Etch Process for Electron Beam Patterned Features 28

3.4 Stress Induced Lateral Widening 32

3.5 Conclusion 37

4 PFCB Small Feature Etch Development on Ultem Substrate 38

4.1 Introduction 38

4.2 Ultem Substrate Preparation..39

4.3 Aluminum Etch Development..40

4.4 PFCB etch development..46

4.5 Conclusion...50

5 Ultra Compact PFCB Air-Trench Waveguide Beam Splitter on Silicon Substrate 51

5.1 Introduction 51

5.2 Air-trench Splitter Analysis...52

5.3 Splitter Mask design and Fabrication 58

5.4 950 nm Wide Splitter Measurement...72

5.5 Conclusion...75

6 Ultra Compact RR Fabrication and Characterization...77

6.1 Introduction 77

6.2 Ring Resonator Analysis 78

6.3 Ring Resonator Fabrication and Measurement 84

6.3.1 Core on Clad 173_Die0..85

6.3.2 Core on Clad 179_Die7..89

6.4 Measurement Comparison to Analytical Result...91

6.4.1 Resonance Frequency and FSR 92

6.4.2 RR Spectral Response as a Function of Splitter and Bend Performance 93

6.5 Conclusion...100

7 Summary and Future Research...102

7.1 Summary 102

7.2 Future Research..104

7.2.1 Small Feature Etch 104

7.2.2 Air-trench Splitter...104

7.2.3 Ultra-compact Ring Resonator and MZI ... 105

Appendix A: PFCB Initial Process Development and Propagation Loss Measurement ... 107

A.1 Introduction ... 107

A.2 PFCB Film Characterization ... 108

A.2.1 Initial Film Process Development ... 109

A.2.2 Refractive Index and Thickness Measurement ... 110

A.3 PFCB Loss Measurement Device Fabrication ... 113

A.3.1 Loss Measurement method ... 114

A.3.2 Racetrack Waveguide Fabrication ... 115

A.4 Measurement Set up and Error Calibration ... 126

A.5 Loss Measurement ... 128

A.6 Conclusion ... 133

Appendix B: PFCB Air-trench Splitter Fabrication Process ... 134

REFERENCES ... 136

LIST OF FIGURES

Figure Page

2.1 Measured attenuation versus wavelength for TVE PFCB [11] 6
2.2 Typical etch profile obtained by etching in oxygen (a) isotropic profile (b) vertical profile with residual lateral etching (c) perfect anisotropic profile[12]...................... 8
2.3 Plasma etch mechanisms [13]... 9
2.4 Various waveguide beam splitter configurations proposed by researchers (a) traditional Y-branch splitter [16] (b) use of resonant cavities at the junction in HIC [19] (c) PhC airhole splitter in HIC [7] (d) SEM image of PhC airhole fabricated [7] (e) airtrenches and adiabatic tapering in LIC [21] (f) SEM image of fabricated device [21] (g) four port air-trench splitter in HIC [22] 14
3.1 PFCB chemical structure showing the polymer unit cell and the two chemical structures contained in the copolymers supplied to us by Tetramer Technologies, Inc.[32].. 22
3.2 Two dimensional finite difference time domain (2D-FDTD) simulation results at a wavelength of 1550 nm for an 800 nm wide, air trench as a 50:50 waveguide beam splitter. 2D simulation predicts a total optical efficiency of 98 % [8]...................... 22
3.3 Trenches etched with SF6/O2 etch (a) sideview of sidewall verticality (one trench wall was broken during cleave) (b) tilted top view showing the trench width......... 24
3.4 (a) passivation sidewall (b) grass on larger features... 25
3.5 The extreme cases of etching with (a) straight CO, with the rest etch parameters being the same. Excessive passivation. Low etch rate of 40nm/min. non-vertical sidewalls (b) straight O2, isotropic etching. bowing of the sidewall. Trench is wider on top . 26
3.6 SEM images of fully etched optically written trenches (a) cross sectional view showing 14 μm depth and vertical sidewalls (b) top view showing ~800 nm width 27
3.7 Aspect ratio dependent etch rate for PFCB with CO/O2 etch 28
3.8 Fabrication process schematic 30
3.9 Small feature in aluminum film after the aluminum etch. The rough layer on top is the remaining 31
3.10 SEM images of fully etched trenches (a) top view (b) tilted cross sectional view... 32
3.11 Extreme lateral widening and cracking at the ends on an isolated trench 33
3.12 Stress related widening of the outmost trenches in an etched comb pattern. All trenches had the same 250 nm starting width patterned by e-beam lithography. 34
3.13 Effect of stress relief trenches. (a) Three identically patterned trenches. (b) Half-length stress relief trenches (see text for discussion)... 35
3.14 stress relief feature distance effect on widening with trenches placed at (a) 35 μm (b) uneven at 15 and 30 (c) at 15 μm.. 36
4.1 Ultem surface optical microscope image at 5x magnification (a) before polishing (b) after polishing. 39
4.2 (a) successful Ultem dice (b) 10x microscope image of diced edge.......................... 40

4.3 Surface temperature measurement configuration on Ultem substrate 41
4.4 Sample burned at the corners during aluminum etch.. 42
4.5 After aluminum etch (a) 800 nm features fully etched (b) 300 nm features partially etched 43
4.6 Stepwise aluminum etch results on (a) 300 nm (b) 600 nm features.......................... 44
4.7 The PFCB etch result on Ultem without extra temperature control 46
4.8 SEM images of 800 nm features after full PFCB etch (a) tilted cross section (b) top view... 48
4.9 visual sidewall roughness comparison on 1.3 mm wide trenches etched on (a) Ultem substrate (b) silicon substrate... 49
5.1 Schematic of a narrow splitter to catch the evanescent tail of the beam 53
5.2 Multiple reflection and refractions on a dielectric slab when $\theta_1 < \theta_c$ 55
5.3 (a) Geometry of splitter design with an air trench. (b) Optical efficiencies at output waveguide channels 1 and 2 as a function of air trench width. 50/50 splitting ratio is achieved with 0.42μm air trench width [8].. 56
5.4 (a) Magnitude squared time averaged electric field of a splitter design for ring resonator at λ=1.55μm (TM polarization). Air trench width is 0.8μm. (b) Spectral response of the splitter design [8]. 57
5.5 (a) Magnitude squared time averaged electric field of a splitter for a Mach-Zender interferometer at λ=1.55μm (TM polarization). The air trench width is 0.8μm and the angle between Channels 1 & 2 is 107.5 degrees. (b) Spectral response of the splitter [8]... 58
5.6 Reflection and transmission measurement layouts.. 59
5.7 Loss versus number of splitters for (a) 80-20 transmission configuration (b) 50-50 splitter configuration... 60
5.8 (a) protect mask (b) waveguide mask (c) opening mask (d) example of a die layout 62
5.9 Optical microscope images of fabricated sample (a) after patterning with PROTECT mask (b) after lift off (c) after patterning with WAVEGUIDE mask (d) e-beam alignment marks after patterning WAVEGUIDE (d) after etching core (e) after patterning with OPEN ING mask and aluminum etch.. 65
5.10 Cracking and over etching of the openings in 400 x 400 μm exposure field The cracking problem was still damaging to the waveguide, with larger exposure field.66
5.11 ZEP cracking problem as problem solving progress (a) with 80 nm evaporated aluminum (b) with 35 nm sputtered Al (c) 90 nm sputtered Al (d) 80 nm sputtered Al with pre-spin step eliminated (e) same as “d” with 95 nm sputtered Al (f) previous improvement plus reduced developing time. 68
5.12 openings are over-etched as ZEP film etches away during an attempt to fully etch a thick aluminum film.. 69
5.13 optical microscope images to pinpoint the appearance of pinholes (a) after sputtering 90 nm Al (b) after ZEP was spun (c) dense pinholes after 30 min bake at 170°C (d) Tilted top SEM image of the same sample showing the ZEP surface and the aluminum cross section through a crack: no sign on problem on ZEP surface .. 70
5.14 Temperature effect on pinhole density (a) less pinholes on sample baked at 140°C (b) appearance of pinhole after full trench etch (c) almost no pinholes on sample baked at 100°C (d) after aluminum etch: low ZEP resistance on sample baked at 100°C.. 71

5.15 Splitter efficiency measurement (a) reflection efficiency (b) transmission efficiency. Note that error bars on the measured data are smaller than the marker size. 73
5.16 Air-trench splitting ratio as a function of air-trench width: 2-D FDTD results in solid line and measured data points in green. 74
6.1 Geometry of a waveguide bend with an air trench. The position of the incident waveguide mode source is shown as well as the detector position along the output waveguide [8]... 79
6.2 Proposed ring resonator combining small-area bends and splitters with air trenches [8]. 80
6.3 Angular spectrum. Vertical line corresponds to plane wave components at the critical angle for 60 degree bend structure [8]. 80
6.4 (a) Bend efficiency as a function of S. Bend efficiency at S=-0.326μm is 99.3%. (b) Bend efficiency as a function of air trench width [8]. 81
6.5 (a) Geometry and magnitude squared time averaged electric field of the final 60 degree bend design at λ=1.55μm (TM polarization). (b) Spectral response (Inset magnify the calculated data region to show the data clearly) [8] 82
6.6 Spectral response of RR for the wavelength range of 1.52μm – 1.60μm (TM polarization) [8]. 83
6.7 Magnitude squared time averaged electric fields at (a) λ=1.5513μm (one of drop wavelengths) and (b) λ=1.5549μm (one of throughput wavelengths) [8]. 83
6.8 Optical microscope image (DIC mode) of the measured ring resonator 85
6.9 First ring resonator output power spectrum at (a) drop port (b) throughput port 86
6.10 Fabrication problems responsible for high losses in RR (a) poor line quality for splitter and mis-shaped and larger than desired bends (b) air-trench splitter line and etch quality (c) stress relief trenches coming too close to the waveguide 88
6.11 Optical microscope image of (a) RR1 (b) RR2 and (c) RR3 89
6.12 RR1 measured power (a) drop port (b) throughput port 90
6.13 RR2 measured power (a) drop port (b) throughput port 90
6.14 RR3 measured power (a) drop port (b) throughput port 91
6.15 Drop and throughput port performance for ideal and less than perfect splitter and bend efficiency. 94
6.16 High and low of ring resonator drop and throughput port efficiency as a function of (a) splitter efficiency (b) bend efficiency.. 95
6.17 RR1 drop port power (a) measured (b) calculated.. 97
6.18 RR1 drop port power (a) measured (b) calculated.. 98
6.19 calculated power for a 95% overall efficiency for splitters and bends (a) drop port (b) throughput port (c) both ports 100
A.1 progress of film quality (a) the first batch of PFCB (cloudy solution) (b) after solution was heated and stirred (c) new batch with some shrinking at the edges (d) higher molecular weight solution solving the shrinking problem 110
A.2 Racetrack pattern: includes 9 straight waveguides in the input side, 9 in the output side and 9 racetracks in the middle 115
A.3 PFCB racetrack fabrication process plan 119
A.4 PFCB core after PFCB etch (a) cross section (b) top view..................................... 121
A.5 Fabricated PFCB racetrack on silicon substrate 122
A.6 PFCB delamination during developing... 123

A.7 SEM images of (a) SiO2 etched profile before pulsed etch was used (b) tilted top image etch profile after changing to etch to pulsed 124
A.8 Examples of different defects observed on the race track waveguides (a) broken waveguide, lithography problem (b) jagged edges and deformation, lithography problem (c) particle on the cladding with focus on particle (d) same as c with focus on waveguide 125
A.9 Measurement set up schematic 127
A.10 Set up for input polarization adjustment 129
A.11 Racetrack output mode detected by IR camera 130
A.12 Measured racetrack IR top images and some defects causing them (a) IR top image of racetrack (b)lithography problem (c) particle on over cladding with focus on surface (d) particle on over cladding with focus on the waveguide 131
A.13 Racetrack 4 IR top image and the defect causing big spray of light(a) IR top image of racetrack (a) broken waveguide causing the big splash of light......................... 132
A.14 IR top image of straight waveguide (a) no IMF on top (b) a drop of IMF on waveguide coupling out light... 133

LIST OF TABLES

Table Page

4.1 Surface temperature measured on silicon and Ultem with different platen temperatures 42
4.2 surface temperature during aluminum etch after reducing coil power to 300 W 44
4.3 surface temperature during PFCB etch after reducing platen temperature to 10^oC.... 47
A.1 Refractive index measurement experiments for core and clad at 1550 nm wavelength (both TE and TM polarization) 112
A.2 Curing experiments to fix Δn at about 1 % 117

CHAPTER ONE

INTRODUCTION

1.1 Motivation

Planar lightwave devices have been the subject of a lot of research in recent years. Decreasing the size of these devices continues to be an important issue since it is advantageous to integrate as many components as possible on a single chip. The size of planar lightwave circuits (PLCs) is usually limited by the area needed to make waveguide bends or splitters. Devices such as ring resonatorS (RR) and Mach-Zender interferometers (MZIs), which are widely used as components in add/drop and bandpass filters, optical switches and multiplexer/demultiplexers [1-4], consist of a combination of bends and splitters. The bend radius can be decreased by using high refractive index contrast (HIC) core and clad materials because light propagating within HIC waveguides is well confined in the core region. However, HIC material systems fall short when it comes to propagation and fiber coupling losses. In low index contrast (LIC) material systems such as polymers, the minimum bend radius is several millimeters or more and [5,6] therefore compact RRs and MZIs have not been realized with conventional LIC waveguides. LIC materials have the advantages of low propagation loss, high coupling efficiencies to and from fibers, and relatively mature fabrication processes.

One approach to reduce the chip area required by a splitter is to introduce a structure at the cross section of one input and two output waveguides such as a photonic crystal mirror [7] or as we have proposed in our group, an air trench structure [8]. Air trench bends have been previously designed and fabricated [9,10] in our group that can be used in conjunction with the proposed splitters to realize compact phtonic devices.

A large part of my dissertation is the fabrication and demonstration of high efficiency small area splitters in a perfluorocyclobutyl (PFCB) polymer, which comprises a family of LIC polymers. PFCBs have low propagation losses and a glass transition temperature (Tg) as high as 350°C. I have measured (as detailed in Appendix A) a 0.4 dB/cm propagation loss for PFCB waveguides. Splitters and bends can be realized with air trench structures (ATSs). I developed a very challenging etch process to create high aspect ratio (18:1) anisotropic trenches as narrow as 800 nm. These ATSs are placed at the intersection of an input and two output waveguides to form high efficiency splitters that operate based on frustrated TIR. A total efficiency of 90.1% is achieved (0.45 dB/splitter loss) while the splitting ratio matches very well with the simulation results. High efficiency bends are realized through TIR by placing wider (1.3 μm) ATSs at the bend corner and considering the Goos-Hanchen shift. Simulation of the bends and splitters is done using a two-dimensional finite difference time domain (2-D FDTD) method and a 3-D FDTD method has been used to confirm the results [8].

I have also fabricated and demonstrated an ultra compact RR using small area bends and splitters. The size of this RR is 1700 times smaller than a RR with traditional bends and couplers made in the same material system. Air trench structures are patterned

with electron beam lithography (EBL) on top of the PFCB stack and are aligned to the waveguide structure within the stack.

1.2 Dissertation Overview

The organization of the dissertation is as follows. In Chapter 2, I provide background information on PFCB, the material that we use to demonstrate our concepts. The device fabrication process is also discussed. I provide information on conventional waveguide splitters to set the scene for the advantages we offer with our approach to the realization of compact beam splitters. Finally ring resonators are briefly discussed.

In Chapter 3, I the present development of a small feature, anisotropic and high aspect ratio (18:1) etch for PFCB polymer on silicon substrate. This etch is the key tool that enables fabrication of small area air-trench beam splitters in PFCB waveguide material systems. I propose the use of stress relief trenches on both sides of the main splitter trench as a means to prevent excessive lateral widening of the trench during etching. The content of this chapter is published in the Journal of Vacuum Science and Technology (JVST) B.

Chapter 4 presents small feature etch development on Ultem substrates. This work is aimed at eliminating stress-related fabrication difficulties that arise from a CTE mismatch between the silicon substrate and PFCB film.

In Chapter 5, I present the design, fabrication and characterization of small area air-trench splitters. The 2-D FDTD simulation was done by Dr. Seunghyun Kim while I did mask layout design, fabrication and characterization of the splitters. The design is presented followed by mask design, fabrication and efficiency and splitting ratio

measurement results of fabricated samples. A paper is being prepared based on the content of this chapter to be submitted to a refereed journal (JLT). I also presented this result at the OSA Frontiers in Optics Conference, Rochester, NY, October 2006.

In Chapter 6, I present design, fabrication and characterization of a compact ring resonator in PFCB based on the use of the air-trench splitters presented in Chapter 6. I also present a comparison between ring resonator measured performance and the analytical performance to explain the measurement results. Ring resonator 2D-FDTD simulations were done by Dr. Seunghyun Kim while I did fabrication and characterization of the device.

1.3 New Contributions

The key contributions presented in this dissertation include the following:

1. Developing an anisotropic, high aspect ratio (18:1) etch process to fabricate small feature trenches in PFCB polymers.
2. Reporting a never before observed, stress related lateral widening during the dry etch of a polymer on CTE mismatched substrate and proposing a stress relief method by placing two identical trenches on either side of the main trench to prevent excessive widening.
3. Fabrication and characterization of the first ultra-compact, high efficiency air-trench splitters in a LIC waveguide material system.
4. Fabrication and characterization of the first ultra-compact ring resonator in LIC waveguides by the use of air-trench bends and splitters.

CHAPTER TWO

BACKGROUND

This chapter contains background information about the research subjects presented in this dissertation. They are intended to aid in understanding the motivation and importance of the work in this dissertation.

2.1 Perfluorocyclobutyl (PFCB) Polymers

The proposed devices in this dissertation are designed and fabricated based on the optical properties of a family of organic, partially fluorinated polymers called perfluorocyclobutyl (PFCB). This family of polymers has been developed by Dr. Dennis Smith's group at Clemson University and is being commercialized by Tetramer Technologies, L.L.C. Polymer materials have received a great deal of attention for use in planar lightwave circuits (PLCs). They are cost effective and the fabrication process is relatively easy.

One of the most important issues to be considered is the realization of lower optical attenuation in polymers. Fluorinated materials have been a subject of research for this reason. Removing hydrogen and replacing it with fluorine in the organic network

negates absorption due to the C-H bonds that have strong absorption in the visible and near infrared regions which is where most communication systems operate. Absorption due to C-F bonds occurs at longer wavelengths compared to their C-H counterparts[11].

Fully fluorinated polymers have lower thermal stability, mechanical robustness and solubility in common organic solvents which leads to difficulty in processing and also maintaining the lifetime of optical devices. To solve this problem, in PFCB based polymers, a thermally stable fluorinated ring is ligated to a chemically tailorable aryl through an ether linkage. The resulting family of materials has shown glass transition temperatures as high as 350°C and refractive indices ranging from 1.44-1.51 at a 1550 nm wavelength. These polymers are capable of being used in core and clad structures with minimal insertion losses to silica fibers. Figure 2.1 shows measured absorption spectrum for one type of PFCB [11].

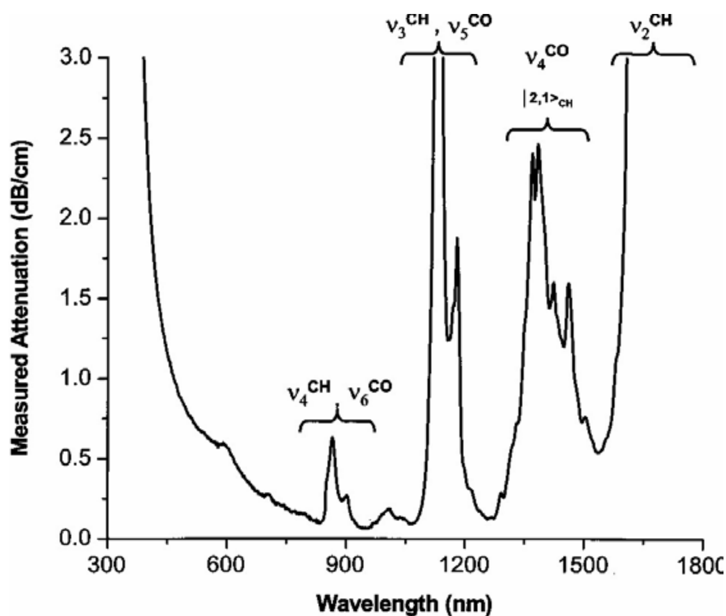

Figure 2.1 Measured attenuation versus wavelength for TVE PFCB [11]

Using PFCB polymers to fabricate waveguide devices was an attractive option for us for the advantages they offer as mentioned in this section and the availability through a DARPA subcontract from Tetramer Tech., L.L.C. Also, we have the required equipment for fabrication of our devices in PFCB polymers in the Nano and Micro Devices Center (NMDC) clean room facilities at UAH. We chose PFCB core and clad polymers with 1.3% refractive index difference to realize our waveguide devices. The preliminary PFCB characterization, including developing a process to achieve a high quality PFCB film, core and clad refractive index measurement and the PFCB waveguide propagation loss measurement, is presented in Appendix A.

2.2 Plasma Etch Theory and Background

Plasma etching is a common step in microfabrication that removes material in selected areas. The features to be etched are usually defined by a lithography step prior to etch. The lithography step defines the etch mask which also etches during the process. Therefore, the etch mask must have adequate etch resistance compared to the material to be etched for it to survive the process.

Figure 2.2 shows typical profiles of polymer features etched in oxygen plasmas. The desired etch for splitters and bends is a perfectly anisotropic profile as shown in Figure 2.2(c)

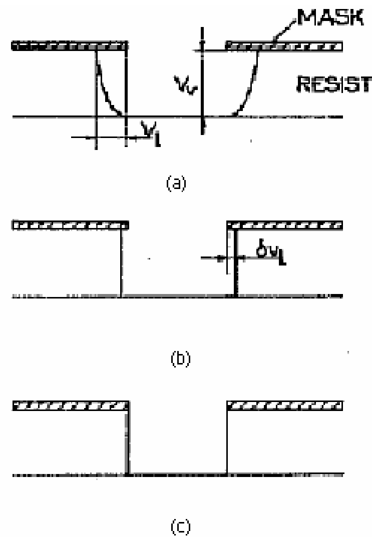

Figure 2.2 Typical etch profile obtained by etching in oxygen (a) isotropic profile (b) vertical profile with residual lateral etching (c) perfect anisotropic profile [12]

There are several different etch mechanisms:

- Spontaneous: Chemical reaction between free radicals with the surface. This mechanism causes isotropic etching and consists of the following reactions:
    - Adsorption of reactive species on the surface
    - Etch product formation
    - Etch product desorption, e.g., Si (s)+4F SiF_4
- Ion Enhanced and Physical etching: This factor affects anisotropy.

The following statements generally describe most reactive ion etch processes:

- More ion energy flux gives better anisotropy
- The higher ion to neutral ratio, the better the anisotropy
- Passivation layer formation helps anisotropy

Figure 2.3 shows different etch mechanisms.

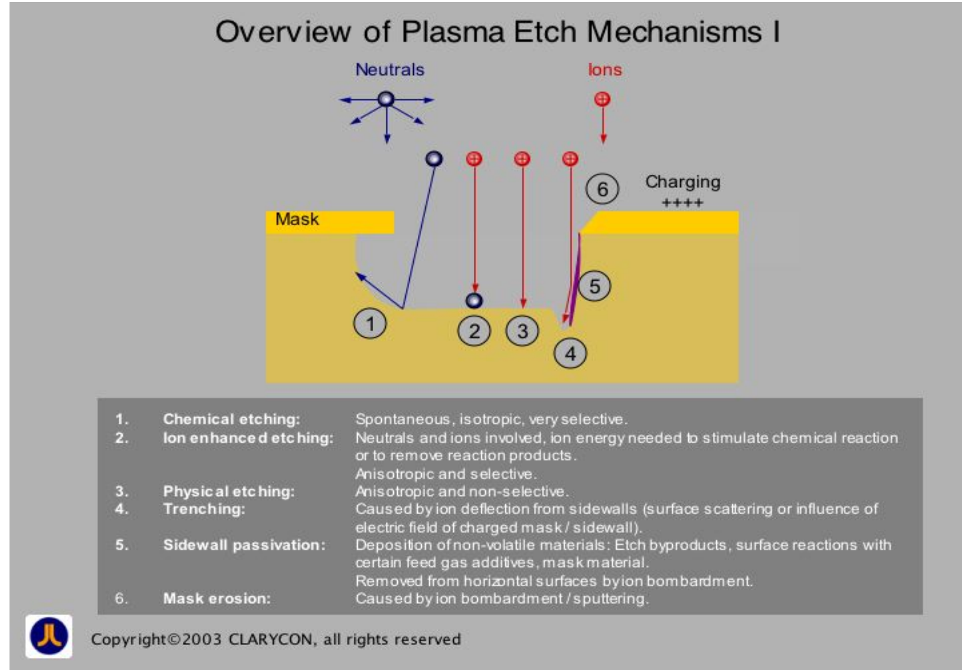

Figure 2.3 Plasma etch mechanisms [13]

Etching polymers in a pure oxygen plasma usually results in isotropic profiles unless it is done at cryogenic temperatures. The low temperatures are aimed at reducing the kinetics of spontaneous etching. Also sidewall passivation may occur as a result of condensation of etch products on the sidewall that makes the sidewall resistant to etching. However, etching at cryogenic temperatures is difficult at an industrial level; therefore, achieving anisotropic profiles at room temperature is of great interest. According to reference [12] there are four ways to achieve room temperature anisotropy with controlled passivation:

1. A gas in the mixture which once deposited, cannot be removed by the etching gases unless under intense ion bombardment.

2. A volatile compound in the mixture at a concentration such that its deposition rate on the sidewall is equal to the lateral spontaneous etch rate.
3. A gaseous element's competitive adsorption which inhibits spontaneous etching of the active gas.
4. An etching gas which does not produce any spontaneous etching at room temperature.

In Chapter 3 of this dissertation, we report the successful development of a PFCB etch using a CO/O_2 etch chemistry in an ICP RIE. We achieve deep (~14 μm), narrow (800 nm) trenches with vertical sidewalls for an etch aspect ratio of 18:1. The addition of CO promotes the development of a thin passivation layer on the sidewalls to suppress spontaneous chemical etching by oxygen and thereby prevents excessive trench widening.

2.3 EBL on Top of PFCB Stack Process

To fabricate high efficiency bends and splitters, air trench structures have to meet three very important criteria: (1) vertical sidewalls, (2) precise positioning of air trench with respect to the waveguide, and (3) smooth sidewalls. Maintaining sidewall verticality is addressed in etch development while air trench to waveguide positioning is a matter of good alignment during patterning. Finally sidewall roughness is affected by both lithography (line quality) and the etch chemistry.

To improve the placement accuracy of an air trench interface with respect to a waveguide junction, we use the autoalignment feature of our in-house NPGS version 9 electron beam lithography system (JC Nabity Lithography Systems), which is used with a

LEO 1550 field emission scanning electron microscope (SEM). We place appropriate alignment marks in each of the four corners of an exposure field to achieve less than 40 nm alignment accuracy [14]. Compared to optical lithography in a contact mask aligner (our other available lithography capability), EBL also offers better line width control and line quality (in terms of roughness) for our feature sizes of interest, which are 800 nm and 1.3 µm. In the case of our research, to have good alignment accuracy between the waveguide structure (which is sandwiched between the upper and lower cladding) and splitters and bend structures (patterned on top of the upper cladding), the EBL alignment marks (AM) and the waveguides have to be laid out at the same time. This somewhat complicates the fabrication process since PFCB is not e-beam transparent and e-beam AMs at the core layer have to be revealed by etching openings in the cladding. After the opening etch, AMs are easily seen in the SEM and precise alignment is achieved. The process flow for EBL on top of a PFCB stack is shown in Appendix B.

The fabrication process used to fabricate splitters, bends and ring resonators in Chapters 5 and 6 is made possible by EBL on top of the PFCB stack.

2.4 Waveguide Beam-Splitters

Dense integration of optical components has long been a subject of interest for researchers. Waveguide beam splitters are one of the essential planar lightwave circuit (PLC) components that along with bends can realize many optical devices such as ring resonators, MZIs and MMI [8, 15]. Traditionally, waveguide beam splitting has been done with a Y-branch configuration, but when it comes to higher integration of optical

components, the small branching angle, long tapered regions and intrinsic mode mismatch loss are problematic [16].

In order to reduce the size of splitters and bends, several approaches have been employed. Many of the designs are based on high index contrast (HIC) materials as they appear to be a natural choice for their high mode confinement to realize compact bends and splitters. However, they suffer higher propagation loss induced by sidewall roughness and high coupling losses [17, 18]. Low index contrast (LIC) waveguide material systems have the advantages of lower propagation losses and easier light coupling into them. Miniaturization in an LIC material can be achieved by design as we will present in this section as well as in Chapter 6 and 7 of this dissertation. We will summarize various approaches in making compact waveguide splitters in this section and compare their compactness as well as splitting efficiency.

The traditional small angle Y-branch splitter as shown in Figure 2.4(a) requires large device lengths to achieve a low loss transition to the two arms [16]. A T-junction is a Y-branch of 90° half angle. Figure 2.4(b) shows a T-junction design based on high index contrast waveguides [19]. Resonant cavities are designed at the junction, so the mode is steered around each corner with low radiation loss. FDTD simulation results show a 99% total efficiency. Air hole photonic crystals have been used to realize splitters in the HIC material as well [7]; 2D-FDTD simulations show 99% efficiency of the splitter. Fabrication in SOI wafers showed over 90% efficiency and a reflection to transmission ratio of 5.9% which is close to the 5.7% predicted by simulation. Figures 2.4(c) and (d) show a schematic and an SEM image of the fabricated device. Figures 2.4 (e) and (f) show the splitter configuration in what they consider an LIC

material ($\Delta n = 6.8\%$). Air-trenches are used to provide locally enhanced lateral confinement. Adiabatic tapering is used to avoid abrupt junction induced mode mismatch and Fresnel reflection [21]. The bend radius R = 10 μm and measurement shows 0.6 dB/junction loss and a 45/55 splitting ratio. A four port air trench splitter is designed for the HIC material where maximum overall throughput is ~81% with less than 1% reflection and cross talk between ports [22].

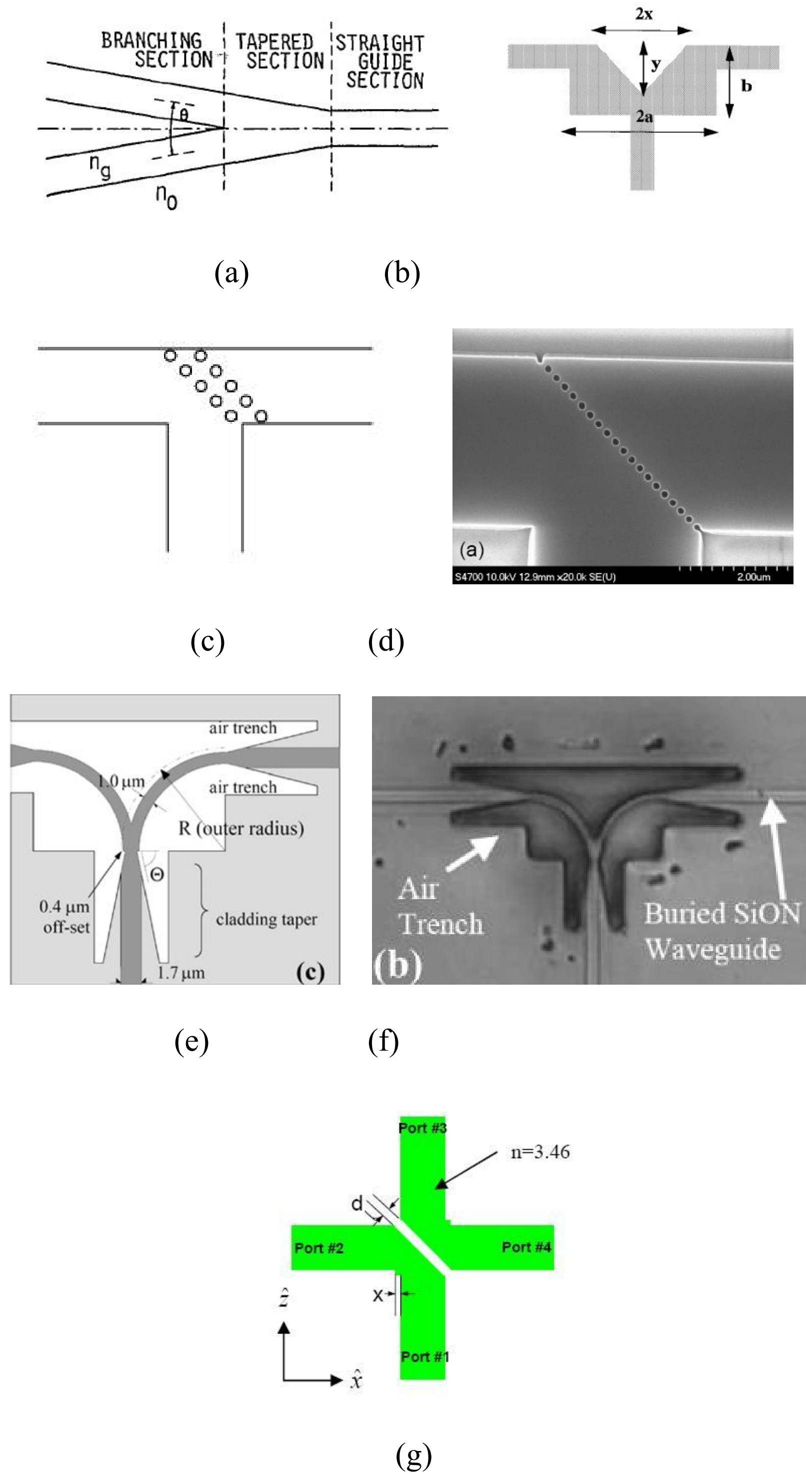

(a) (b)

(c) (d)

(e) (f)

(g)

Figure 2.4 Various waveguide beam splitter configurations proposed by researchers (a) traditional Y-branch splitter [16] (b) use of resonant cavities at the junction in HIC [19] (c) PhC airhole splitter in HIC [7] (d) SEM image of PhC airhole fabricated [7] (e) airtrenches and adiabatic tapering in LIC [21] (f) SEM image of fabricated device [21] (g) four port air-trench splitter in HIC [22]

In Chapter 5 we present an air-trench beam splitter that uses the principle of frustrated total internal reflection (FTIR) [8]. While high efficiency air-trench splitters have been demonstrated in high refractive index contrast waveguides; the work in this dissertation demonstrates them in low refractive index contrast waveguides. As discussed in this section, LIC waveguides have the advantage of lower propagation and coupling losses which our splitter devices enjoy by use of PFCB polymers. Another advantage of our waveguide splitters is its compact size (a 22 μm x 800 nm trench used at intersection of waveguides). However, a very important aspect of our compact design for splitters is that the device size is independent of refractive index difference. This means that the same idea can be used for other popular LIC waveguide material systems such as silica as well as the HIC such as silicon on insulator (SOI) waveguides. The only challenging aspect of our work is the air-trench structure requirements that call for a very challenging ICP-RIE etch development. In Chapter 3 we discuss the high aspect ratio anisotropic etch on small features that makes the fabrication of this beam splitter possible. Chapter 5 presents design and simulation for 90° (85-15 splitting ratio) splitters for use in ring resonators and 107.5^{o} equal power splitters as well as fabrication and measurement for the 85-15 splitter.

2.5 Ring Resonators

A traditional ring resonator (RR) consists of a waveguide formed as a closed loop (circle, racetrack or ellipse) and coupled to one or more input/output waveguides. If light

with a wavelength satisfying the condition $\phi = kd = 2\pi q$ (where $k = \frac{2\pi n}{\lambda}$ is the wavenumber, d is the ring circumference and q an integer) is coupled in the RR, intensity builds up as the light travels multiple round-trips due to constructive interference. When only one bus waveguide is used, the device is an all pass or phase filter. A second waveguide can be used to pick up the resonant frequencies and this configuration acts as an optical channel dropping filter. Because of their frequency sensitive response, RRs have been studied for various photonics applications, such as add/drop and band pass filters, wavelength division multiplexer/demultiplexers, and optical switches [24, 42-46].

There are challenges in realizing compact ring resonators. One problem is the weak coupling between bus waveguide and a perfect ring. Racetrack resonators have been used to facilitate a longer coupling region [20]. However, this increases the device size. Another issue lies in the precise coupling of light because of the small separation between the bus waveguide and the ring. Chu *et al.* used a stack RR in which the bus waveguide and the ring are vertically placed and coupling efficiency is controlled by the thickness of the spacer [23].

Compact RR can be realized in an HIC material and photonic crystals because light is highly confined to the core region making a low loss tight bend possible [44-46]. However, as previously noted, propagation and fiber coupling losses are much higher than LIC waveguides [48]. The large radius of the ring required for low loss waveguide turns makes realizing compact RRs challenging in an LIC material.

In Chapter 6, we present an ultra-compact RR in an LIC material with the use of air trenches as bends (to turn the waveguide around the corners) and splitters (for in and

out coupling as well as completing the RR loop). We reduce the RR size 1700 times compared to a traditional RR made in the same material system.

CHAPTER THREE

PFCB SMALL FEATURE ETCH DEVELOPMENT ON SILICON SUBSTRATE

We have developed an anisotropic, high aspect ratio (18:1) etch for perfluorocyclobutyl (PFCB) polymers with trenches as narrow as 800 nm using a CO/O_2 etch chemistry in an inductively coupled plasma reactive ion etcher (ICP RIE). Anisotropy is achieved by carbon sidewall passivation. The motivation for this etch development is to use the air trenches as very compact waveguide splitters [8]. We report a new trench widening mechanism due to the tensile stress of the PFCB films, and a method of avoiding this widening through the use of additional stress relief trenches on both sides of the desired trench. A paper containing the CO/O_2 etch development with the stress relief method was published in the Journal of Vacuum Science and Technology (JVST) B. Prior to developing the desired etch with CO/O_2 chemistry, an SF_6/O_2 chemistry was considered and an acceptable etch was developed. This effort is also presented in this chapter.

3.1. Introduction

Polymers have long been of interest as a platform for planar lightwave circuits (PLCs) [8, 10, 28-31]. Fluorinated polymers have attracted particular attention because of their typically low propagation loss at telecommunication wavelengths. Perfluorocyclobutyl [32, 33] (PFCB) (Tetramer Technologies, Inc.) comprises a family of partially fluorinated copolymers with selectable refractive index based on copolymer composition, and glass transition temperatures as high as 350°C (PFCB chemical structure is shown in Figure 3.1) [11]. Waveguides fabricated with such materials typically have low refractive index contrast (1-3%) between the core and clad. Similar to low refractive index contrast silica waveguides, this results in a minimum waveguide bend radius on the order of several millimeters or larger, which is a limiting factor in decreasing the size of waveguide elements in PLCs to enable higher levels of integration.

We recently proposed the use of air trenches to create small area bends and splitters in materials with a low refractive index (i.e., on the order of 1.5, as opposed to higher index materials such as silicon nitride and semiconductors), which permits the size of these waveguide elements to be essentially independent of the core/clad refractive index contrast [34]. We have demonstrated high efficiency bends in PFCB [10], and have designed air trench splitters suitable for compact ring resonators and Mach-Zehnder interferometers (see for example, Figure 3.2) [8]. However, fabrication of air trench splitters is challenging since they require narrow (800 nm), high aspect ratio (18:1) trenches.

Anisotropic etching of polymers has been reported in the literature with different degrees of achieved anisotropy and aspect ratio. For example, a high aspect ratio etch of features as narrow as 150 nm has been developed for SiLK™ using a high density plasma source and in which anisotropy is a result of passivation with polymer graphitization [35]. The maximum achieved aspect ratio is ~6:1 in N_2/O_2 and N_2/H_2 plasmas. A deep reactive ion etch (RIE) with vertical sidewalls has likewise been achieved in PMMA using Ar and O_2 [36]. Etch depths of up to 85 μm were achieved for features ~65 μm and larger.

As reported in Reference [4], we have developed an anisotropic etch for PFCB using a He/O_2 etch chemistry in an inductively coupled plasma reactive ion etcher (ICP-RIE) (Surface Technology Systems) with SiO_2 as an etch mask [10]. Etched trenches 20 μm wide and 14 μm deep with vertical sidewalls have been fabricated. However, this etch has over 1 μm lateral widening, which makes it unsuitable for the 800 nm features needed for air trench beam splitters.

Schuppert *et al.* developed a cryo-cooled RIE etch process for PFCB using a SF_6/O_2 etch chemistry and a substrate temperature of -50°C [37]. The purpose of the low temperature is to reduce the kinetics of spontaneous etching on the sidewalls. This etch has a smaller lateral widening compared to room temperature etches, but the achieved aspect ratio is only 1:1 and the sidewall angle is 85 degrees. In contrast, we need to achieve a sidewall angle of 90+/-1 degrees to achieve high optical efficiency.

While oxygen is typically used as the primary gas in the plasma etching of polymers due to its high reactivity, ion induced lateral spontaneous etching is also present [12, 38] which usually results in linewidth broadening and non-vertical sidewalls, particularly for etches conducted at room temperature or above. To reduce or eliminate

this lateral etching, a gas can be added to the plasma to create a protective passivation layer on the sidewalls [12, 35, 37, 39]. In this chapter we report the successful development of a PFCB etch using a CO/O_2 etch chemistry in an ICP RIE. We achieve deep (~14 μm), narrow (800 nm) trenches with vertical sidewalls for an etch aspect ratio of 18:1. The addition of CO promotes the development of a thin passivation layer on the sidewalls to suppress spontaneous chemical etching by oxygen and thereby prevents excessive trench widening.

We have also found another source of trench widening that can dramatically affect the realization of submicron high aspect ratio features. Since the PFCB films in our samples are under tensile stress, this stress tends to pull apart the edges of the trench to create a wider trench than would otherwise result if the film were unstressed. We report a method of avoiding this stress-induced broadening by etching narrow stress-relieving trenches on both sides of the main trench.

This chapter is organized as follows. In Section 3.2 we discuss initial etch development with optically patterned features using a contact mask aligner for both SF_6/O_2 and CO/O_2 etch chemistry. However, since fabrication of high efficiency splitters requires precise air trench-to-waveguide alignment that cannot be achieved in a mask aligner, we finalized our etch process development with electron beam lithography (EBL) performed in a scanning electron microscope (SEM). This not only permitted accurate alignment, but also had the benefit of being much more repeatable in defining the trench width for submicron features. The EBL etch process is discussed in Section 3.3. In Section 3.4 we explore the effects of PFCB film stress on trench widening and show how this can be avoided with extra stress-relieving trenches. Section 3.5 summarizes some of

the difficulties we experienced during etch development as a result of environment and equipment variability.

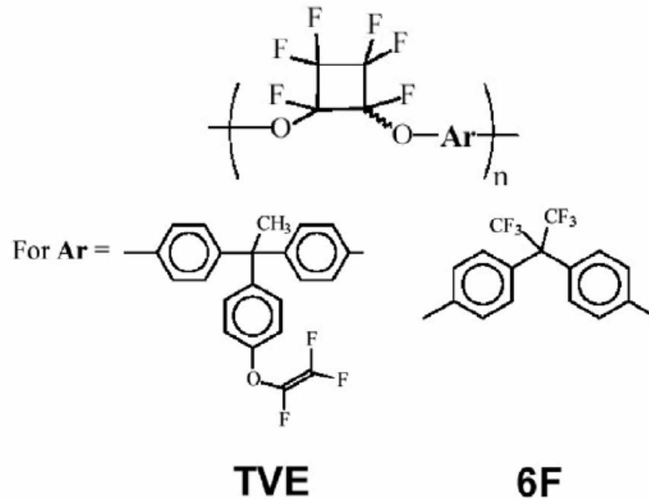

Figure 3.1 PFCB chemical structure showing the polymer unit cell and the two chemical structures contained in the copolymers supplied to us by Tetramer Technologies, Inc.[32]

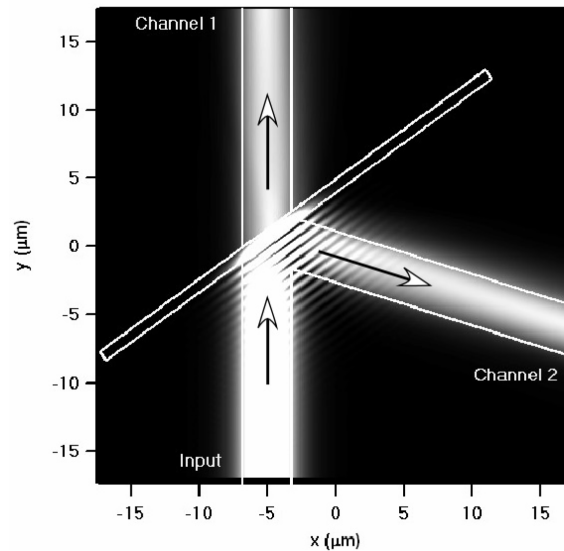

Figure 3.2 Two-dimensional finite difference time domain (2D-FDTD) simulation results at a wavelength of 1550 nm for an 800 nm wide, air trench as a 50:50 waveguide beam splitter. 2D simulation predicts a total optical efficiency of 98 % [8]

3.2 Preliminary SFE Development with Optically Patterned Features

Initial PFCB etch development using both SF6/O_2 and CO/O_2 chemistry was done with an optically patterned array of trenches ranging in width from 0.5 μm to 20 μm. Etch samples were prepared by sequentially spin coating and curing two 11 μm thick PFCB films on 3 inch Si wafers, which corresponds to the final thickness of the eventual fully processed waveguide samples. An HCl-based adhesion promoter was applied to the Si substrate prior to spin coating the first film. Curing was performed in a nitrogen atmosphere with samples beginning at room temperature and then ramped up to 190°C at a rate of 1°C/min followed by a dwell time of 22 hours (the cure process is discussed in Appendix A). After curing, a positive photoresist (AZ 701 MiR), was spin coated on top of the PFCB film stack and exposed with the trench array pattern by optical contact lithography. A 120 nm thick aluminum film was thermally evaporated on the samples, followed by lift off to create an aluminum etch mask.

3.2.1 SF_6/O_2 Etch

The first etch chemistries we considered for small feature etch were SF_6 and O_2 in the ICP/RIE in which sulfur acted as the passivation agent based on Reference [12].

For SF_6/O_2 etch we changed parameters such as coil power, platen temperature and chamber pressure to achieve the final etch. Aluminum was used as an etch mask. SiO_2 was another etch mask choice but the fluorine in SF_6 etches the SiO_2 etch mask. The final etch recipe was developed as follows:

- O_2 (10sccm):SF_6 (30)
- 200 W Coil power
- 150 W platen power
- 10 mTorr Pressure
- -5 C platen temperature
- 36 minutes to etch 14 μm deep trenches on 800 nm wide features

This recipe etched 14 μm deep trenches with vertical sidewalls as shown in Figure 3.3(a) and (b). On features wider than 1.8 μm, we observed a surface grass problem (Figure 3.4(a)). We suspect this problem could be because of the micro-masking of etch bi-products. Since the grass does not appear on the smaller features of our interest, we did not pursue it further. Also there is a 150 nm thick passivation sidewall that is responsible for achieved anisotropy. However, if used as a waveguide splitter, the optical effects of this layer are not known.

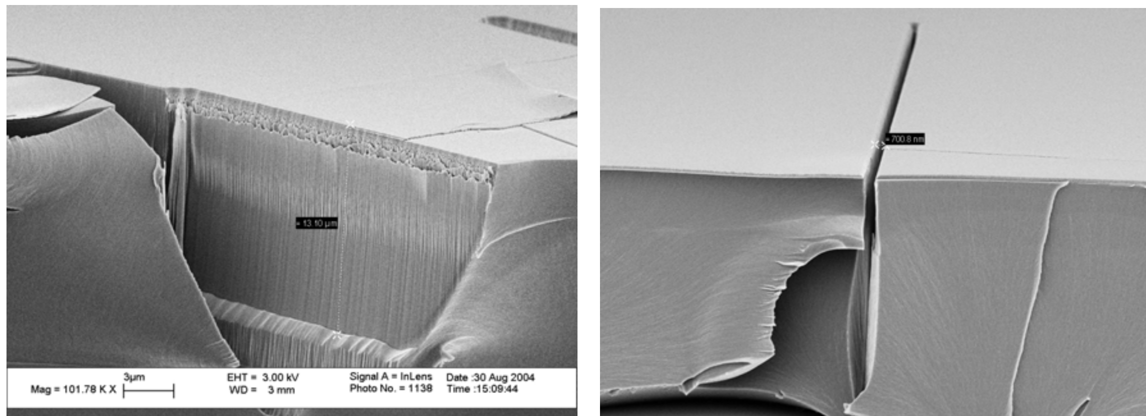

(a) (b)

Figure 3.3 Trenches etched with SF_6/O_2 etch (a) sideview of sidewall verticality (one trench wall was broken during cleave) (b) tilted top view showing the trench width

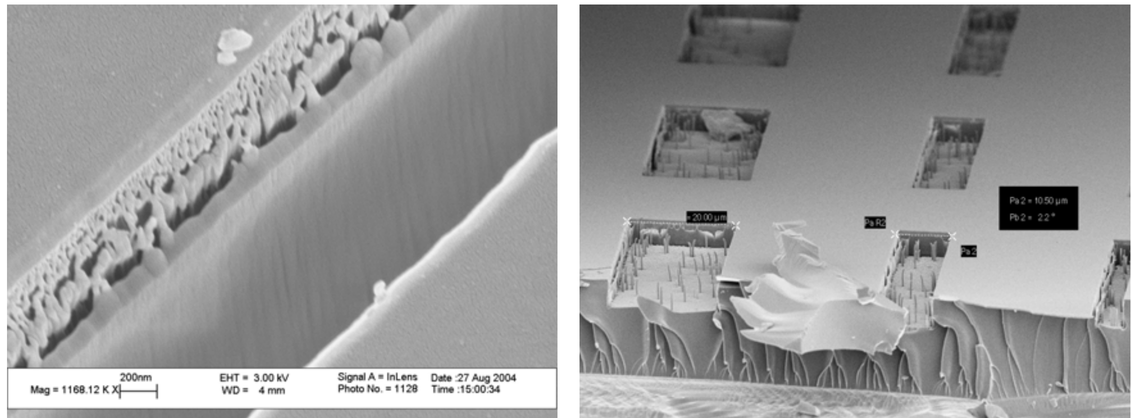

Figure 3.4 (a) passivation sidewall (b) grass on larger features

3.2.2 CO/O_2 Etch

We varied different etch parameters such as the ratio of the CO to O_2 gas flow rate (which included the extreme cases of etching with only CO and only O_2 shown in Figure 3.5(a) and (b)), chamber pressure, coil power, platen power, and platen temperature to obtain an anisotropic, high aspect ratio etch. The best etch result was achieved with 500W coil power, 200W platen power, 5 mTorr chamber pressure and 25 sccm CO and 5 sccm O_2 flow rates. The platen was kept at 10^oC by helium backside cooling. Figure 3.6 shows the final etch results after a 54 min PFCB etch. Figure 3.6(a) is a cross-sectional SEM image of the trenches, showing sidewall verticality on small features as well as the desired 14 μm etch depth. Figure 3.6(b) shows a top view of an 838 nm wide trench achieved on one of the optically patterned trenches after being etched more than 14 μm deep. Figure 3.7 shows the etch rate as a function of trench width, indicating that the etch rate is aspect ratio dependent (as expected).

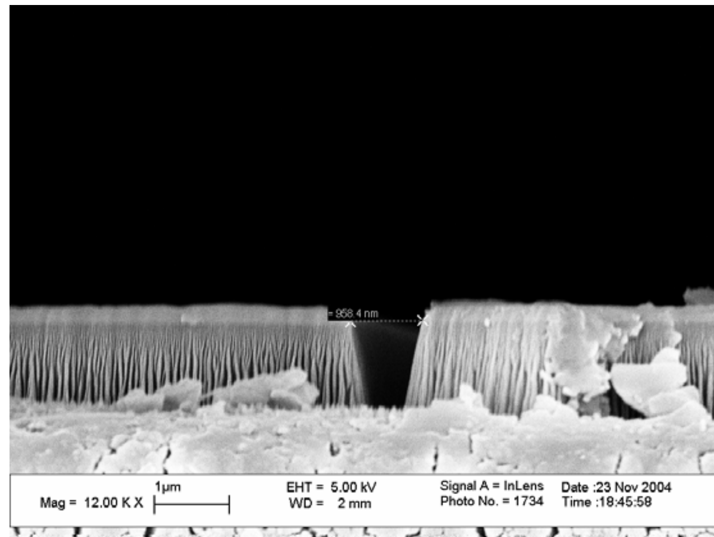

(a)

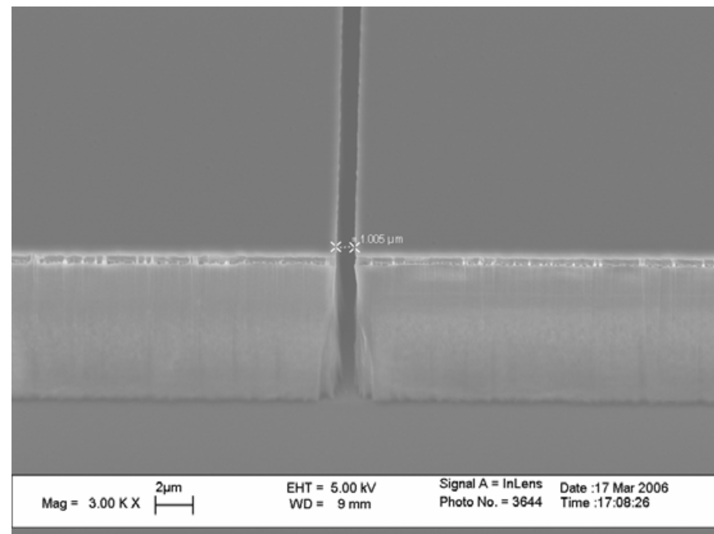

(b)

Figure 3.5 The extreme cases of etching with (a) straight CO, with the rest etch parameters being the same. Excessive passivation. Low etch rate of 40nm/min. non-vertical sidewalls (b) straight O_2, isotropic etching. bowing of the sidewall. Trench is wider on top

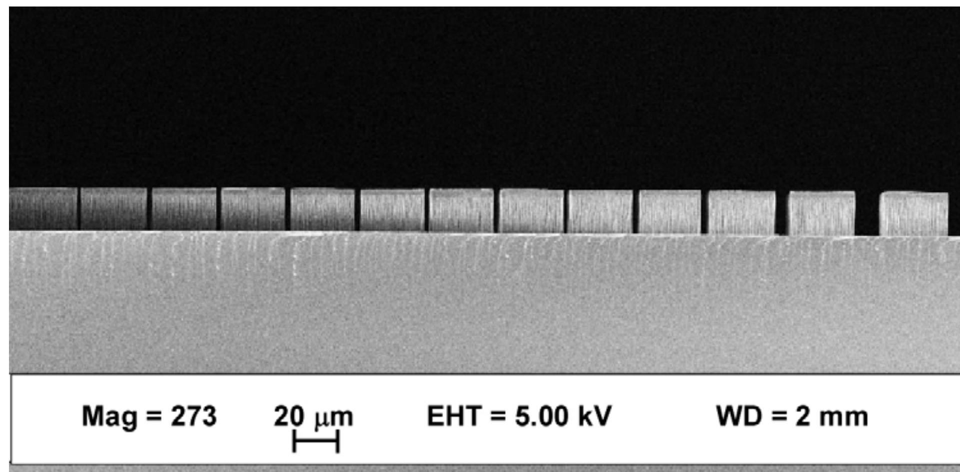

(a)

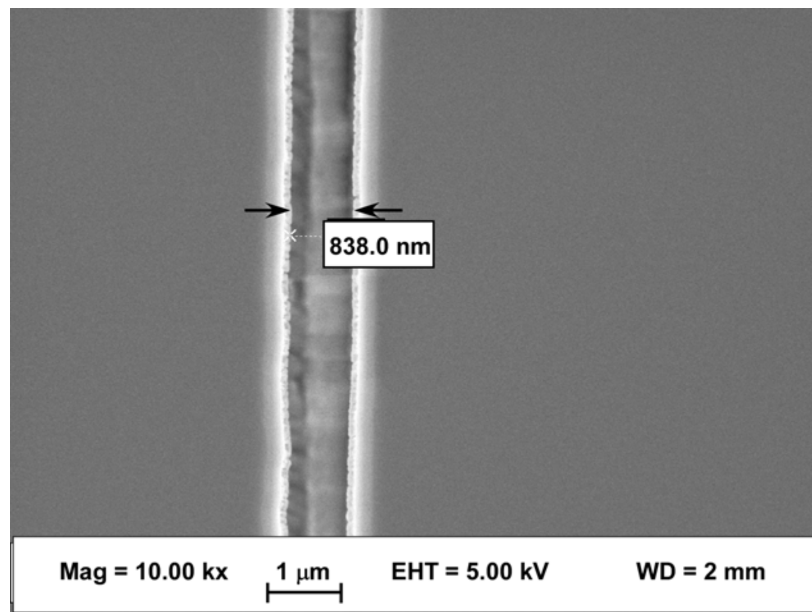

(b)

Figure 3.6 SEM images of fully etched optically written trenches (a) cross-sectional view showing 14 μm depth and vertical sidewalls (b) top view showing ~800 nm width

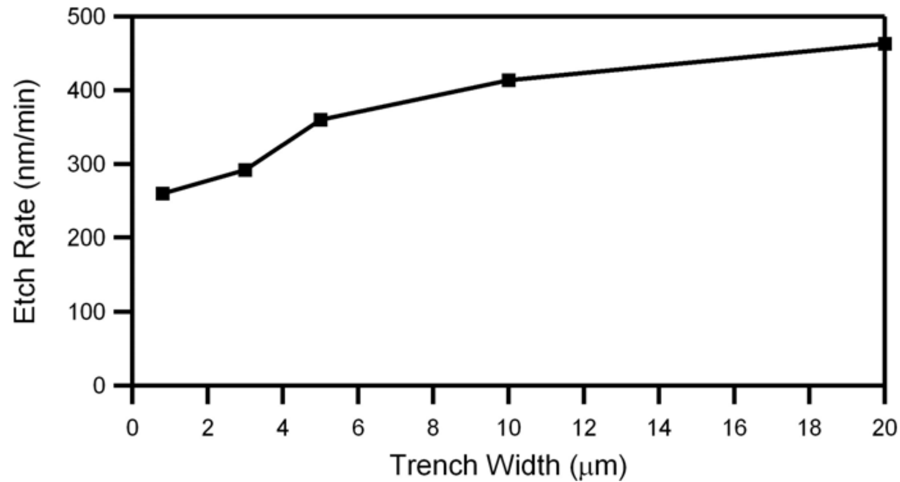

Figure 3.7 Aspect ratio dependent etch rate for PFCB with CO/O_2 etch

While the optical lithography results show that it is possible to etch trenches of the desired size and aspect ratio, the alignment accuracy that can be achieved in a contact mask aligner is typically at best ~1 μm. However, to achieve maximum optical efficiency, a splitter needs to be placed to within 100 nm of its ideal position [10]. Moreover, it is very difficult to pattern 800 nm features with reasonable uniformity and yield over a 3 inch wafer. We therefore opted to use our other in-house lithography capability which overcomes both of these difficulties. This required a variety of process adjustments, which are detailed in the next section.

3.3 Etch Process for Electron Beam Patterned Features

We have found that we can generally achieve alignment accuracies significantly better than 40 nm using the autoalignment feature of the Nanometer Pattern Generating System (NPGS, from JC Nabity Lithography Systems) when we do electron beam lithography in a LEO 1550 field emission scanning electron microscope (SEM).

However, the lift off process described in Section 4.2 to pattern the aluminum etch mask can't be used with e-beam lithography due to the charge that accumulates in the absence of a conductive layer during patterning. Charging causes poor visibility of the EBL alignment marks and consequently poor trench-to-waveguide alignment. To avoid this problem, we deposit a 120 nm thick uniform aluminum film directly on top of the PFCB layer, and then spin coat a positive e-beam resist, ZEP 520A (ZEON Corp.) (see Figure 3.8 for fabrication process schematic). The conductive aluminum film dissipates electrons during EBL thereby eliminating the charging problem but necessitating that the Al be etched rather than lifted off.

ZEP 520 A, positive e-beam resist

Aluminum

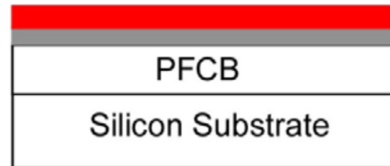

(a)

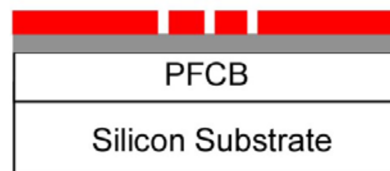

(b)

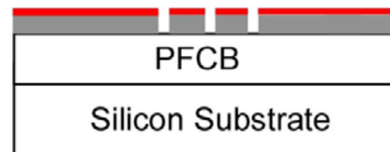

(c)

(d)

Figure 3.8 Fabrication process schematic

After exposure and development of the e-beam resist, we physically sputter the aluminum film in the ICP RIE using an argon plasma with ZEP 520A as the etch mask. To survive through the entire aluminum etch process, we found that the ZEP e-beam

resist needed to be 550 nm thick and soft baked at the upper end of its temperature range (180°C) in order to improve its etch resistance. The final optimized aluminum etch process is a 10 sccm argon flow rate, 5 mTorr chamber pressure, 600 W coil power, 300 W platen power, and a platen temperature of 20°C. The etch time is 6 minutes. Figure 3.9 shows a small trench after the aluminum etch.

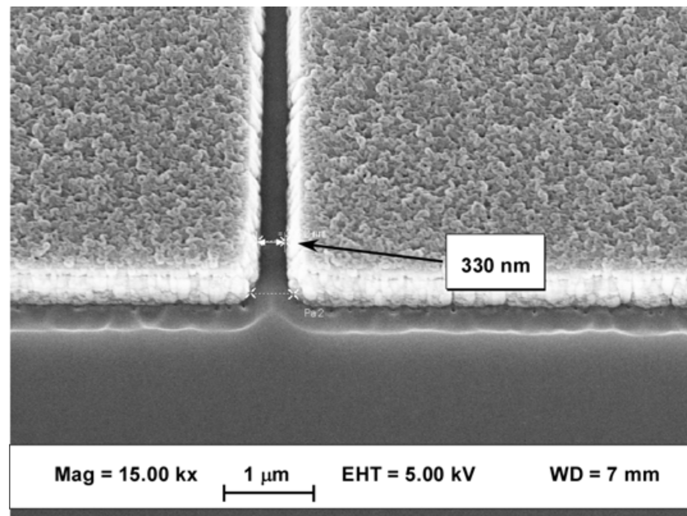

Figure 3.9 Small feature in aluminum film after the aluminum etch. The rough layer on top is the remaining

Immediately after the aluminum etch, we use the same CO/O_2 etch process discussed in Section 3.2 to etch comb shape patterns in the PFCB, with each group of comb teeth having a different width ranging from 200 nm to 800 nm. We find that a 250 nm wide pattern in aluminum results in an 800 nm wide trench etched in PFCB. Thus there is 550 nm of lateral widening during the etch. Figures 3.10(a) and 3.10(b) show a top view and tilted cross-sectional SEM images of trenches after the PFCB etch. Note in Figure 3.10(a) that the trench edges are reasonably smooth, while in Figure 3.10(b) the

sidewall verticality appears excellent despite some plastic deformation due to cleaving. Also note that the etch depth is over 14 μm.

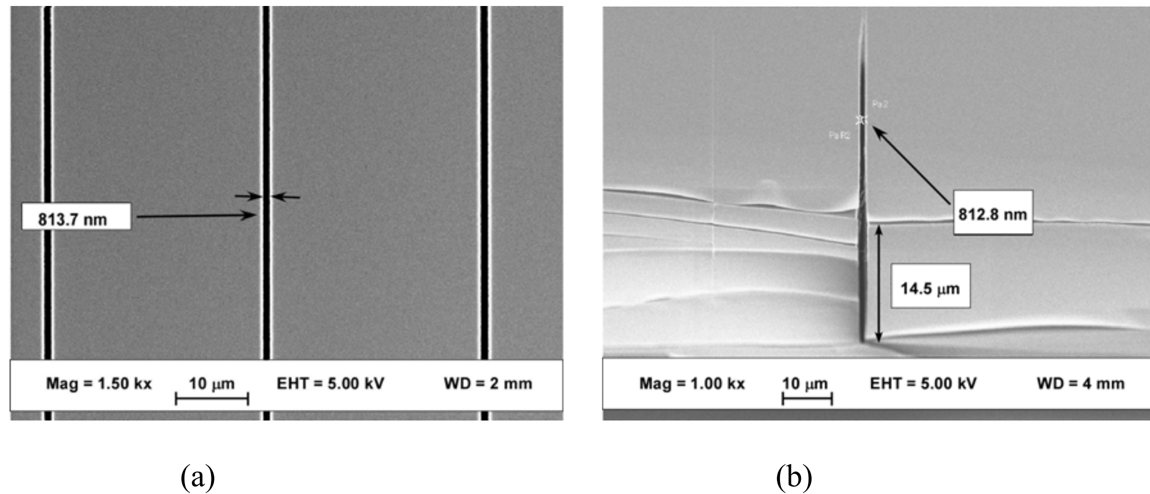

(a) (b)

Figure 3.10 SEM images of fully etched trenches (a) top view (b) tilted cross-sectional view

3.4 Stress Induced Lateral Widening

For actual device fabrication, individual air trench waveguide splitters are patterned and etched at waveguide intersections. Figure 3.11 shows a top view of one such isolated trench after the PFCB etch, which was initially written as a 250 nm wide line by EBL. Note that the trench is widened to ~2 μm, and that there is severe cracking at the trench ends. This is caused by tensile stress in the PFCB film, which is a result of the coefficient of thermal expansion (CTE) mismatch between PFCB (~60 ppm/^{o}C) and Si (2.6 ppm/^{o}C at 293 ^{o}K) and the PFCB curing process. When the wafer is brought to room temperature after being cured at 190°C, the PFCB film attempts to shrink more than

the Si substrate, thereby resulting in considerable tensile stress in the PFCB film, which in turn significantly widens isolated trenches.

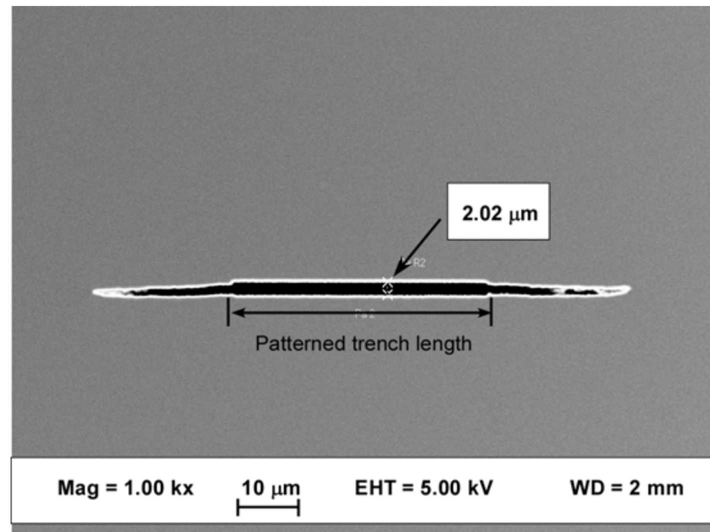

Figure 3.11 Extreme lateral widening and cracking at the ends on an isolated trench

A careful inspection of the etched comb patterns discussed in Section 3.3 suggests a method of relieving the stress and obtaining the desired trench widths. As shown in Figure 3.12, a comb pattern in which all of the comb fingers are EBL patterned with a width of 250 nm results in all of the inner trenches having the expected width of 800 nm after etching. However, note that the widths of the two outermost trenches are ~1.94 μm. Clearly, the outermost trenches relieve the tensile stress for the region in between them (at least in the direction perpendicular to the trenches), which permits the inner trenches to be broadened only by the reactive ion etch process such that they have the desired final width.

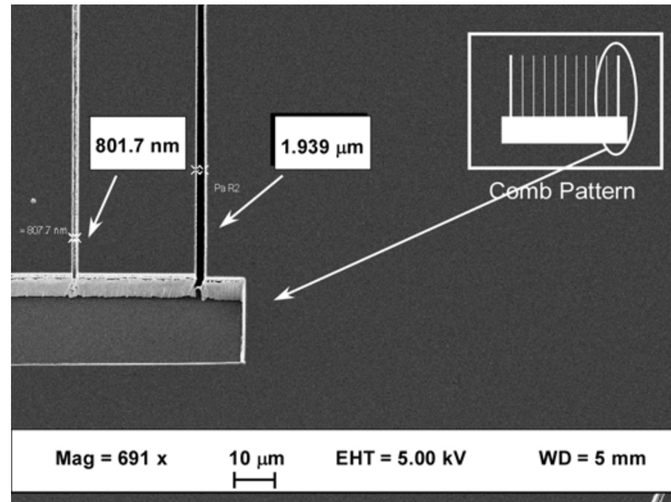

Figure 3.12 Stress related widening of the outmost trenches in an etched comb pattern. All trenches had the same 250 nm starting width patterned by e-beam lithography.

As shown in Figure 3.13(a), we can therefore avoid trench widening by placing the desired trench between two stress relief trenches. Each of the trenches shown in Figure 3.13(a) began as a 250 nm wide EBL patterned line, with 30 μm separation between lines. After etching, the middle trench is 777 nm wide while the stress relief trenches are widened to 1.3 μm and cracked at the ends. This result confirms the effectiveness of the use of adjacent stress relief trenches to avoid stress induced broadening of the middle trench.

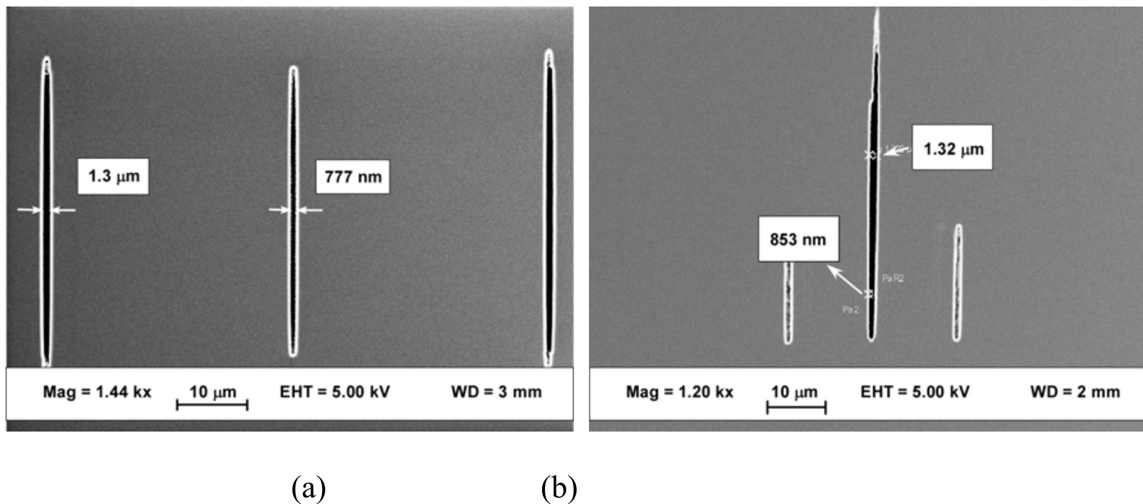

(a) (b)

Figure 3.13 Effect of stress relief trenches. (a) Three identically patterned trenches. (b) Half-length stress relief trenches (see text for discussion).

As a further demonstration of this stress relieving approach, consider Figure 3.13(b), which shows stress relief trenches patterned only adjacent to the lower half of the middle trench, which has a post-etch width of 853 nm. The upper half of the middle trench, which is not between stress relief trenches, has a width of 1.32 nm, and this end of the trench is cracked.

The main drawback to the use of stress relief trenches is that some trial and error is required to determine the width of the EBL patterned trenches that result in the desired width of the final etched trench. Nonetheless, our experience indicates that this is relatively straightforward. Figure 3.14(a) shows the middle trench widened to 840 nm with stress relief trenches at 35 μm distance. The trench widening decreases to make a 780 nm wide trench as stress relief features are moved closer to 30 μm on one side and 15 μm on the other. This pattern continues as both trenches are moved closer to 15 μm of the main trench and the trench width is reduced to 520 nm. Also, in the case of fabrication and characterization of waveguide splitters, the stress relief trenches need to

be placed far enough from the waveguide such that they do not intersect the waveguide mode. For our waveguide geometry, 99.99% of the modal power is within a circle of 7 μm radius centered on the waveguide core. Therefore all stress relief trenches have to be placed at least 7 μm away from the waveguide, which is not onerous for our applications.

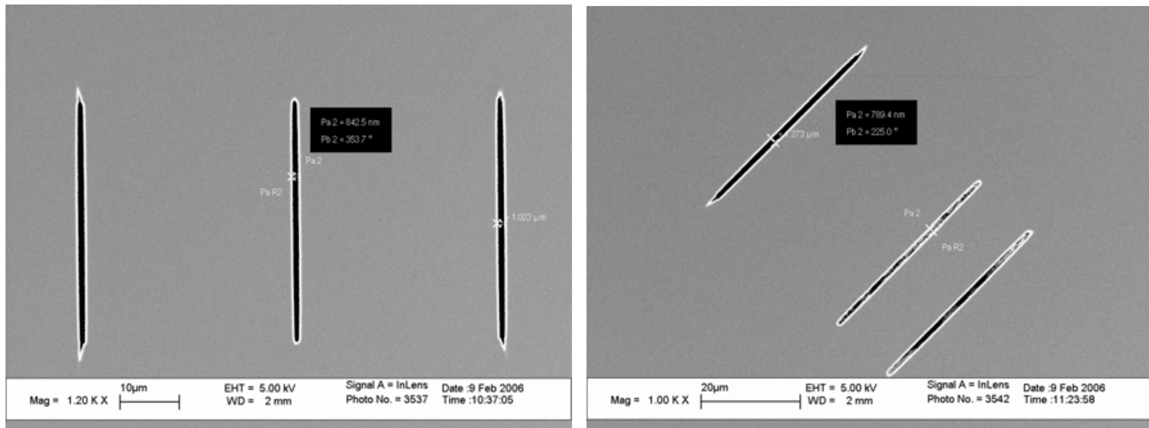

(a) (b)

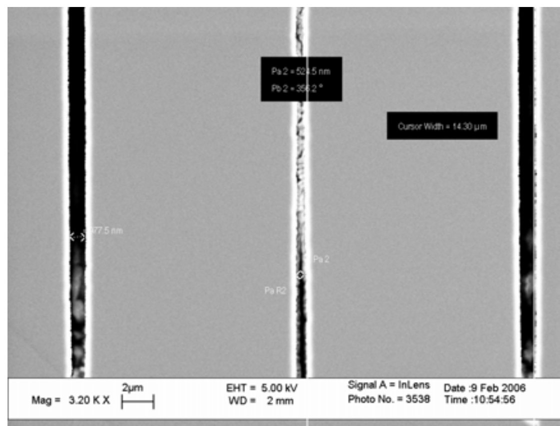

(c)

Figure 3.14 stress relief feature distance effect on widening with trenches placed at (a) 35 μm (b) uneven at 15 and 30 (c) at 15 μm

To the best or our knowledge, stress induced lateral widening of etched polymer trenches on Si substrates has not been noted by other groups, despite extensive polymer

etching reported in the literature. This is likely due to the fact that the effect of this trench widening mechanism is indistinguishable from the lateral widening that is often associated with anisotropic reactive ion etching. For example, we now consider it likely that the lateral widening reported in our previous paper for He/O_2 anisotropic etching of PFCB [10] is due to a combination of reactive ion etch effects and tensile stress broadening. Note that in that paper we were nonetheless successful in compensating for this widening in our optical patterning in order to accurately place trench edges relative to waveguide intersections. We expect that similar stress-induced widening effects are present with other polymer films that are cured on non-CTE matched substrates and in which deep trenches are etched. This will be particularly noticeable for small feature, high aspect ratio trenches that are etched most or all of the way through the polymer film.

3.5 Conclusion

We have developed a small feature, high aspect ratio (18:1), anisotropic etch for PFCB polymers that uses a CO/O_2 etch chemistry in an ICP RIE. Anisotropy was achieved by controlled trench sidewall passivation based on the use of CO. Tensile stress in the PFCB film resulted in excessive trench widening for isolated trenches. We have demonstrated how stress relief trenches can be used to avoid widening of the main trench.

CHAPTER FOUR

PFCB SMALL FEATURE ETCH DEVELOPMENT ON ULTEM SUBSTRATE

This chapter presents PFCB etch development on an Ultem substrate. Ultem substrate has an advantage of closer CTE to PFCB film. This reduces stress related problems that we have experienced as a result of CTE mismatch between PFCB and silicon substrate.

4.1 Introduction

A PFCB small features etch development was presented in the previous chapter on silicon substrate. As mentioned in Chapter 3, there are many stress related process issues because of the CTE mismatch between silicon and the PFCB film. To eliminate these problems, we decided to develop the same fabrication process on a substrate that has a closer coefficient of thermal expansion to PFCB.

In this chapter we present the process development on Ultem 1000 polyetheimide 3" substrate. The substrate thickness is 1.5 mm and has a CTE of ~56 ppm/^{o}C. While Ultem substrate was the best candidate for our purpose at the time of this effort, factors such as low thermal conductivity combined with a thickness larger than desired are the

source of complication in some fabrication steps. One of the main issues with using a thick substrate with low thermal conductivity in our process is excessive heating during ICP-RIE that changes the etch dynamics. The focus of our effort was to investigate the possibility of a small feature etch on Ultem substrates.

4.2 Ultem Substrate Preparation

The Ultem 1000 substrate was obtained in sheets and cut in a machine shop into circular 3” wafers. The surface roughness was measured using a Tencor P10 profilometer in 2 directions to be 15 nm and 1.4 μm.The surface was polished in the Center for Applied Optics (CAO) at UAH and surface roughness was reduced to ~20 nm in both directions. Figure 4.1 (a) and (b) show microscope images in the DIC mode of the substrate surface before and after polishing.

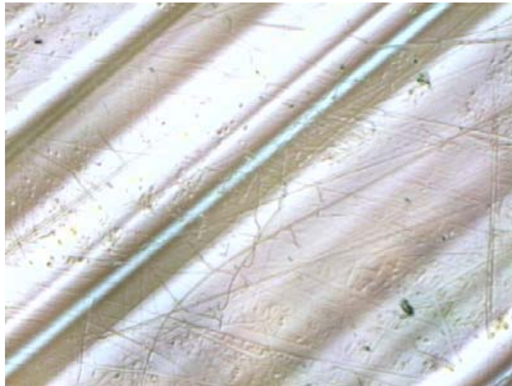

(a)

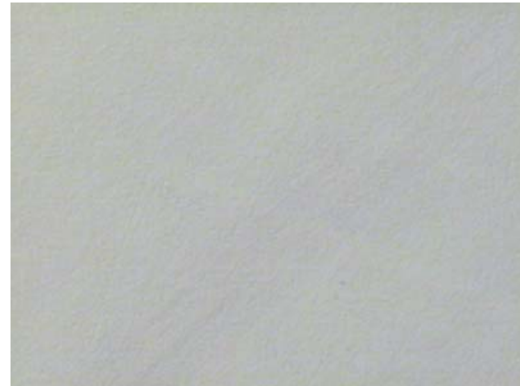

(b)

Figure 4.1 Ultem surface optical microscope image at 5x magnification (a) before polishing (b) after polishing.

A two stage dicing process was also developed to achieve a cut without chipping or polymer film delamination. Dicing is an important step that exposes the input and output waveguide faces for in and out coupling of light once waveguide devices are fabricated on the substrate. Figure 4.2(a) and (b) show successful dicing of Ultem and a microscope image of diced edge with no chipping or polymer delamination.

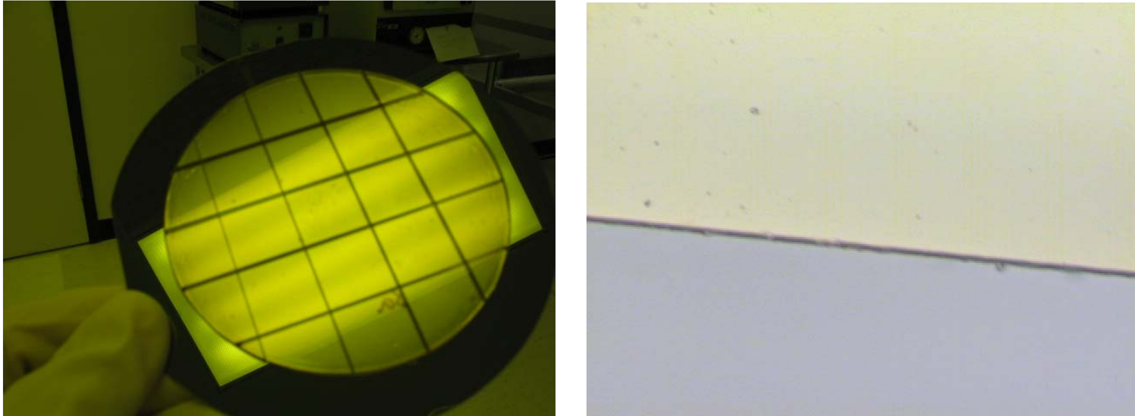

(a) (b)

Figure 4.2 (a) successful Ultem dice (b) 10x microscope image of diced edge

4.3 Aluminum Etch Development

The key issue in duplicating the already developed ICP-RIE aluminum etch on Ultem was to keep the process temperature the same as on silicon. The process temperature in the ICP-RIE is controlled by helium backside cooling of the platen with a Huber Unistat 140W cooler. Since the ICP only has carriers for 4" substrate, all smaller pieces are loaded on a carrier silicon wafer. The lack of direct contact between the main sample to be etched and the temperature controlled platen causes another hurdle for cooling the sample. We used a silver based thermal grease to improve the thermal contact

between the carrier wafer and the sample. Sample surface temperature can be measured during the etch process by placing a thermal strip on the sample covered with Kapton tape to prevent damage to the strip as seen in Figure 4.3.

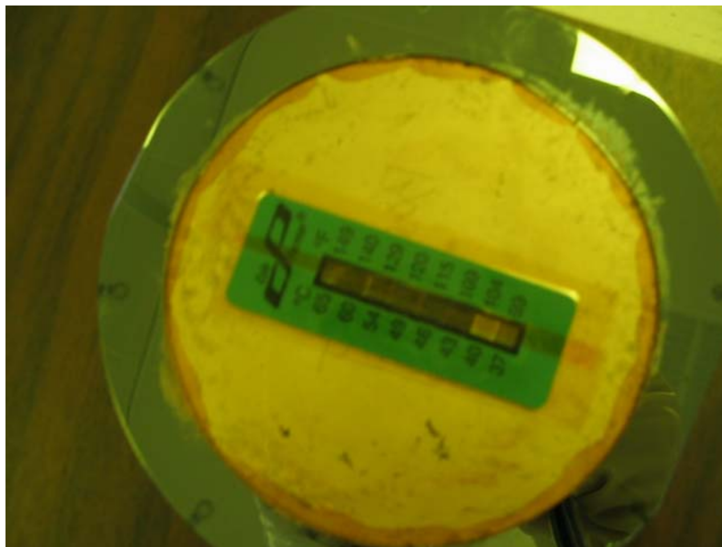

Figure 4.3 Surface temperature measurement configuration on Ultem substrate

Aluminum etch parameters on silicon substrate are as follows: 10 sccm Ar, 5 mTorr chamber pressure, 600 W coil power, 300 W platen power , 20 C platen temp, 7 minutes for 160 nm thick aluminum.

The surface temperature was first measured directly on a silicon substrate. The temperature reached equilibrium at 56°C after 3 minutes. The same etch except with platen temperature at 10°C was run on the Ultem substrate and the thermal strip read 110°C after 3 minutes. The platen temperature was then reduced to 0°C, but the heating effect was almost the same as in the latter experiment. Temperature measurements are shown in Table 4.1 for all three cases.

Table 4.1 Surface temperature measured on silicon and Ultem with different platen temperatures

During Argon Aluminum etch in the ICP/RIE								
	30 sec	**1 min**	**2 min**	**3 min**	**4 min**	**5 min**	**6 min**	**7 min**
Silicon Surface Temp. (20°C platen temp.)	46°C	49°C		56°C	56°C	56°C	56°C	56°C
Ultem Surface Temp. (10°C platen temp.)		65°C	77°C	110°C				
Ultem Surface Temp. (0°C platen temp.)	46°C	65°C	77°C	110°C	110°C	110°C	110°C	110°C

Even though the temperature was higher than desired, a test etch was run on the comb shape pattern on an 18x18 mm sample. We observed sparks at the corners of the sample 3 minutes into the etch. Figure 4.4 shows the sample after this etch. SEM images in Figure 4.5 showed that the narrowest features fully etched were 800 nm. This result was not satisfactory since we need features as narrow as 300 nm to be etched in order to achieve trench width of 800 nm after full the PFCB etch.

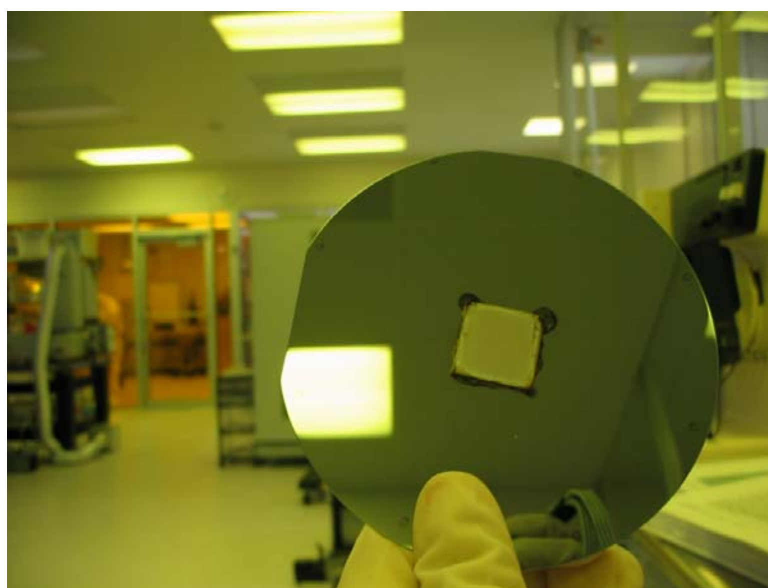

Figure 4.4 Sample burned at the corners during aluminum etch

The next step was to perform a stepwise etch with 1.5 minute etch time followed by 2 minutes with no plasma in the chamber. This kept the surface temperature at around 70°C, but there were still sparks at the sample corners.

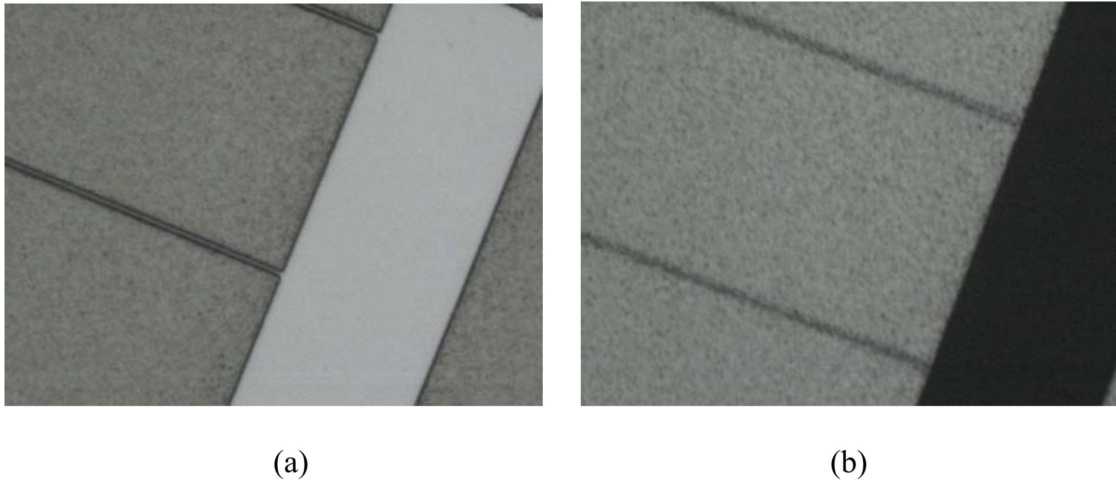

(a) (b)

Figure 4.5 After aluminum etch (a) 800 nm features fully etched (b) 300 nm features partially etched

The last experiment showed that reducing the platen temperature and cutting up the etch into shorter steps was helpful in reducing the surface temperature but were not enough to eliminate extreme heating. Due to the fact that this etch is designed to physically sputter out the aluminum etch mask, changing the coil or platen powers will not have a drastic effect on the nature of the etch except in the etch rate. We reduced the coil power to 300 W to decrease the initial energy of argon atoms that contributes to surface heating. The temperature test result is shown in Table 4.2. No signs of overheating or sparks were observed on the sample during the etch process. The results confirm that cutting the etch in 3 minute periods keeps the heating under control and should result in similar etch to that of on silicon (see Table 4.1 for temperature comparison).

Table 4.2 surface temperature during aluminum etch after reducing coil power to 300 W

During modified Al etch in the ICP/RIE					
	1 min	**2 min**	**3 min**	**4 min**	**6 min**
Ultem Surface Temp. (0^oC platen temp.)	40^oC	46^oC	54^oC	65^oC	99^oC

A comb shape pattern was etched on the Ultem substrate with the following parameters: 10 sccm Ar , 5 mTorr chamber pressure , 300 W coil power, 300 W platen power, 0^oC platen temp, 3 min etch 3 min rest pattern for a total 9 min etch time. Since the etch time was longer than before, ZEP 520 A (acting as etch mask for Al etch) did not hold up for the full duration of the etch. This problem was then solved by spinning a thicker, 800 nm film of ZEP as opposed to 500 nm before. Figure 4.6(a) and (b) show the etch results. The aluminum was fully etched on all feature sizes including 300 and 400 nm wide lines of our interest.

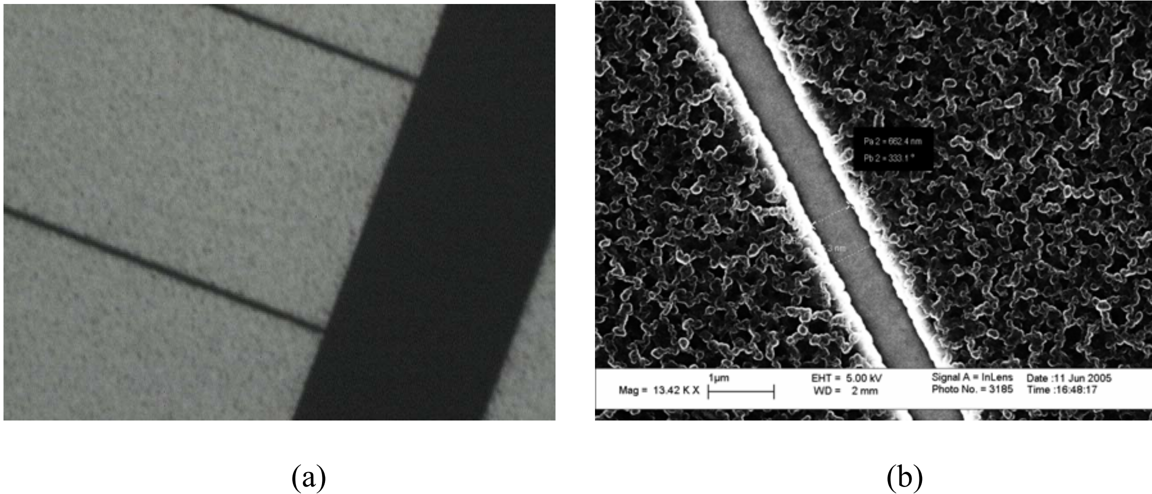

(a) (b)

Figure 4.6 Stepwise aluminum etch results on (a) 300 nm (b) 600 nm features

The aluminum etch process on top of the Ultem substrate was finalized by making the following changes:

- Platen temperature was reduced to 0^oC from 20^oC to reduce excessive heating during the etch
- The coil power in the ICP/RIE was dropped to 300W from 600 W to reduce the energy of argon atoms to prevent heating
- The etch was done in 3 minute steps with 3 minutes rest in between so that the temperature would not exceed 57^oC (the same as the sample temperature on silicon substrate). This increased the etch time to 9 minutes.
- ZEP 520 A film was made thicker to stand the extra etch time.

4.4 PFCB Etch Development

As for the aluminum ICP/RIE sputter discussed in the previous section, the key to having the desired PFCB etch on Ultem is to control the sample surface temperature. Unlike the aluminum sputter that was solely a physical process, the developed PFCB etch has a spontaneous chemical etch mechanism combined with sidewall passivation. The developed recipe carefully balances sidewall passivation and etch processes, so it is not desirable to change anything in the etch chemistry or coil and platen powers even if they contribute to reducing heat.

The temperature was first measured on a silicon sample using thermal strips while running the following recipe in the ICP/RIE: 25 sccm CO / 5 sccm O_2, 500 W coil power,

200 W platen power, 5 mTorr chamber pressure, 10°C platen temp, 54 minutes to achieve 14 μm deep, 800 nm wide trenches.

Surface temperature reaches equilibrium at 37°C after 5 minutes. The same experiment was repeated for an Ultem sample and equilibrium was reached at 65°C after 10 minutes.

Even though the sample was heating more than desired, a 30 minute test etch was run on comb shape patterns on the Ultem substrate. As seen in Figure 4.7, the etch roughness is increased and there is grass on the open etched areas. Sidewall verticality seems to be compromised as well.

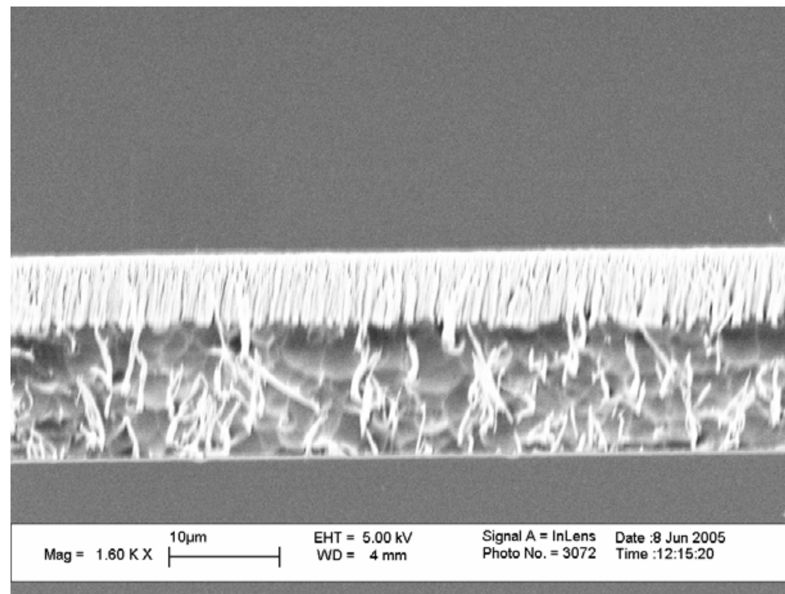

Figure 4.7 The PFCB etch result on Ultem without extra temperature control

The platen temperature was then dropped to 0°C and the surface temperature was measured during the etch. The surface temperature reached equilibrium at 40°C after 2 minutes. As shown in Table 4.3, the surface temperature for the Ultem with the platen at 0°C is very close to that of on top of silicon at 10°C. The latter recipe was used on

comb shape patterns for 40 minutes and the resultant trenches are shown in Figure 4.8(a) and (b). Figure 4.9(a) and (b) compare the sidewall smoothness and verticality on trenches with the same width on Ultem and silicon substrates. The etch rate is also the same as on silicon. The finalized ICP-RIE PFCB etch parameters on the Ultem substrate are 25 sccm CO / 5 sccm O_2, 500 W coil power, 200 W platen power, 5 mTorr chamber pressure , 0^oC platen temp, 54 minutes to achieve 14 μm deep, 800 nm wide trenches.

Table 4.3 surface temperature during PFCB etch after reducing platen temperature to 10^oC

During CO/O2 PFCB etch in the ICP/RIE								
	30 sec	**1 min**	**2 min**	**3 min**	**4 min**	**5 min**	**10 min**	**30 min**
Silicon Surface Temp. (10^oC platen temp.)	-	-	-	-	-	37^oC	37^oC	37^oC
Ultem Surface Temp. (10^oC platen temp.)	37^oC	43^oC	54^oC	54^oC	60^oC	60^oC	65^oC	65^oC
Ultem Surface Temp. (0^oC platen temp.)	-	37^oC	40^oC	40^oC	40^oC	40^oC	40^oC	40^oC

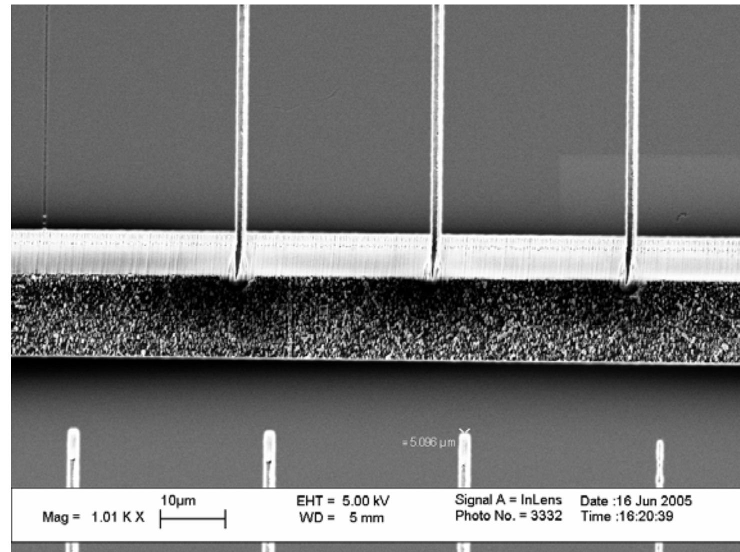

(a)

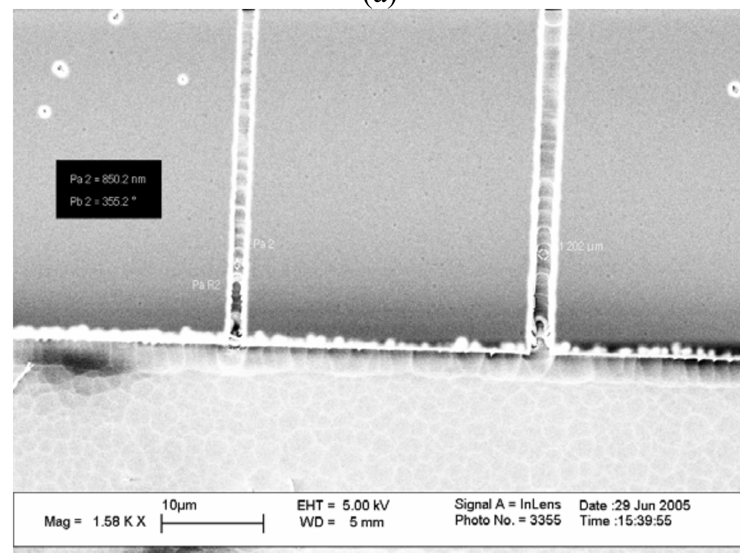

(b)

Figure 4.8 SEM images of 800 nm features after full PFCB etch (a) tilted cross section (b) top view

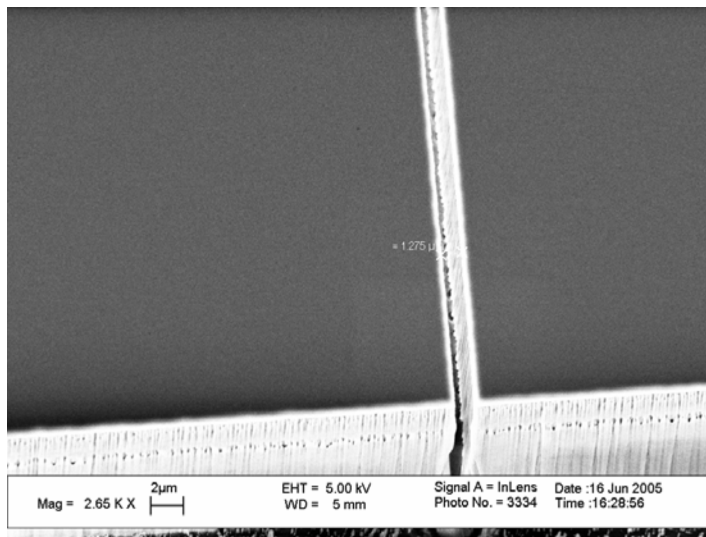

(a)

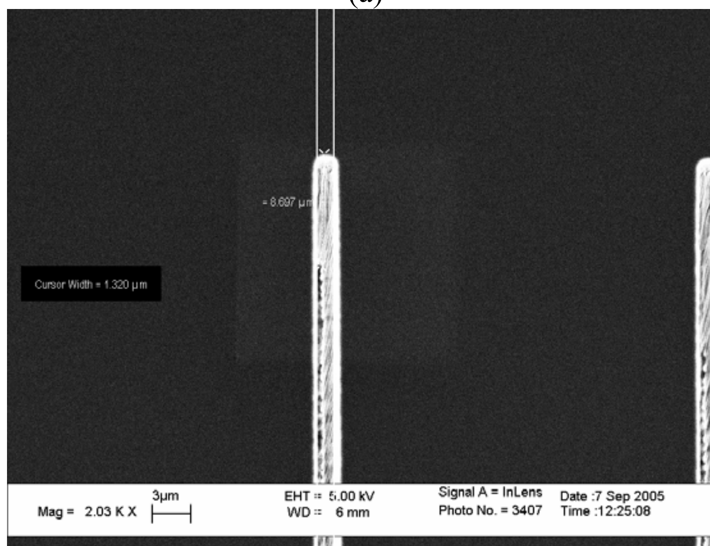

(b)

Figure 4.9 visual sidewall roughness comparison on 1.3 mm wide trenches etched on (a) Ultem substrate (b) silicon substrate

The PFCB small feature etch on top of Ultem was finalized by changing the platen temperature to 0°C compared to 10°C on silicon. This change allowed us to achieve surface temperatures very close to silicon and replicate the same small feature PFCB etch on Ultem.

4.5 Conclusion

We have presented small feature etch development for PFCB on top of Ultem substrates motivated by the elimination of stress related issues arising from silicon/PFCB CTE mismatch. To do this we have conducted surface temperature measurements during aluminum and PFCB etch and tried to keep the surface temperature on the Ultem the same as silicon substrate. The final etch processes were presented with very similar results on the Ultem.

Future research in this area includes full fabrication of waveguide devices using the narrow air-trenches as splitters on top of Ultem. In this research we focused on device fabrication on silicon substrate since most process steps are fully developed and approached stress related problems differently. However fabrication of our photonic devices on polymer or polyimide substrates is a very viable option that does not require much developing effort since the most challenging part (ICP-RIE etch step) is already developed.

CHAPTER FIVE

ULTRA COMPACT PFCB AIR-TRENCH WAVEGUIDE BEAM SPLITTER ON SILICON SUBSTRATE

In this chapter, the motivation, design and simulation, fabrication, and measurement of PFCB air-trench waveguide splitters are presented. The 90° splitter devices have a measured loss of 0.45 dB/splitter (90.1% efficiency).

5.1 Introduction

As discussed in the background section of this dissertation, compact planar waveguides circuits (PLCs) are difficult to achieve in low index contrast (LIC) material systems. To miniaturize PLCs, the size of bends and splitters as their fundamental building blocks needs to be reduced. Splitters are traditionally realized using Y-branches that require small angles and long tapered regions to insure a high efficiency splitting. We have previously demonstrated high efficiency and small area 45° single air interface bends in our group by etching 50 μm x 20 μm trenches at the intersection of two waveguides [10]. 2-D FDTD simulations show that high efficiency air-trench splitters can be realized by etching a narrow trench at the intersection of an input and two output waveguides [8]. The narrow air-trench partially reflects the light while capturing the

evanescent tail of the reflected light and transmitting it through. The etch required to fabricate these trenches is very challenging as we need vertical sidewalls and a 14 μm depth on trenches as narrow as 800 nm wide (aspect ratio of over 18:1). We have developed this etch with a CO/O_2 chemistry in the ICP/RIE and the use of stress relief trenches as presented in Chapter 3 of this dissertation.

In the following sections, we discuss the design of air-trench splitters and 2D-FDTD simulation results [8]. This is followed by a description of our fabrication process. In the last section, we report our measurement results.

5.2 Air-trench Splitter Analysis

We use a perfluorcyclobutyl (PFCB) copolymers waveguide structure whose core and clad refractive indices are 1.4816 and 1.4625. For single mode operation at a wavelength of 1.55μm, the core channel dimension of the waveguide is 3.6μm x 3.6μm. The waveguide size difference with what was presented in Appendix A is because here we use a different supply of PFCB core and clad with a different refractive index contrast and the waveguide was designed accordingly. The waveguide structure is approximated as a 2-D structure with a waveguide width of 3.6μm and a core refractive index of 1.4755 for the purpose of 2-D FDTD calculations [8].

Before presenting the 2-D FDTD simulation results, we present a “back of the envelop” calculation as a sanity check for the simulation. However, the results we achieve in our calculation are not expected to closely match the simulation results since they are all based on the assumption of a plane wave traveling in a material with the

effective refractive index of the core as opposed to the actual waveguide mode which can be considered to be composed of an angular spread of plane waves.

A T-junction (90 degree) configuration is first considered for its practicality. The purpose is to find the air trench width that can capture the portion of the evanescent tail for a 50-50 power splitting ratio. We consider a plane wave impinging upon the air interface at 45° which is larger than the critical angle, θ_c required for TIR (Figure 5.1).

$$\theta_c = \arcsin(N_{eff}) = 42.66^o \,. \tag{5.1}$$

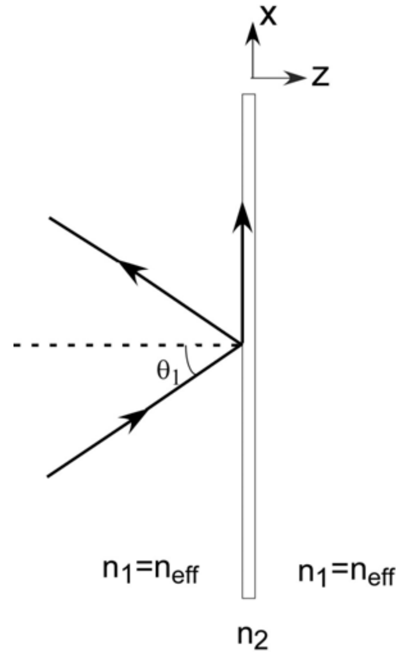

Figure 5.1 Schematic of a narrow splitter to catch the evanescent tail of the beam

We calculate the air-trench width required for 50% power transmission through the air-trench. The Evanescent tail of the field decays as $e^{-\beta z}$, where

$$\beta = k_2 \sqrt{(\frac{n_1}{n_2}\sin\theta_1)^2 - 1} \,. \tag{5.2}$$

$k_2 = 2\pi n_2 / \lambda$ is the wave number in the second medium (air) and n_1 and n_2 are the respective mode effective refractive index and air's, θ_1 is the beam incident angle (45°). Equation 5.3 determines how field decays as a function of distance from the first trench surface. However we are interested in power.

$$E \propto e^{-\beta z}. \tag{5.3}$$

The power drop is then given by equation 5.4

$$I \propto e^{-2\beta z}. \tag{5.4}$$

Solving equation 5.4 for a T= 50% and plugging into 5.3, we calculate z = 570 nm. This means we need a trench that is 570 nm wide and 14 μm deep which is extremely challenging to realize. Based on this data, for a 90 degree waveguide splitter configuration, a 50-50 power split is not an option. However, wider trenches that result in higher reflection are attractive option for splitters in our ring resonator configuration where an even power split is not required. For example a 740 nm trench width is calculated for 15% transmittance (85/15 splitting ratio). Again, these numbers only give us an idea and the devices will be designed based on 2D-FDTD simulation results.

To realize a 50-50 splitter, we can choose a larger splitting angle that makes a higher transmittance possible. This means the plane wave angle of the incident light will be less than θ_c calculated in equation 5.1 and the FTIR concept does not apply anymore. This case can simply be analyzed as a dielectric slab problem in which reflectance and transmittance are calculated based on multiple reflections (Figure 5.2). As mentioned before, this is only an analytical look at the working principles of the air-trench splitters and their behavior.

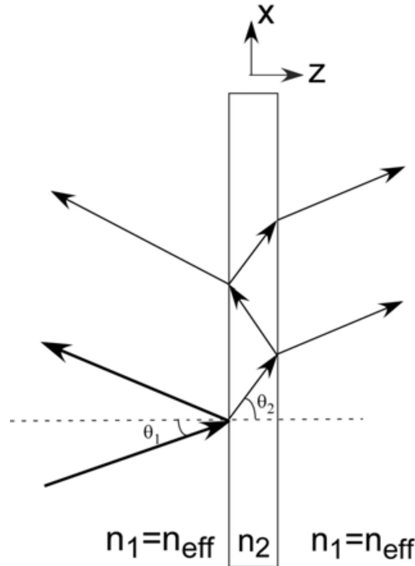

Figure 5.2 Multiple reflection and refractions on a dielectric slab when $\theta_1 < \theta_c$

For the 2-D FDTD simulation, a configuration as shown in Figure 5.3(a) was first considered and optical efficiencies at output waveguide Channels 1 and 2 were calculated as a function of the air trench width with a mode overlap integral (MOI) [8] (the optical efficiency is defined as the ratio of the power in the guided mode at the output detector to the incident guided mode power)[40]. Figure 5.3(b) shows how efficiency at each output channel changes as a function of trench width. According to the result, a 0.42μm wide trench is needed for a 50-50 splitting ratio. This requires etching trenches with over 33:1 aspect ratio and is not something we would like to attempt! However an un-even power splitter can be achieved with 0.8-1 μm wide air-trenches and used for a ring resonator as we do not need an even splitting ratio in the case of a RR.

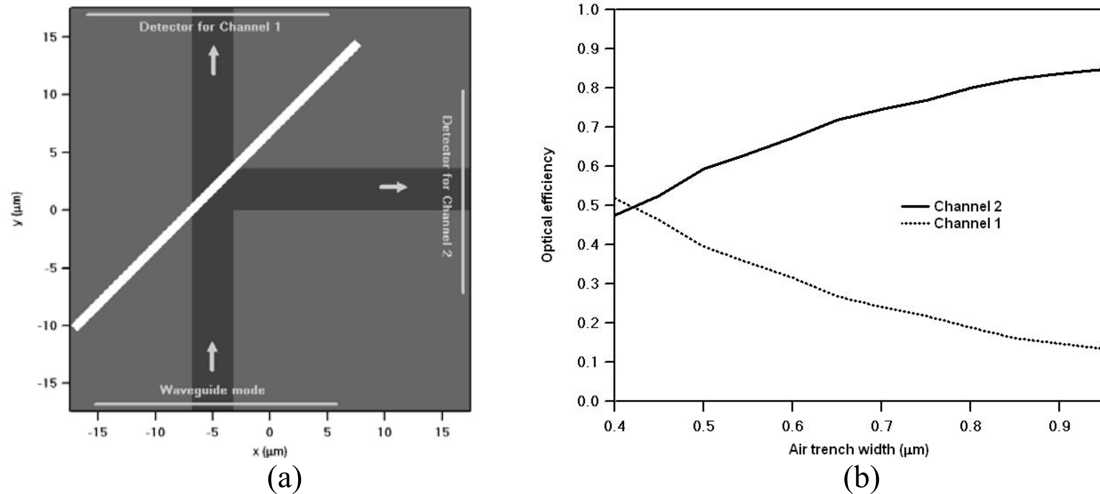

(a) (b)

Figure 5.3 (a) Geometry of splitter design with an air trench. (b) Optical efficiencies at output waveguide channels 1 and 2 as a function of air trench width. 50/50 splitting ratio is achieved with 0.42µm air trench width [8]

A 0.8 µm wide air trench was chosen for splitters in RR and later used in FDTD RR simulations [8]. However, later in fabrication we deviated to 850-950 nm wide trenches for the splitters. This changes the splitting ratio slightly. Simulation results predict a total efficiency of 98.7% with the respective 18.8% and 79.9% optical efficiencies at Channels 1 and 2 for an 800 nm wide splitter at λ=1.55µm. Figure 5.4(a) shows the magnitude squared time averaged electric field of such splitter. The spectral response of the splitter is shown in Figure 5.4(b) indicating reasonable uniformity over a 1.5-1.65 µm wavelength range [8].

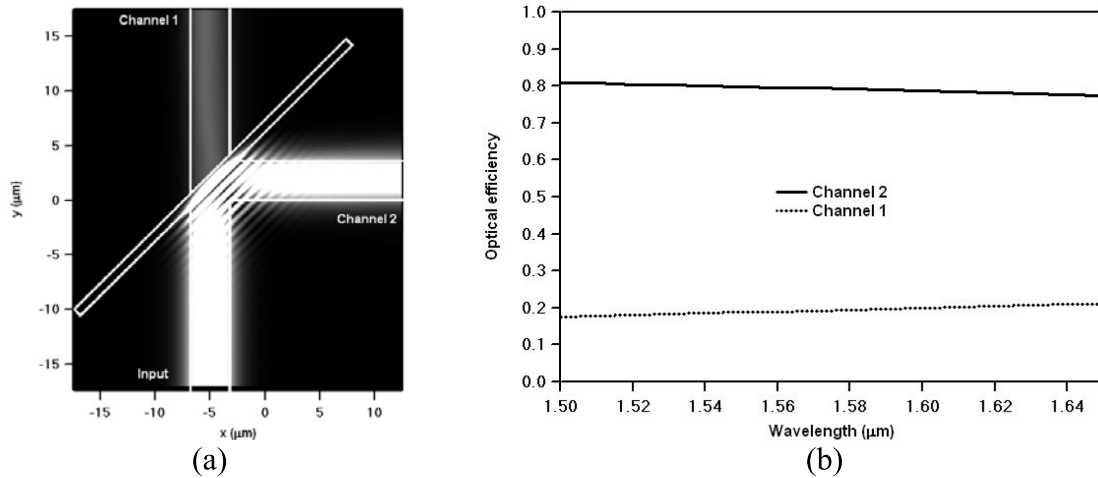

Figure 5.4 (a) Magnitude squared time averaged electric field of a splitter design for ring resonator at λ=1.55µm (TM polarization). Air trench width is 0.8µm. (b) Spectral response of the splitter design [8].

As explained earlier in this section, to achieve a 50/50 splitting ratio, we can change the geometry right angle so we do not have to etch the required 14µm deep [41] and 0.42µm wide air trench, which is not an easy task. An FDTD simulation was done keeping the air trench width at 0.8µm while changing the angle for the Channel 2 waveguide [8]. The final design with the magnitude squared time averaged electric field at λ=1.55µm is shown in Figure 5.5(a). The angle between Channels 1 and 2 is 107.5 degrees. The optical efficiencies are 48.5% and 48.1% for Channels 1 and 2. Figure 5.5(b) shows the spectral response of the splitter. The splitting ratio is uniform over the wavelength range of 1.50µm – 1.65µm.

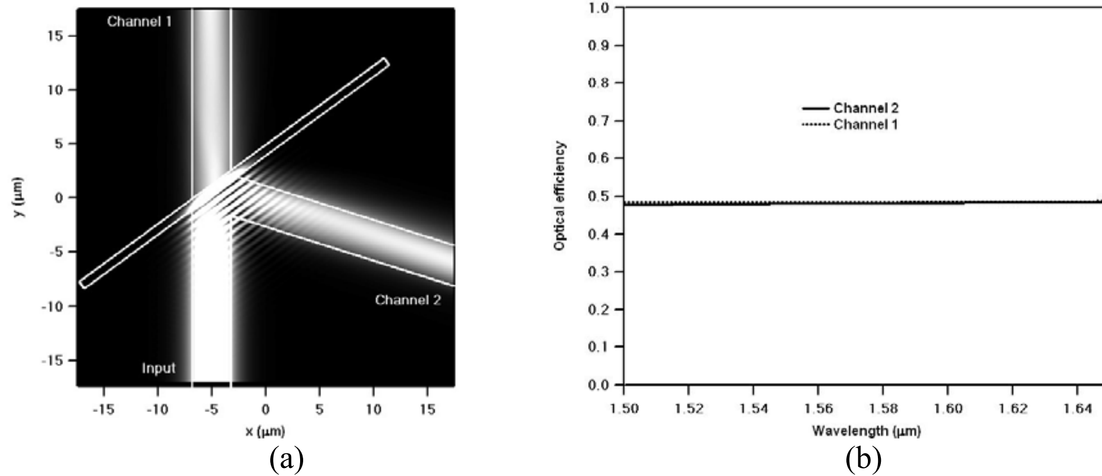

(a) (b)

Figure 5.5 (a) Magnitude squared time averaged electric field of a splitter for a Mach-Zender interferometer at λ=1.55µm (TM polarization). The air trench width is 0.8µm and the angle between Channels 1 & 2 is 107.5 degrees. (b) Spectral response of the splitter [8].

5.3 Mask Design and Fabrication

We fabricated the splitters described in Section 5.1 for measurement and characterization using EBL on top of the PFCB stack process mentioned in the background section. The details of the fabrication process will be presented in this section. The fabrication schematic is presented in Appendix B. We designed optical masks containing waveguide layouts appropriate for measuring splitting ratio and overall efficiency of the splitters. Also included are splitters and bends that are the building blocks of ring resonator and Mach-Zehnder interferometers as well as several ring resonators. In this section however, we will focus on 90 degree (85-15 splitting ratio) splitters used in ring resonators and 107.5 degree (50-50) splitters.

We designed separate splitter configurations for reflection and transmission measurement as follows:

- The reflection measurement configuration consists of equal-length waveguides that each have a different number of splitters that operate in reflection. The waveguide that carries the transmitted light is terminated at 15 µm past the splitter with an angled end-face to prevent the mode reflecting back into the splitter.
- The transmission measurement configuration consists of straight waveguides with different numbers of splitters on their path. The waveguide that carries the reflected light is terminated at 15 µm past the splitter the same as above.

Figure 5.6 shows the overall layout for both of these types of waveguides.

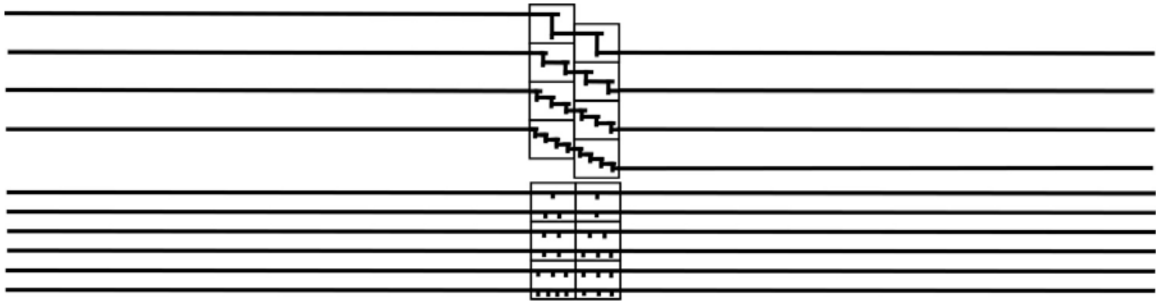

Figure 5.6 Reflection and transmission measurement layouts

To decide on the maximum number of splitters we can use in the above layouts, before the output power falls into the detector noise range, we did loss budget calculations. The following values are the basis of our calculation:

- Maximum input power = 1 mW
- Maximum output power reliably detected by our detector = 50 nW
- Fiber to waveguide coupling loss in each side = 60% adds up to 4.44dB
- Propagation loss = 0.4 dB/cm

From 1 mW input to 50 nW output there is a 43 dB budget out of which ~5 dB is spent on propagation and coupling losses leaving us with 38dB to spend on splitters.

Figures 5.7(a) and (b) show the calculated number of splitters for reflection and transmission configuration for 50-50 splitter and transmission of 80-20.

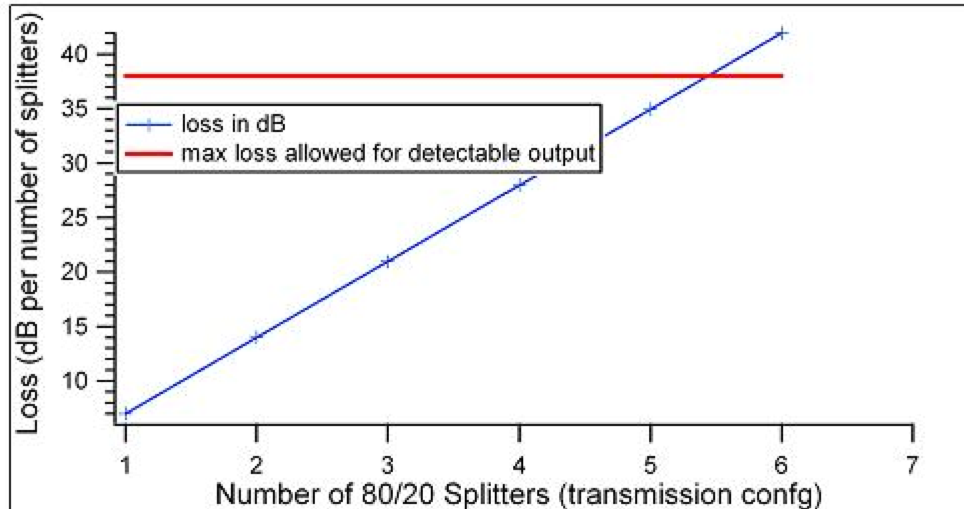

For 80/20 splitter with 20% transmission 1,2,3,4 and 5 splitter layouts can be used

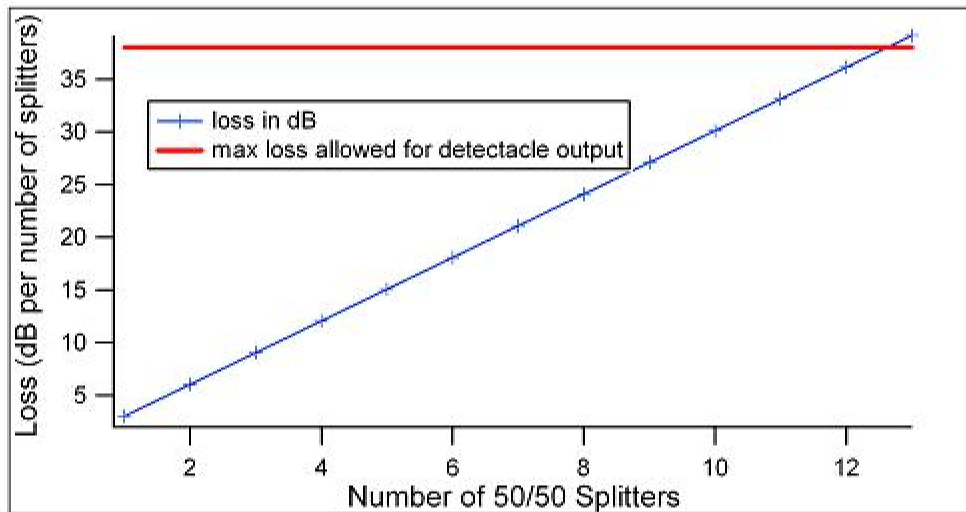

For 50/50 splitters, 2, 4, 6, 8,10 and maybe12 splitters can be used in the layout

Figure 5.7 Loss versus number of splitters for (a) 80-20 transmission configuration (b) 50-50 splitter configuration

According to our loss budget calculations for transmission configuration of 80-20 splitters, the maximum number of splitters we can use is 5. In the case of 50-50

splitters, 10 is the maximum for both reflection and transmission layouts that can be reliably measured.

To fabricate the splitter devices, we need three optical masks which were laid out using LASI 5 software and designed such that the pattern made by each one contains alignment marks to be aligned to the next mask. We needed to incorporate gold alignment marks in the same patterning step that we lay out the waveguides. The gold alignment marks are used later when splitters are patterned on top of the over-clad and need to be precisely aligned to the waveguides. The purpose of each mask will be explained as the fabrication process is discussed below. Figure 5.8(a)-(c) show the three masks in order of use while 5.8(d) show an example of a die layout. The squares surrounding the portion of the waveguide to be patterned with splitters shows the field size for e-beam lithography.

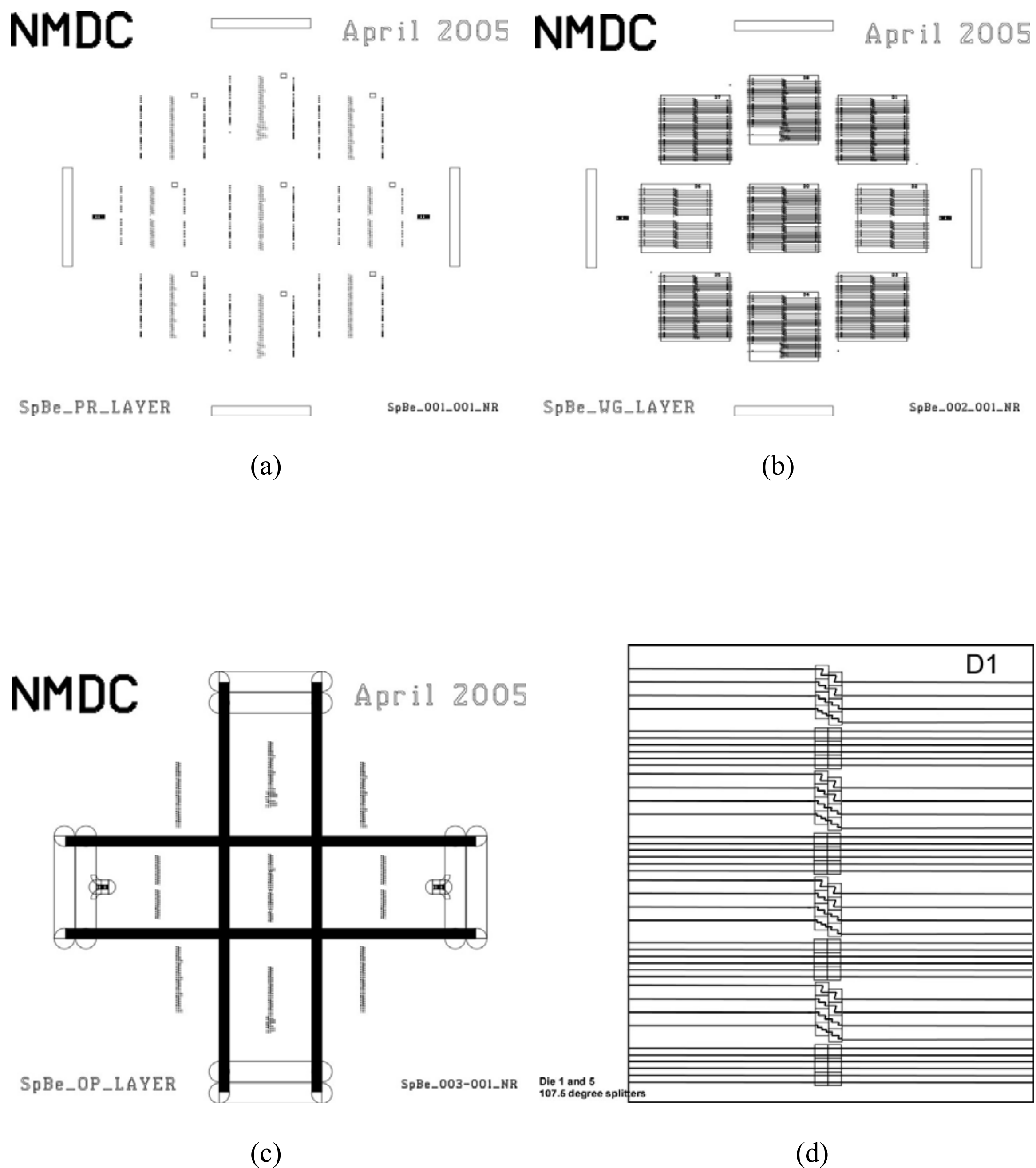

Figure 5.8 (a) protect mask (b) waveguide mask (c) opening mask (d) example of a die layout

We fabricated splitter devices in PFCB waveguides on a silicon substrate. First, a 10 μm thick under-cladding layer was spun and cured at 190°C followed by a 3.6 μm thick core layer. The spin and cure processes for PFCB was developed and presented in Appendix A. Next we patterned optical alignment marks and square patches at the corners of the e-beam fields where the alignment marks would later sit, using the "PROTECT" mask and AZ 701 MiR i-line photoresist (Figure 5.9(a)). Then we thermally evaporated a 100 nm gold film preceded by a 10 nm chromium film for better adhesion and lifted off in JT Baker PRS 1000 to have the square patches and optical alignment mark in gold (Figure 5.9(b)). Next, we deposited a silicon dioxide film as a hard mask for the waveguide etch with RF sputtering and patterned the waveguides and optical alignment marks as well as e-beam alignment marks using the "WAVEGUIDE" mask and the same positive photoresist. The silicon dioxide hard mask was etched in a CHF_3 chemistry with a inductively coupled reactive ion etcher (ICP RIE) followed by etching of the PFCB core layer in the ICP RIE using a helium and oxygen etch chemistry (Figure 5.9(c)). The gold patch around the e-beam alignment mark is also sputtered away during PFCB etch to outline them in gold (Figure 5.9(d)). After the waveguide core etch, the silicon dioxide layer was stripped in buffered hydrofluoric acid. The overcladding was then spun and cured at 190°C. An aluminum hard mask was thermally evaporated on top of over-cladding and openings were aligned and patterned where the gold e-beam alignment marks are embedded in the waveguide level using the AZ 701 photoresist. The aluminum was wet etched in aluminum etchant at 45°C followed by a PFCB etch through the opening using the same helium and oxygen chemistry to reveal the e-beam alignment marks (Figure 5.9(e)). The sample was diced into 9 dies which were individually

processed by RF sputtering of another layer of aluminum that increases the etch mask thickness as well as covering the sidewalls of the openings to avoid charging during e-beam lithography.

We then spun and cured ZEP 520A positive e-beam resist. The splitters were patterned at the designated positions with respect to the underlying waveguides with the aid of the gold EBL alignment marks.

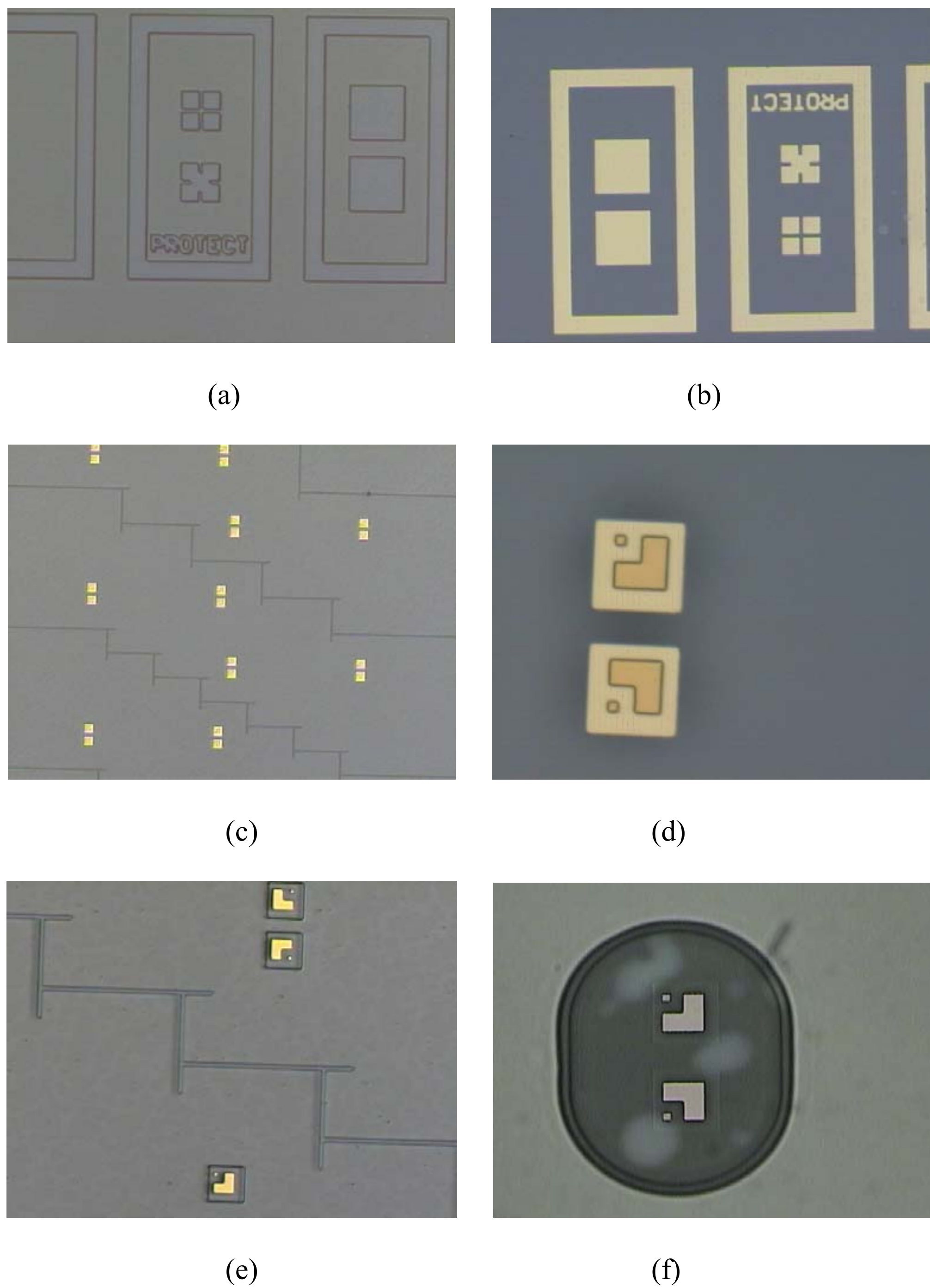

Figure 5.9 Optical microscope images of fabricated sample (a) after patterning with PROTECT mask (b) after lift off (c) after patterning with WAVEGUIDE mask (d) e-beam alignment marks after patterning WAVEGUIDE (d) after etching core (e) after patterning with OPEN ING mask and aluminum etch

We used the autoalignment feature of our in-house NPGS version 9 electron beam lithography system (JC Nabity Lithography Systems), which is used with a LEO 1550 field emission scanning electron microscope (SEM) to align and pattern the splitters. With placement of appropriate alignment marks in each of the four corners of an exposure field in the second optical lithography step (WAVEGUIDE mask), we achieve an alignment accuracy of less than 40 nm.

In the first iteration of the optical mask set, we used a 400µm x 400µm exposure field. After the first fabrication trials we found that ZEP 520A cracks around the alignment mark openings and the cracks often cut into the waveguides after the air-trench etch. The cracking is primarily caused by the stress in the thick stack of PFCB caused by CTE mismatch of PFCB and silicon substrate. Another problem was that the aluminum etch mask etched quicker around the opening and sometimes etched into the waveguides, since ZEP was thinner at that area. Figure 5.10 shows both problems. To reduce the chance of waveguide damage, we increased the opening edge distance to waveguides by making a second iteration of the mask set with a larger, 600µm x 600µm, exposure field.

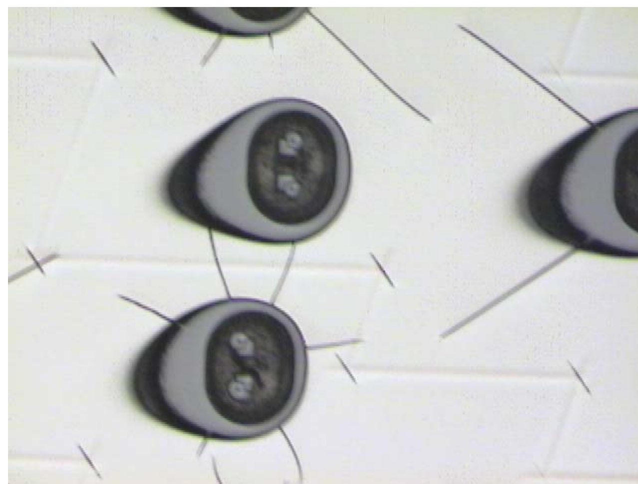

Figure 5.10 Cracking and over etching of the openings in 400 x 400 µm exposure field
The cracking problem was still damaging to the waveguide, with larger exposure field

We found that if the last layer of aluminum (deposited before ZEP is spun) is sputtered instead of evaporated, the cracking is reduced. We know that deposition through sputtering is less directional than evaporating, so the opening sidewalls are better covered in the case of a sputtered film. A conclusion can be made that the less contact ZEP 520A has with the PFCB, the better chance of sample survival as it appears that the solvent contained in the ZEP weakens the PFCB and makes it more vulnerable to stress. Figure 5.11(a) and (b) are taken after ZEP was spun on top of the sample covered by 80 nm evaporated (a), and 35 nm sputtered (b), aluminum. As we increased the thickness of the sputtered layer, the cracking reduced (Figure 5.11(c)). We also found that cracks are more severe when ZEP sits on the sample before the spin and penetrates through the thin aluminum layer into the PFCB film. The spreading step was taken out of the spin process and the spin process was started as the ZEP was being dispensed on the sample. Figure 5.11(d) shows the improvement. Inspecting the sample after each fabrication step showed that cracking happens after spinning the ZEP but increases during the developing step. Based on this observation, we cut the developing time by 20% while increasing the e-beam exposure dose by 20% to insure good pattern. With this we solved the ZEP cracking problem as shown in Figure 5.11(e) and (f). A few cracks still show up, but usually they are short and don’t cut into the waveguides.

Notice that there is a fine balance between increasing the aluminum thickness to reduce cracking and the aluminum etch time in the ICP RIE. ZEP acting as an etch mask in this process can only resist the argon plasma for a limited time based on the hard-bake temperature of the ZEP. If the aluminum film is sputtered too thick, the aluminum will not etch fully in the allowed ZEP resistance window. An attempt to etch aluminum fully

as the ZEP thins too much results in the opening to widen and cut into the waveguides.

This effect is shown in Figure 5.12.

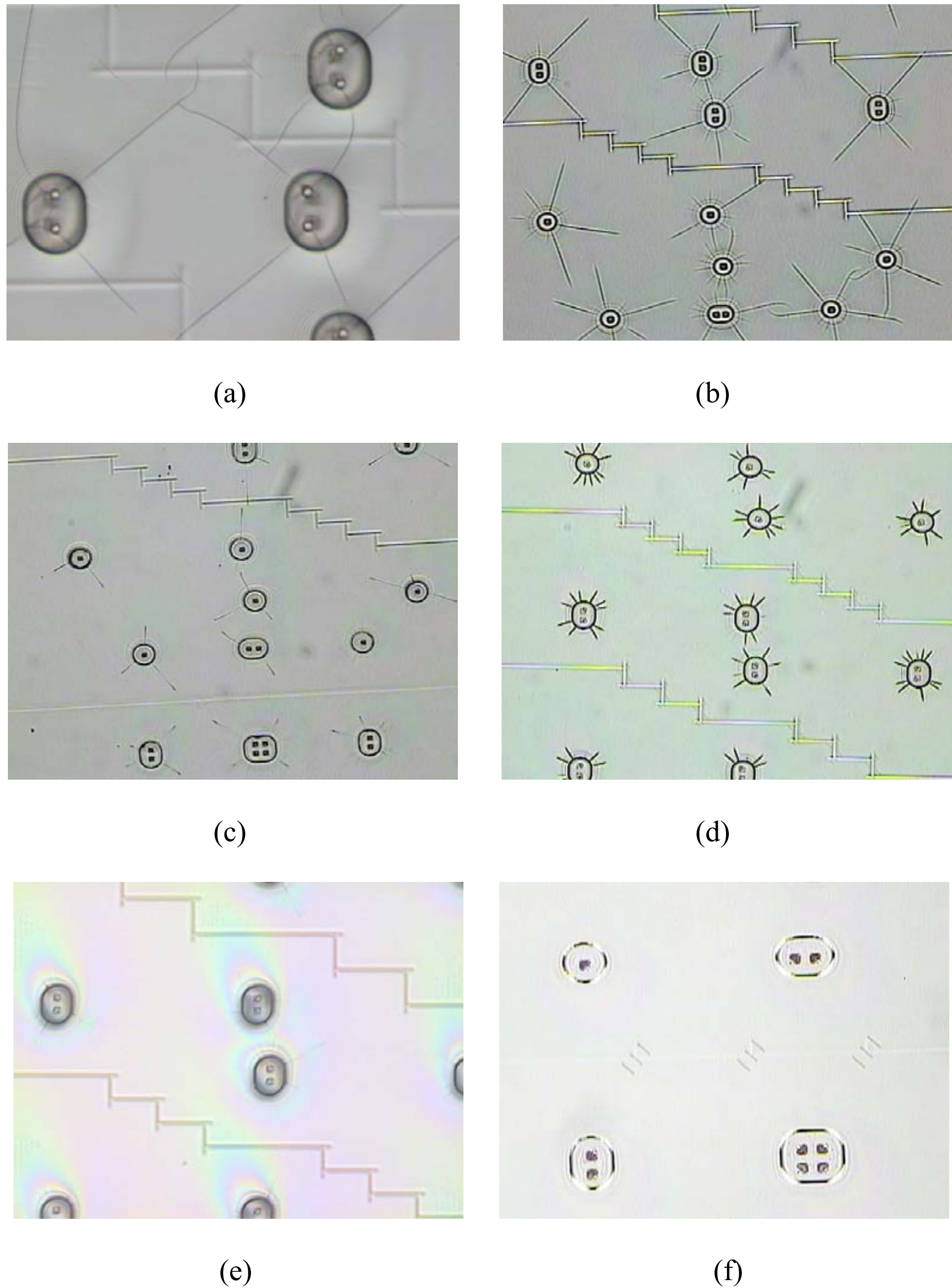

Figure 5.11 ZEP cracking problem as problem solving progress (a) with 80 nm evaporated aluminum (b) with 35 nm sputtered Al (c) 90 nm sputtered Al (d) 80 nm sputtered Al with pre-spin step eliminated (e) same as "d" with 95 nm sputtered Al (f) previous improvement plus reduced developing time

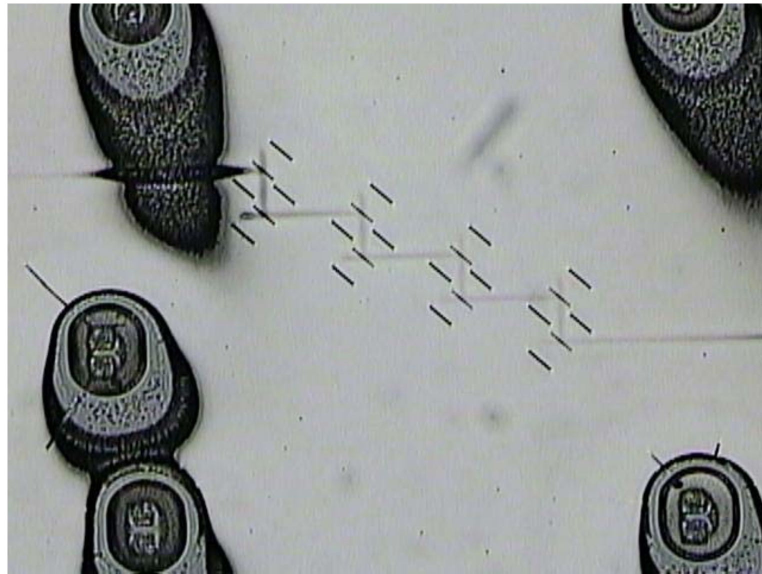

Figure 5.12 openings are over-etched as ZEP film etches away during an attempt to fully etch a thick aluminum film

Another fabrication problem was the pinholes we first noticed appearing after etching the trenches on some but not all samples. We found that the pinholes etch deep into the PFCB film during the trench etch. These deep holes cut into the waveguide in many places and such samples have no or very little waveguide output power. To find the root of this problem, we inspected the sample after each fabrication step starting from etching the openings. Figure 5.13 shows optical microscope images of the sample at various stages of fabrication. The pinholes appear after baking ZEP at 170°C for 30 minutes. Figure 5.13(c) shows an optical microscope image of very dense pinholes. Figure 5.13(d) shows an SEM image of the same sample. There are no signs of the problem on the ZEP surface and this suggests that the problem is the in the aluminum layer.

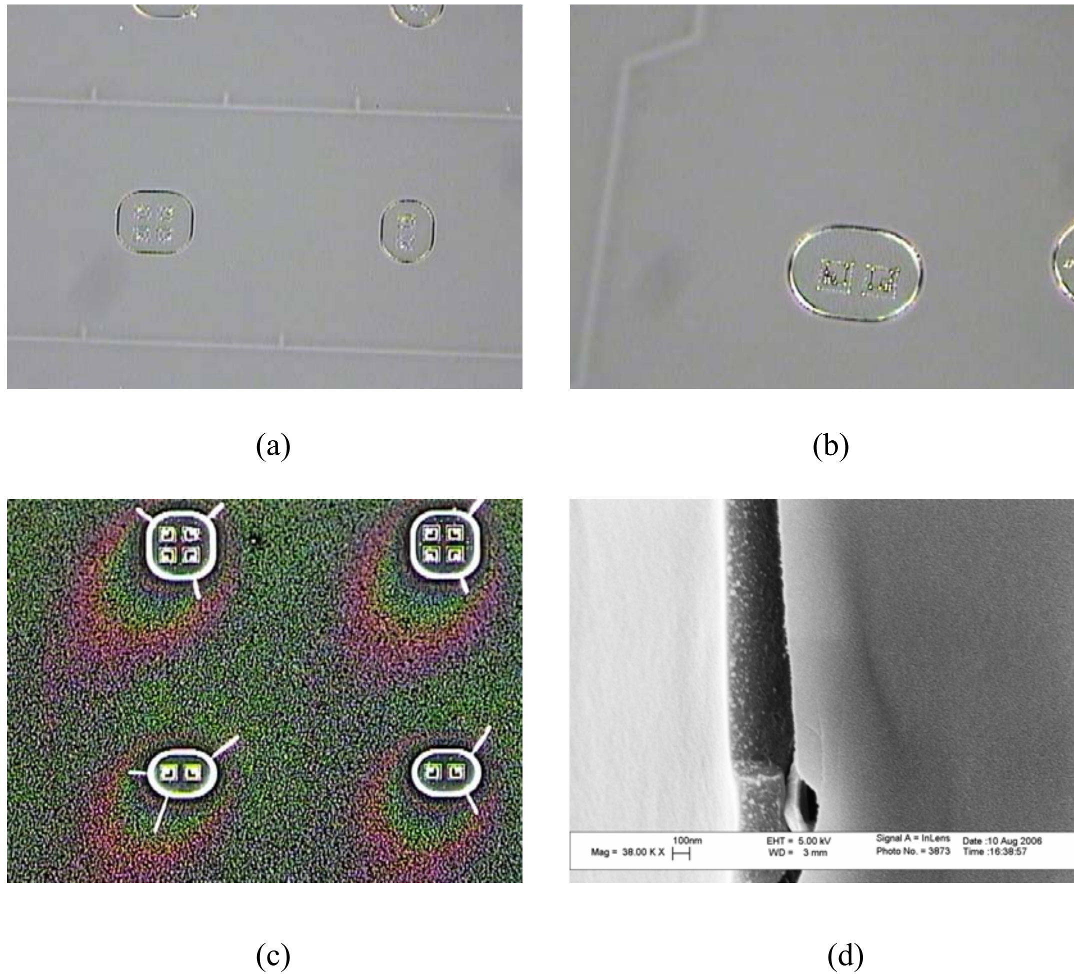

Figure 5.13 optical microscope images to pinpoint the appearance of pinholes (a) after sputtering 90 nm Al (b) after ZEP was spun (c) dense pinholes after 30 min bake at 170°C (d) Tilted top SEM image of the same sample showing the ZEP surface and the aluminum cross section through a crack: no sign on problem on ZEP surface

To find out whether or not this aluminum deformation is because of high temperatures, we reduced the bake temperature and found that density of the pinholes decreases with temperature. Figure 5.14(a) shows a sample baked at 140°C that has less pinholes. Figure 5.14(b) shows how the pinholes etch into the PFCB after the trench etch. We further reduced the baking temperature to 100°C which eliminated the pinhole problem. However, the etch resistance of ZEP was also reduced as expected. As shown in Figure 5.14(d) the ZEP film could not withstand the full aluminum etch. The pinhole

problem is an ongoing issue that is more prominent on some samples and less problematic on others. The measured samples were ones with less pinholes.

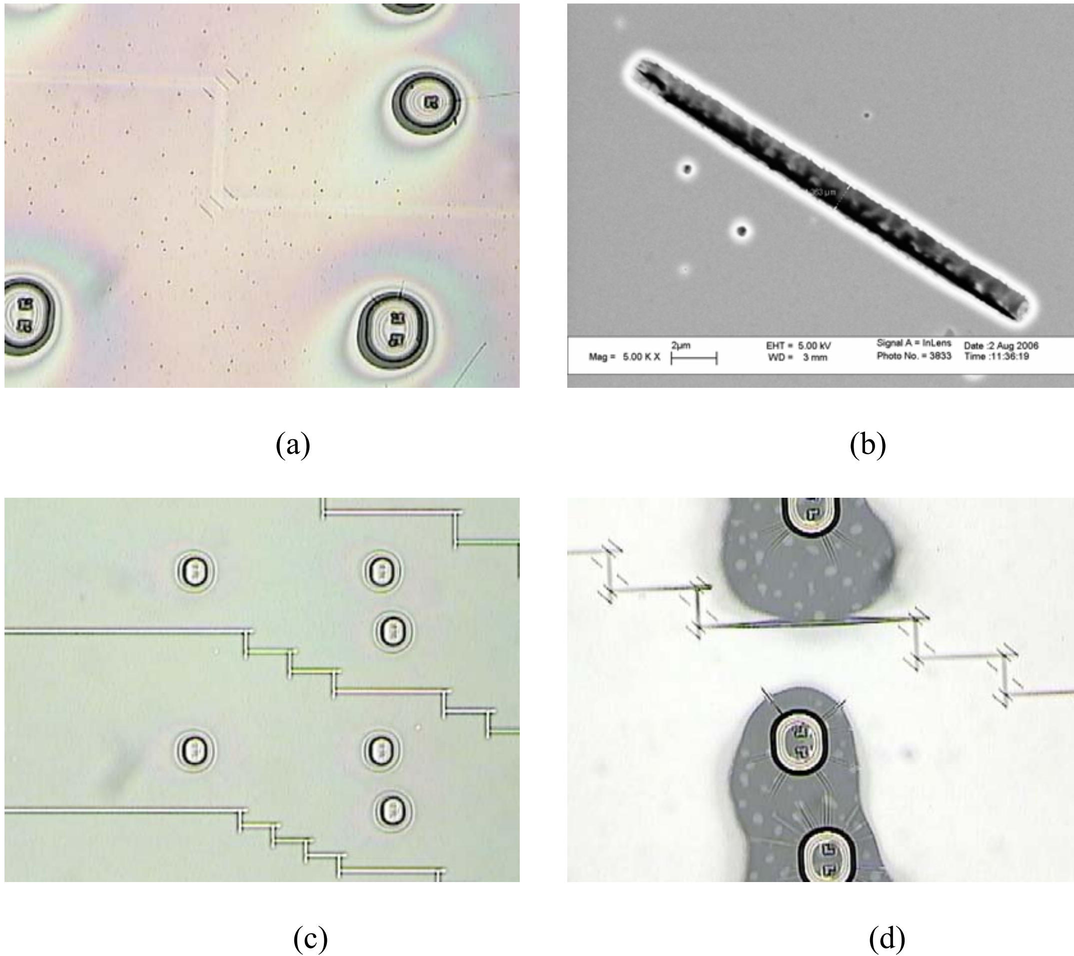

Figure 5.14 Temperature effect on pinhole density (a) less pinholes on sample baked at 140°C (b) appearance of pinhole after full trench etch (c) almost no pinholes on sample baked at 100°C (d) after aluminum etch: low ZEP resistance on sample baked at 100°C

5.4 950 nm Wide Splitter Measurement

A Newport PM500 Autoalign System was used to measure the optical power loss from a set of PFCB waveguides with different numbers of splitters in the reflection and transmission configurations. A wavelength tunable laser was used as a polarization light source with center wavelength at 1550nm. A polarization maintaining (PM) fiber was butt coupled into each input waveguide in turn. The output optical power from the device was butt coupled into a single mode fiber, which is connected to an optical power meter. Two computer-controlled precision 3-axis motion stages with 50 nm accuracy are used to optimize the input and output fiber position for highest throughput power.

Figure 5.15(a) and (b) show reflection and transmission efficiency for a 950 nm wide 90 degree splitter. The trenches on this sample were patterned 400 nm wide and 22 μm long. The aluminum etch mask thickness was ~150 nm, comprised of ~60 nm evaporated aluminum (left after the openings were etched) plus ~90 nm sputtered aluminum to cover the opening sidewalls. The aluminum sputter time in the ICP RIE was 5 minutes and air-trenches were etched with CO/O_2 etch for 60 minutes. The measured splitter loss at 1550 nm is 0.45 dB/splitter (90.1% splitter efficiency) for TM polarization. We repeated the measurement several times, the statistical error for the measurement in this system is ±0.02dB.

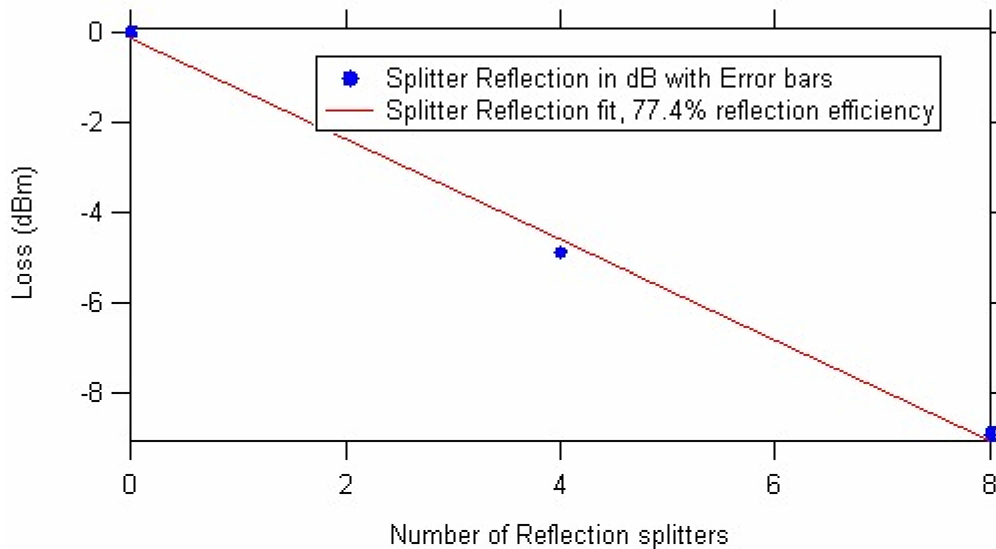

(a)

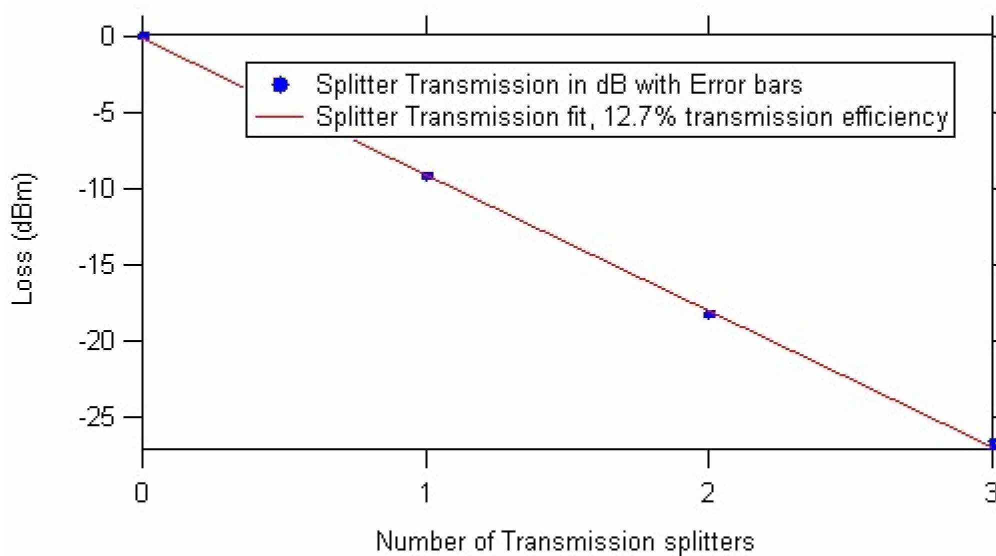

(b)

Figure 5.15 Splitter efficiency measurement (a) reflection efficiency (b) transmission efficiency. Note that error bars on the measured data are smaller than the marker size

The measured splitting ratio is 85.9/14.1 which is in very close agreement with the 2D-FDTD simulation results for a 950 nm trench which is 86.13/13.87. Figure 5.16 is the air-trench splitting ratio versus trench width for a 90 degree splitting configuration.

The red and blue lines are the simulated reflection and transmission, normalized to their sum. The green triangles are the measurement results.

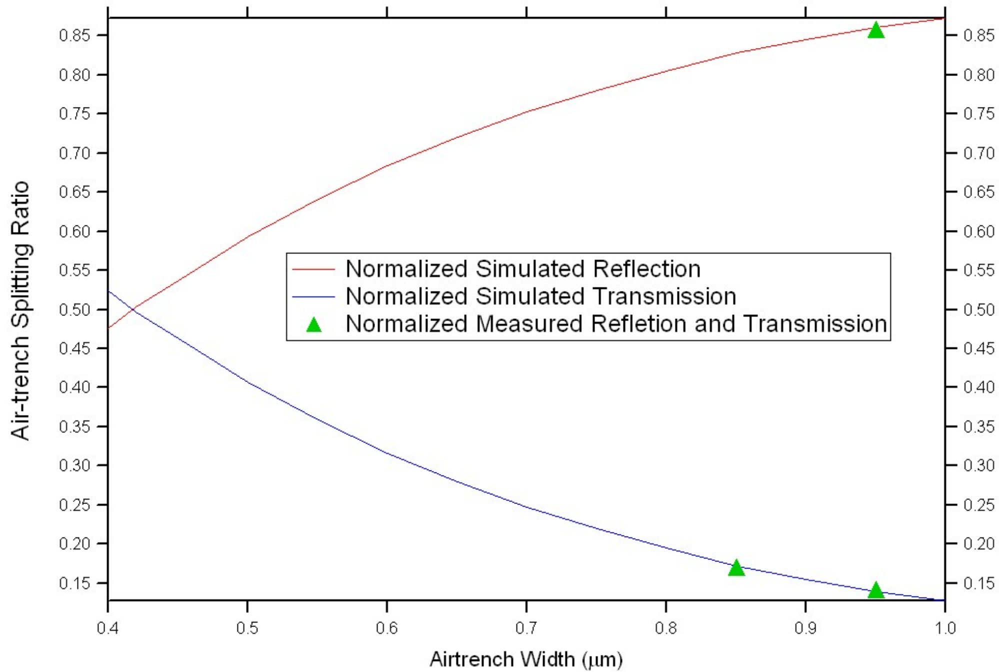

Figure 5.16 Air-trench splitting ratio as a function of air-trench width: 2-D FDTD results in solid line and measured data points in green.

It is important to note that we went through several fabrication iterations before achieving the performance presented above. We made a number of modifications, the most important of which are as follows:

- We changed the patterned width of the splitter from 250 to 400 nm while reducing the length from 30 to 22 μm. By increasing the width, we insured a full aluminum etch that improved the line edge quality and avoided partially etched trenches while reducing the length of the trench increased its mechanical robustness and

allowed less widening. This change increased the measured splitter efficiency from ~65% to ~84%

- We increased the etch time from 54 to 60 minutes which increases the depth of the trench. This increased the measured efficiency to 90.1%

A more detailed account of changes made in fabrication that resulted in higher efficiency splitters is presented in Section 7.3.

We believe that 50-50 splitters with a reflection angle of 107.5^{o} will show similar efficiency if fabricated since they are simulated with the same tools and require the same air-trench etch. We were unable to complete the fabrication of these splitters due to equipment issues.

5.5 Conclusion

We have presented results for compact high efficiency 90° splitters in PFCB waveguides. Frustrated total internal reflection is used to reflect part of the waveguide mode from an air interface while the evanescent tail is captured and transmitted through. Splitter design and tolerance analysis was done by Dr. Seunghyun Kim using 2-D and 3-D FDTD simulations. The fabrication process and fabrication results have been presented. Finally, experimental measurements show an achieved splitter loss of 0.45±0.02dB/bend for TM polarization.

We believe that 50-50 splitters with a reflection angle of 107.5^{o} will show similar efficiency if fabricated. Future research will focus on the fabrication of 50-50 splitters as well as trying to increase the splitter efficiency by reducing air-trench sidewall roughness

for CO/O_2 etch and using alternative SF_6/O_2 etch on silicon substrate. Also to avoid the stress related problems, the splitters can be fabricated on polyimide substrate using the etch developed in Chapter 5.

CHAPTER SIX

FABRICATION AND CHARACTERIZATION OF COMPACT RING RESONATORS IN PFCB

In this chapter we present the design, fabrication and characterization of ultra-compact PFCB ring resonators. We use the air-trench splitters detailed in Chapter 5 as well as air-trench 60 degree bends to realize the ring resonators.

6.1 Introduction

Ring resonators (RRs) have been studied for different applications, such as add/drop and band pass filters, wavelength division multiplexer/demultiplexers, and optical switches [24,42-46]. As mentioned in the background section, low index contrast (LIC) waveguides, such as silica and polymer waveguides, are attractive platforms for RRs because of their low propagation and coupling loss from and to fibers, and mature microfabrication processes [24, 42, 43, 47]. Large bend radius for high efficiency waveguide turns in LIC makes realizing compact RRs difficult.

We use the air-trench splitters demonstrated in Chapter 5 and air-trench bends to realize compact RR devices in PFCB. We present the design and simulation, fabrication and measurement for compact PFCB RR in this chapter. We discuss simulation results

and measured performance as well as a comparison between analytical and measured performance.

6.2 Ring Resonator Analysis and Simulation

The ring resonators are designed using small area air-trench bends and splitters [8]. The analysis of air-trench splitters was presented in Section 5.2. In this section we present the bend analysis followed by ring resonator design and simulation.

Air-trench bends are designed and simulated for RRs using 2-D FDTD [8]. The geometry of a bend structure is shown in Figure 6.1 in which the angle between the bisecting line of input and output waveguides is defined as the bend angle, θ. The intersection of the input and output waveguide lines is the origin, O, and the distance from the origin to the air trench wall is defined as the separation, S. It is positive when the air trench wall moves from the origin in a direction away from the bend. The S value that results in the highest bend efficiency is always negative because of the Goos-Hanchen shift at the air interface.

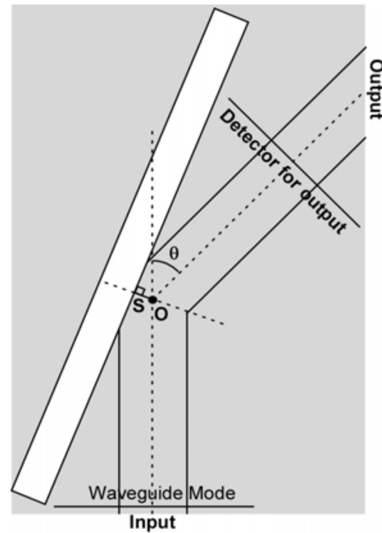

Figure 6.1 Geometry of a waveguide bend with an air trench. The position of the incident waveguide mode source is shown as well as the detector position along the output waveguide [8]

For waveguide material systems in which the core and clad refractive indices are relatively low, bend angles less than 90° are needed for all the planewave components of the mode to undergo TIR [10]. A bend angle of 60 degrees was chosen for the RR as shown in Figure 6.2. The angular spectrum of the waveguide mode is shown in Figure 6.3 with vertical lines corresponding to plane wave components at the critical angle for a 60 degree bend. Plane wave components on the right side of the vertical line satisfy the TIR condition for that particular bend making a high efficiency waveguide bend possible.

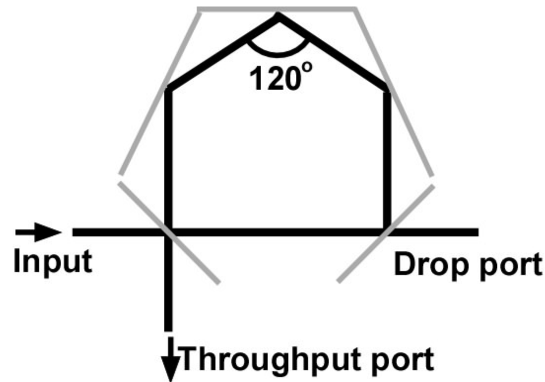

Figure 6.2 Proposed ring resonator combining small-area bends and splitters with air trenches [8].

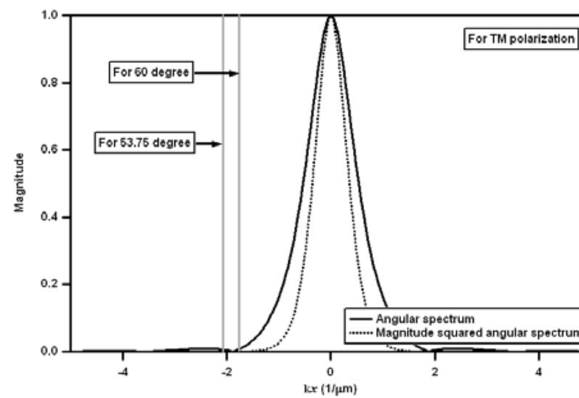

Figure 6.3 Angular spectrum. Vertical line corresponds to plane wave components at the critical angle for 60 degree bend structure [8].

The optimum trench interface position was found through FDTD simulation at S= -0.326μm for a 99.3% bend efficiency. Figure 6.4(a) shows the bend efficiency as a function of S at a wavelength of 1.55μm [8]. Keeping the air trench interface at this position, the bend efficiency as a function of the air trench width is shown in Figure 6.4(b). As the width increases, the amount of optical power transmitted through the air trench by frustrated TIR (FTIR) decreases exponentially [8]. We chose a 1.3μm wide trench for the bend, so the size is in the same ball park as the splitter trench,

minimizing the aspect ratio dependant etch rate difference. In this case, the bend efficiency is 99.2%.

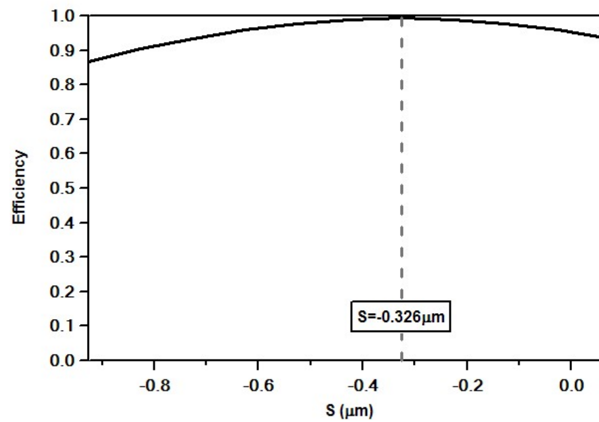

(a)

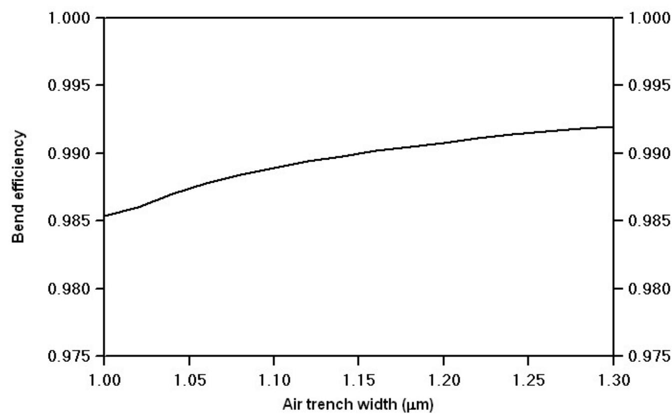

(b)

Figure 6.4 (a) Bend efficiency as a function of S. Bend efficiency at S=-0.326μm is 99.3%. (b) Bend efficiency as a function of air trench width [8]

Figure 6.5(a) shows the 60 degree bend geometry and the magnitude squared time averaged electric field for λ=1.55μm (FDTD result) [8]. Figure 6.5(b) shows the spectral response of the bend in 1.50μm to 1.65μm wavelength range.

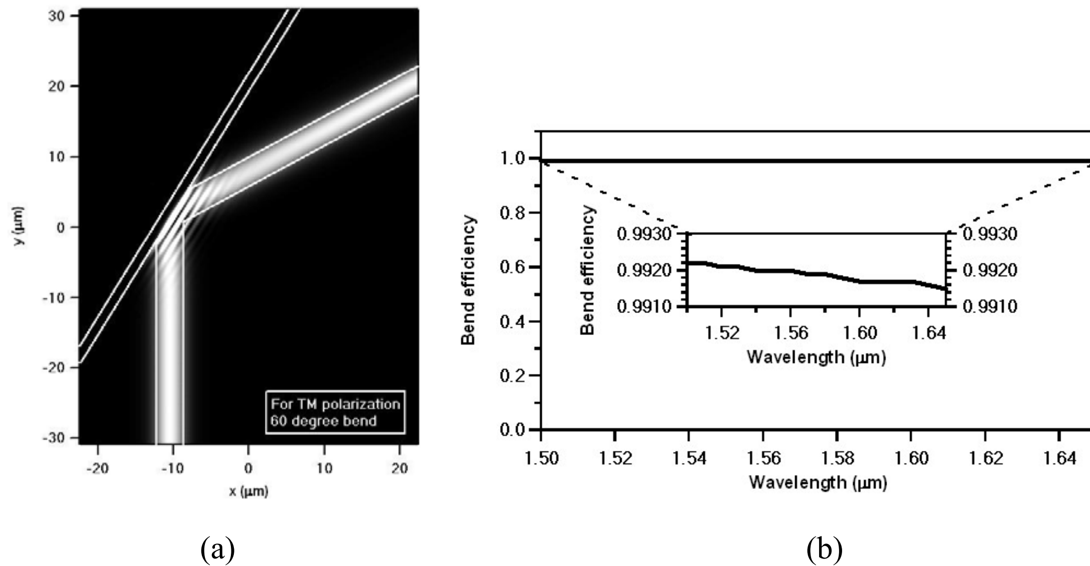

(a) (b)

Figure 6.5 (a) Geometry and magnitude squared time averaged electric field of the final 60 degree bend design at λ=1.55µm (TM polarization). (b) Spectral response (Inset magnify the calculated data region to show the data clearly) [8]

The final RR design occupies an area of only 70µm x 100µm. The simulated performance using FDTD is shown in Figure 6.6 [8]. The solid and dashed lines are the optical efficiencies at the drop and throughput ports. The optical efficiency at the drop wavelengths is 86%. The free spectral range (FSR) is 6.2nm and the full width at half maximum (FWHM) is 0.5nm. The Q factor is >3000. Figure 6.7 shows the magnitude squared time averaged electric fields at λ=1.5513µm (one of drop wavelengths) and λ=1.5549µm (one of throughput wavelengths).

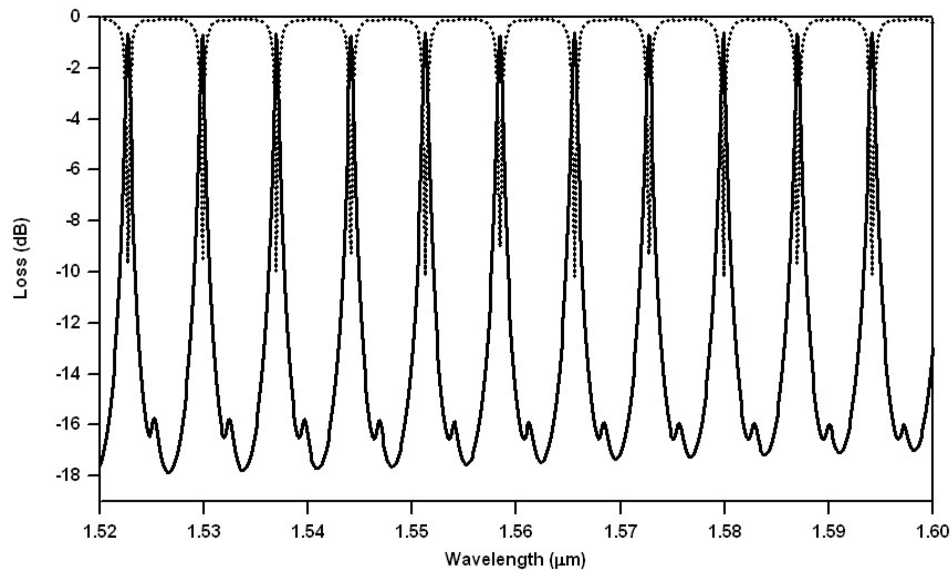

Figure 6.6 Spectral response of RR for the wavelength range of 1.52μm – 1.60μm (TM polarization) [8]

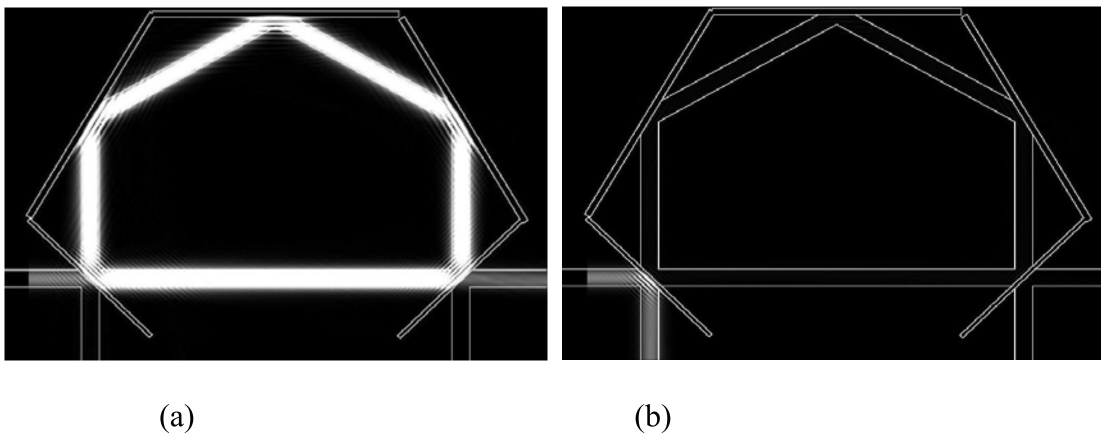

(a) (b)

Figure 6.7 Magnitude squared time averaged electric fields at (a) λ=1.5513μm (one of drop wavelengths) and (b) λ=1.5549μm (one of throughput wavelengths) [8]

6.3 Ring Resonator Fabrication and Measurement

We fabricated the ring resonators using the splitter and bend mask discussed in Section 5.3 and the same fabrication process (see Appendix B for process schematic). There are only 2 dies out of 9 on the mask that include ring resonators (three on each die). This makes achieving a well fabricated ring resonator a low yield proposition. In this section we present several ring resonators' fabrication and measurement. We present the fabrication problems in each iteration and the changes made to improve the performance of the next generation of device. All measurements were done using a Newport PM500 Autoalign System measuring the optical power from the drop and throughput port of the ring resonator while a Labview program was used to scan the wavelength on a tunable laser with the center wavelength at 1550nm. Light from a polarization maintaining (PM) fiber was butt coupled into the input waveguide and the output optical power from the device was butt coupled into a single mode fiber, which was connected to an optical power meter. The measured output power was recorded as the wavelength was scanned using a Labview program. Two computer-controlled precision 3-axis motion stages with 50 nm accuracy are used to optimize the input and output fiber position for the highest power before the wavelength scanning started. The maximization of power was done at a drop wavelength for the drop port and at a throughput wavelength for the throughput port. The wavelength was changed in 0.1 nm steps and we waited three seconds before taking data points after each step of change.

6.3.1 Core on Clad 173_Die0

The splitter was patterned at a 250 nm width using EBL. There was a mild pinhole problem (for more details on pinholes see Section 5.3). Air-trenches were etched 55 min with a CO/O_2 PFCB etch. All splitter and bend trenches were 30 μm long. Figure 6.8 is an optical microscope image of the measured ring resonator showing the waveguide structure underneath as well as the etched bends and splitters. The throughput port is redirected with two 45 degree bends. Figure 6.9(a) and (b) show the drop and throughput port optical power as the wavelength was varied over the range of 1530-1560 nm. The straight waveguide output power on this die was 140 μW while the maximum detected output for the ring resonator drop port was 1.6 μW. This shows quite a bit of loss inside the RR.

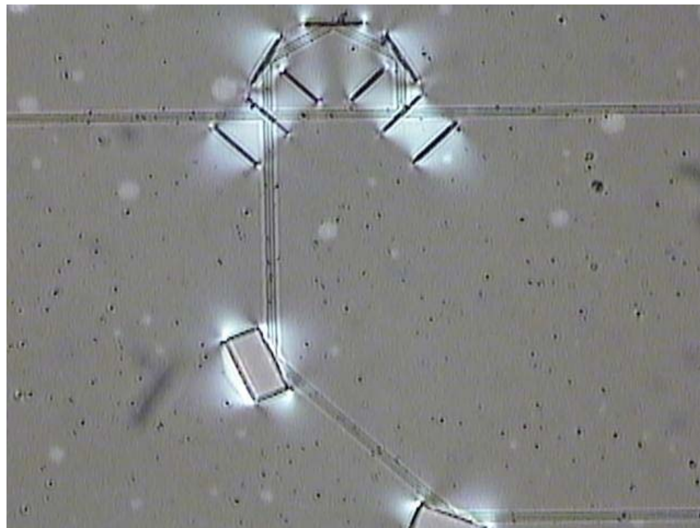

Figure 6.8 Optical microscope image (DIC mode) of the measured ring resonator

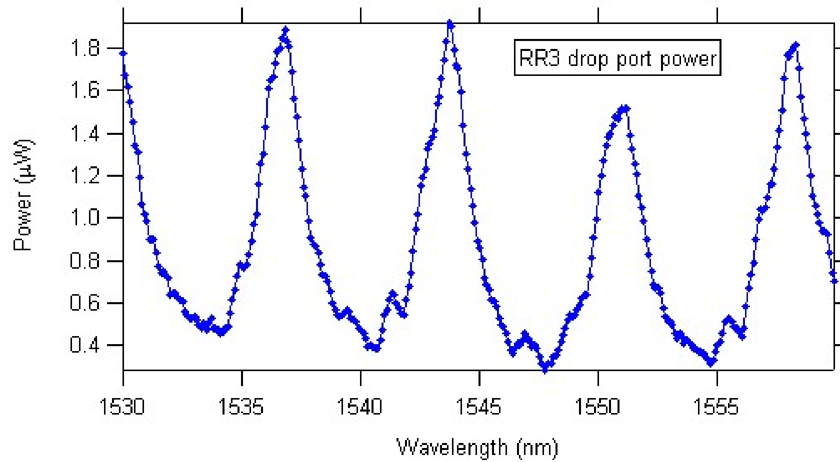

(a)

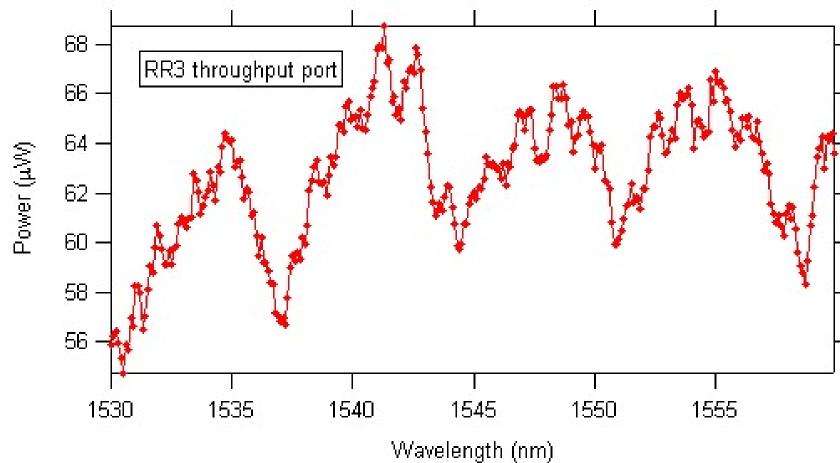

(b)

Figure 6.9 First ring resonator output power spectrum at (a) drop port (b) throughput port

There are problems in fabrication that are in part responsible for high losses:

1. The air-trench splitter shape has imperfections as a result of poor lithography or incomplete etching of aluminum etch mask. This is shown in Figure 6.10(a)
2. The stress relief features are too long (30 µm) and get too close to the waveguides. This is shown in Figure 6.10(c). The minimum distance required between the air-trench and the waveguide carrying the mode must be 7µm

because 99.99% of our waveguide mode power is contained in a 7μm radius around the waveguide axis.

3. The air-trench bends have two problems, both of which are shown in Figure 6.10(a):
   a. Air-trench bends are widened to over 1.7 μm instead of the desired 1.3 μm. This misplaces the bend interface by 0.4μm from one determined to have the highest efficiency by the Goos-Hanchen shift.
   b. Stress relief features were not used for air-trench bends and this has caused the belly shape widening in the middle of the trench.

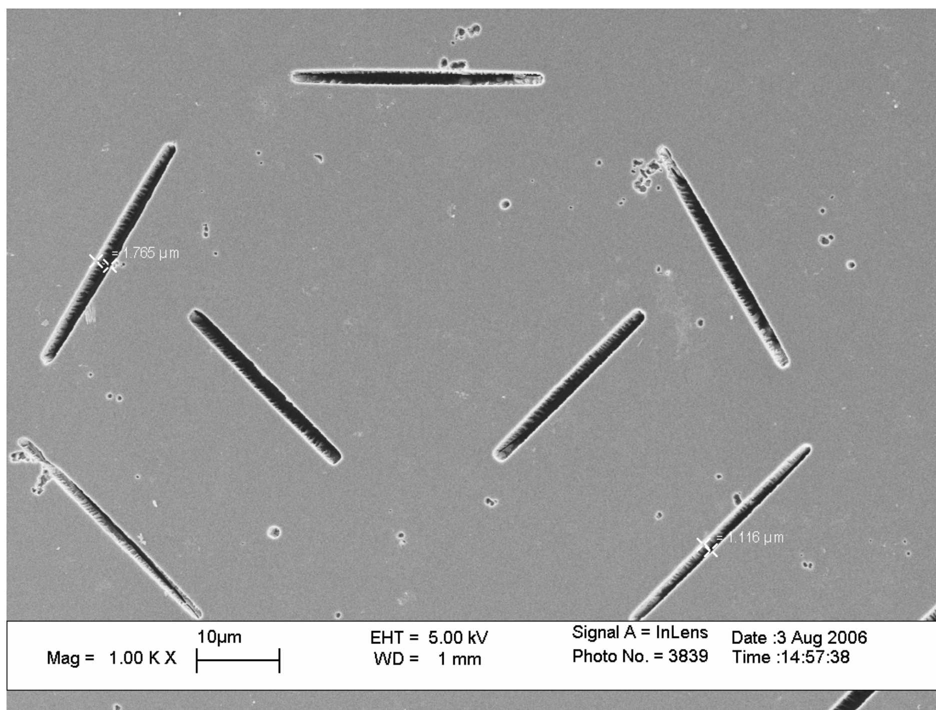

(a)

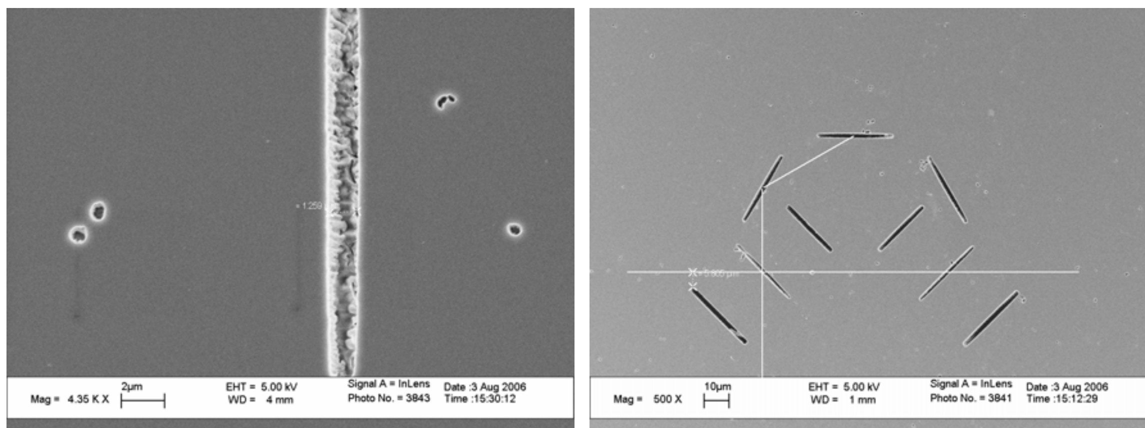

(b) (c)

Figure 6.10 Fabrication problems responsible for high losses in RR (a) poor line quality for splitter and mis-shaped and larger than desired bends (b) air-trench splitter line and etch quality (c) stress relief trenches coming too close to the waveguide

6.3.2 Core on clad 179_Die7

The three ring resonators on this die were fabricated to correct the problems on Core on clad 173. The following changes were made on one or more of the three ring resonators:

1. Stress relief trenches were added on the outer side of air-trench bends in RR1 and RR2 and on both sides on RR3 as seen in Figure 6.11. This improved the bends shape, especially in RR3 which was protected from both sides.
2. According to stress relief etch studies, shorter trenches have better mechanical stability and the stress related widening is smaller in them. For this reason we shortened the trench length on RR2 and RR3 to 22 μm, still long enough to fully capture the incoming mode. This change has two effects:
    a. The stress relief trenches do not interfere with the waveguide mode.
    b. The trench starting width can be larger since widening is less on shorter trenches. This extra width makes a full aluminum etch possible.

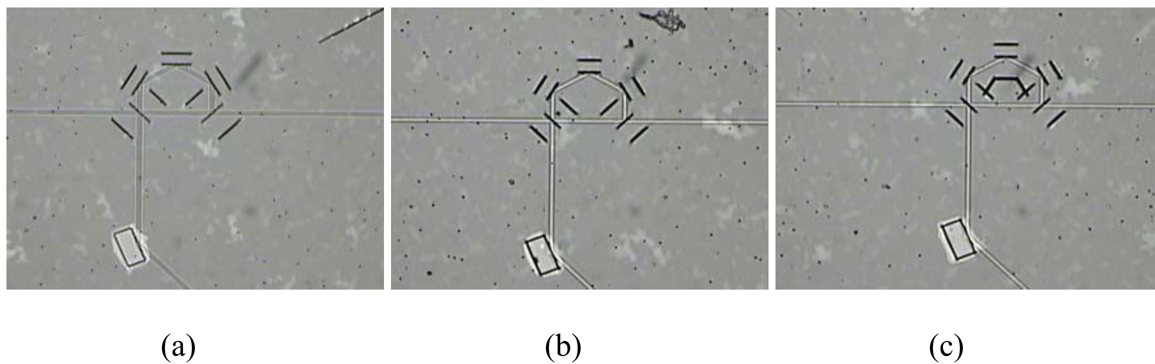

(a) (b) (c)

Figure 6.11 Optical microscope image of (a) RR1 (b) RR2 and (c) RR3

RR1 has 30 μm long splitters and bends. Splitters have 250 nm patterned width while bends are patterned at 650 nm with an outer stress relief trench. The after etch width of trenches are 870 nm for splitters and 1.1-1.47 μm for bends.

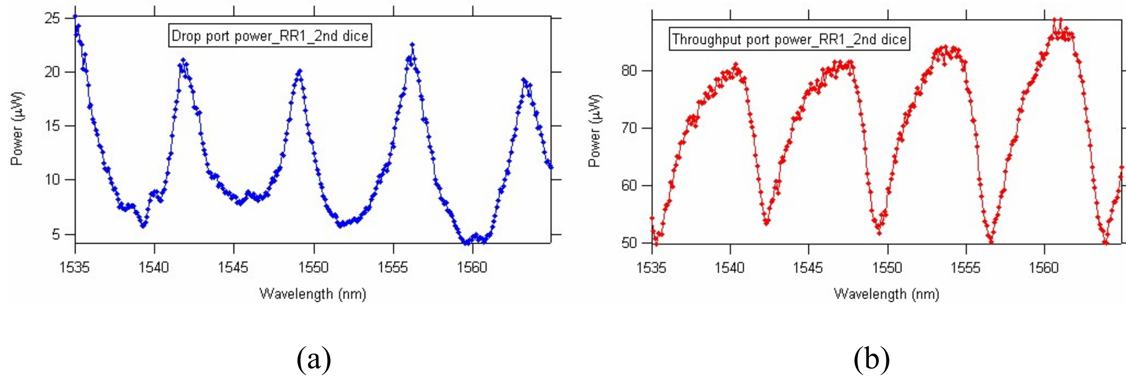

(a) (b)

Figure 6.12 RR1 measured power (a) drop port (b) throughput port

RR2 has a 22 μm long and 450 nm starting point splitters and 650 nm bends with only an outer stress relief trench.

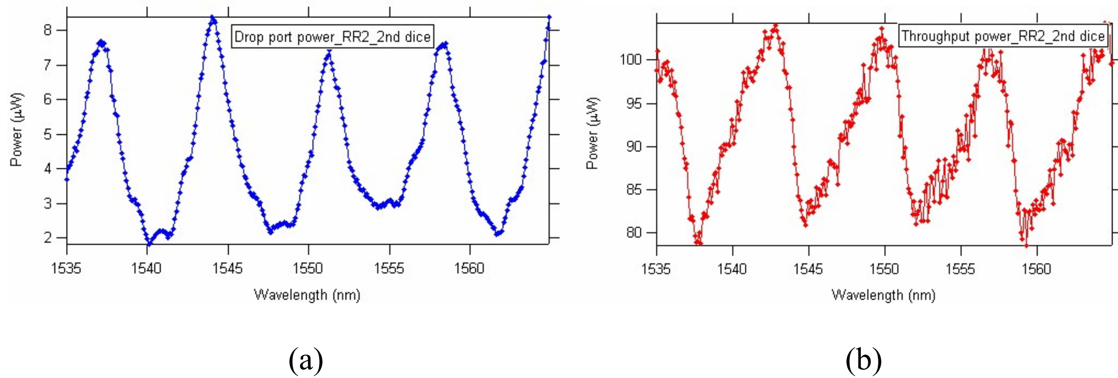

(a) (b)

Figure 6.13 RR2 measured power (a) drop port (b) throughput port

RR3 has 22 μm long with 400 nm patterned width splitters and 750 nm bends with stress relief trenches at both sides.

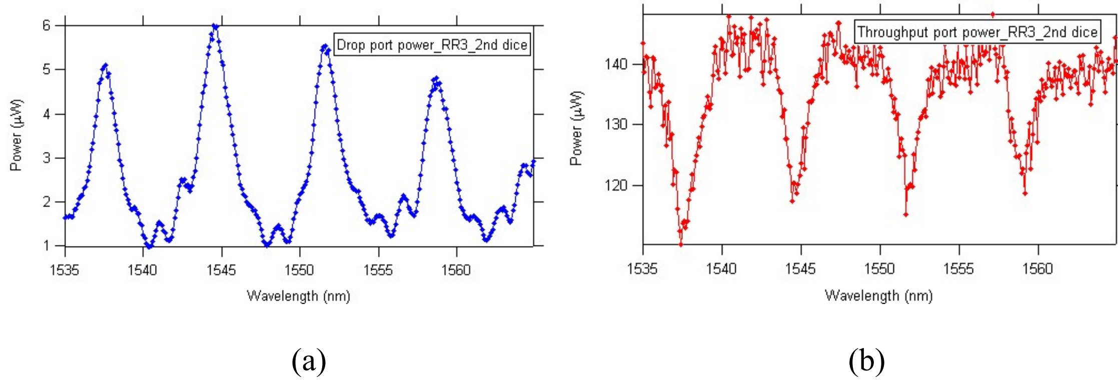

(a) (b)

Figure 6.14 RR3 measured power (a) drop port (b) throughput port

The lower efficiency in drop port in RR2 and RR3 as compared to RR1 is in large part a result of reducing the bend trench length to 21 μm while for a 60° waveguide turn this length is not enough to entirely capture the waveguide mode.

6.4 Measurement and Comparison to Analytical Result

In this section we explain the measured optical performance of our fabricated ring resonator. This is done by analytically calculating the performance and some key parameters of the ring resonator while changing the splitter and bend performance. Next we compare the analytical and measurement results for two specific ring resonators presented in the previous section.

6.4.1 Resonance Frequency and FSR

A mode of a certain frequency can exist in a lossless ring resonator only if the phase shift imparted by a single trip around the ring is a multiple of 2π:

$$\phi = kd = 2\pi q \qquad q = 1,2,3,.. \quad . \tag{6.1}$$

Therefore, the resonance frequency and wavelength are given by Equations 6.2 and 6.3

$$\nu_q = q\frac{c}{dn_{eff}} \tag{6.2}$$

$$\lambda_q = \frac{c}{\nu_q} = \frac{dn_{eff}}{q} \quad , \tag{6.3}$$

where c is the speed of light in vacuum, n_{eff} the waveguide effective refractive index and d the RR length. Our RR has a fabricated waveguide length of 229.5 µm and n_{eff}=1.4755. We calculated a resonance wavelength at 1560.49 as seen below in equation 6.4. However, the measured resonance frequency (see Figure 6.12) is different.

We explain this wavelength shift by the accumulated phase changes induced by bends and splitters in the RR. This total phase shift is calculated using equation 6.1 and assuming a total length of $d' = d + \Delta d$ for RR and finding the phase change $\Delta\phi$.

$$\lambda_{meas} = \frac{n_{eff} d'}{q}$$

$$\Delta d = \frac{q\Delta\lambda}{n_{eff}}$$

$$\Delta\phi = \frac{2\pi n_{eff}}{\lambda}\Delta d \ .$$

The $\Delta\phi$ is the accumulated phase shift inflicted by the 3 bends and two splitters in the ring.

The measured free spectral range (FSR) is ~7.2 nm which is very close to what is predicted by simulations.

6.4.2 RR Spectral Response as a Function of Splitter and Bend Performance

The losses in the RR increase as the bend and splitter efficiency decreases. Equations 6.5 and 6.6 are the analytical expressions for drop port and throughput port of our ring resonator,

$$\text{Drop port Efficiency} = \frac{T_S^2 \big/ (1-R_s R_b^{1.5})^2}{1+[4R_S R_b^{1.5} \big/ (1-R_S R_b^{1.5})^2]\sin^2\frac{\phi}{2}} \tag{6.5}$$

$$\text{Throughput port Efficiency} = R_s\left(1+\frac{T_S^2 R_b^3 - 2T_S R_b^{1.5}\cos(\phi) + 2T_S R_S R_b^3}{(1-R_s R_b^{1.5})^2 + [4R_s R_b^{1.5}]\sin^2\frac{\phi}{2}}\right. , \tag{6.6}$$

where T_s and R_s are the efficiencies at two different output channels of the splitter, R_b is the bend efficiency, $\phi = 2\pi n_{eff}(d+\Delta d)/\lambda$, d is the light propagation distance in the ring resonator, and Δd is the total effective propagation distance corresponding to the phase delays from bends and splitters.

To have a general idea of the change in RR performance versus bend and splitter efficiency, we calculated the ideal RR performance with bends and splitters at a maximum efficiency predicted by simulation in the dotted line and a much worse performance with 50% splitter and 90% bend efficiency in solid lines in Figure 6.15. The

drop port power is extremely reduced while the throughput power is at less than 50% with a low extinction ratio (i.e., shallow dips).

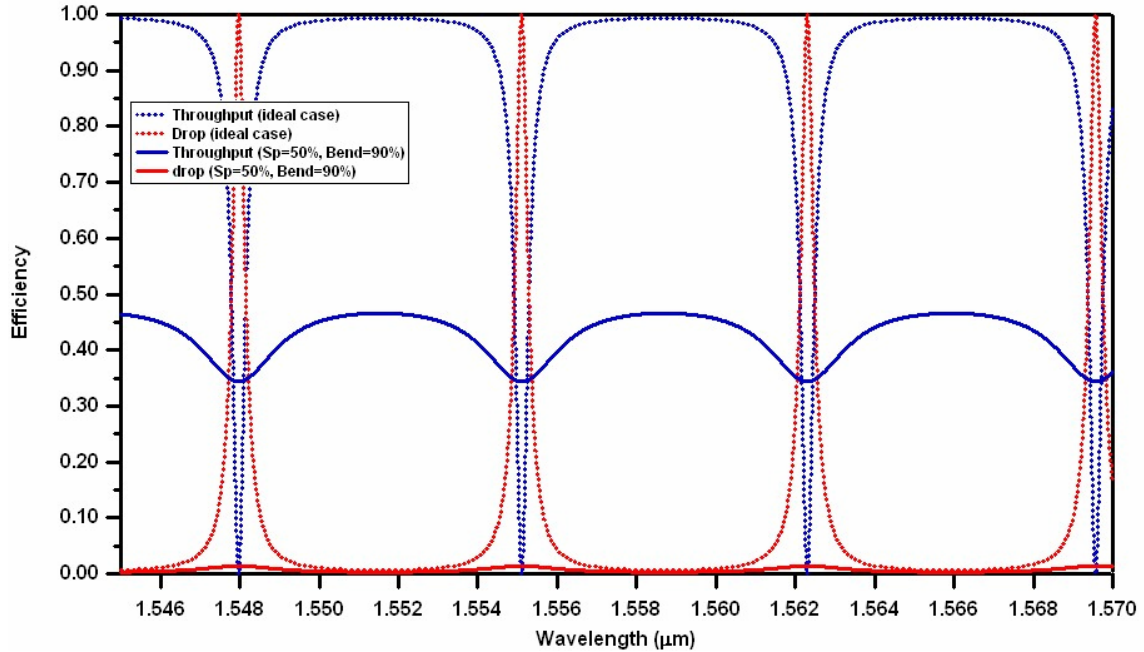

Figure 6.15 Drop and throughput port performance for ideal and less than perfect splitter and bend efficiency

We also studied how the peaks and valleys of both the drop and throughput port change as the splitter and bend efficiency varies. Figure 6.16(a) shows highs and lows of drop and throughput port efficiency as a function of splitter efficiency. Bends are assumed to be perfect. The following points are drawn from the graph:

1. The drop efficiency decreases very quickly as splitter efficiency drops.
2. The peak of throughput port efficiency varies linearly with splitter efficiency.

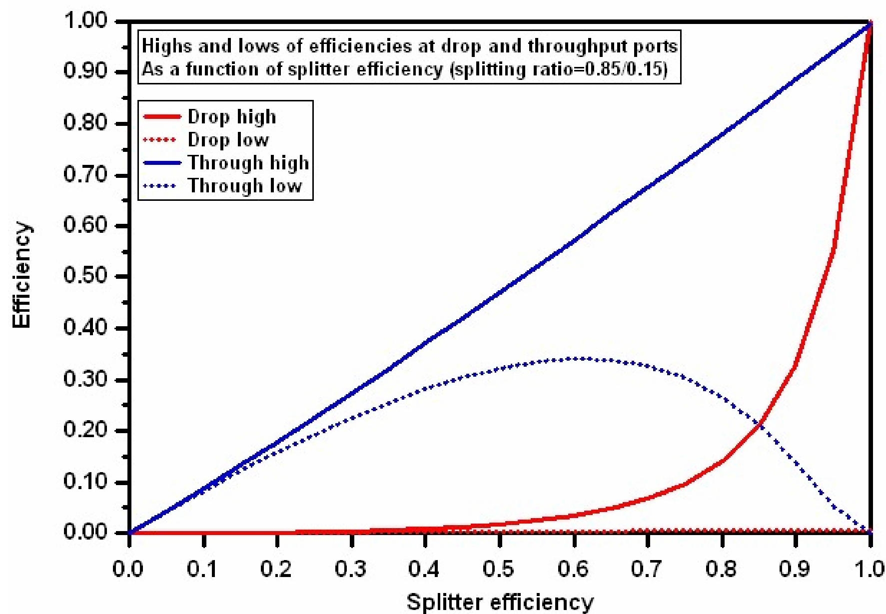

(a)

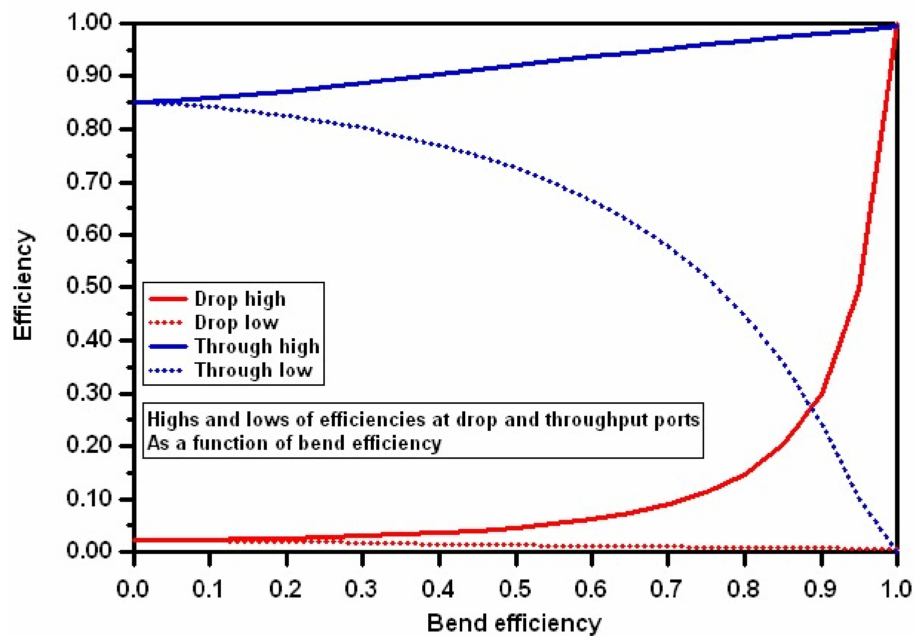

(b)

Figure 6.16 High and low of ring resonator drop and throughput port efficiency as a function of (a) splitter efficiency (b) bend efficiency

Figure 6.16(b) shows highs and lows of drop and throughput efficiency as a function of bend efficiency. This time splitters are assumed to be perfect. We notice the following:

1. Similar to the splitter case, the drop efficiency decreases very quickly as bend efficiency drops
2. Throughput port efficiency changes linearly but slowly compared to the change resulted from splitter efficiency drop.
3. Throughput port efficiency goes to 85% as the bend efficiency goes to zero which is the splitter's efficiency toward the throughput port.
4. Drop port efficiency goes to 2.25% as bend efficiency goes to zero which is the square of splitter's transmission since there are two splitters in this path.

The calculations for Figures 6.15 and 16 are done by Dr. Kim.

Analytical calculations were done for the best measured ring resonator (RR1). To numerically evaluate the drop and throughput ports, we used d = 229.5 μm (ring resonator length), n_{eff} = 1.4755 and we assume 84.5% splitter and 85% bend efficiency and a 85-15 splitting ratio. The splitter efficiency number used in the calculation is based on the measured splitters on the same die as the ring resonator and the bend efficiency is from rough bend measurements made on dies from the same sample. The straight waveguide output power is 300 μW. Figure 6.17(a) and (b) are the measured and calculated drop port power versus wavelength. Figure 6.18(a) and (b) are the measured and calculated throughput port power.

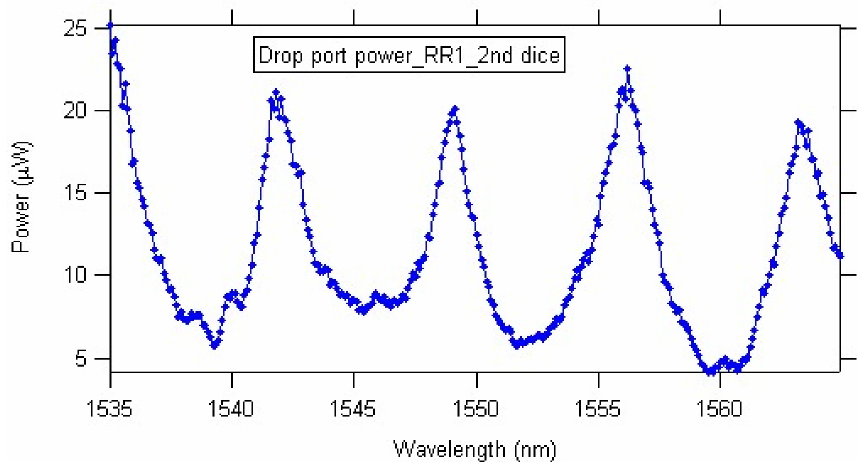

(a)

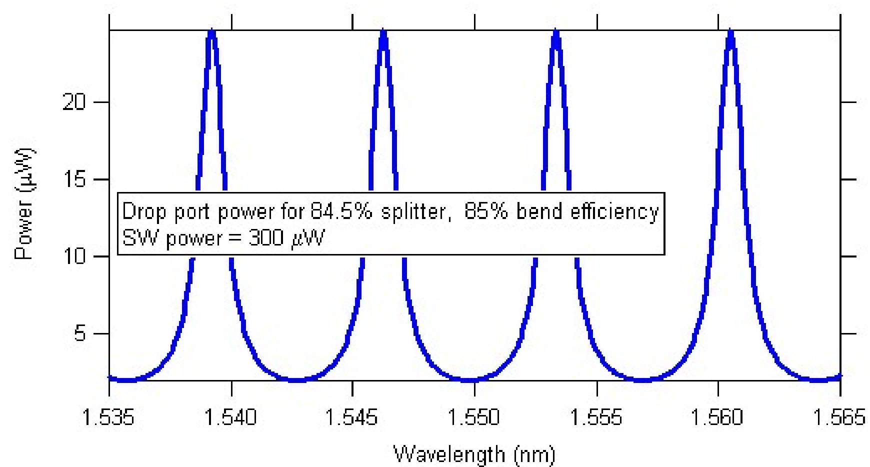

(b)

Figure 6.17 RR1 drop port power (a) measured (b) calculated

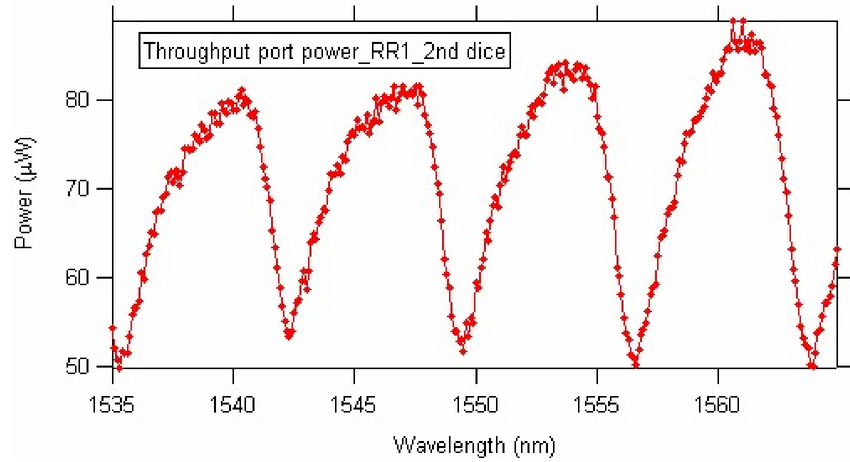

(a)

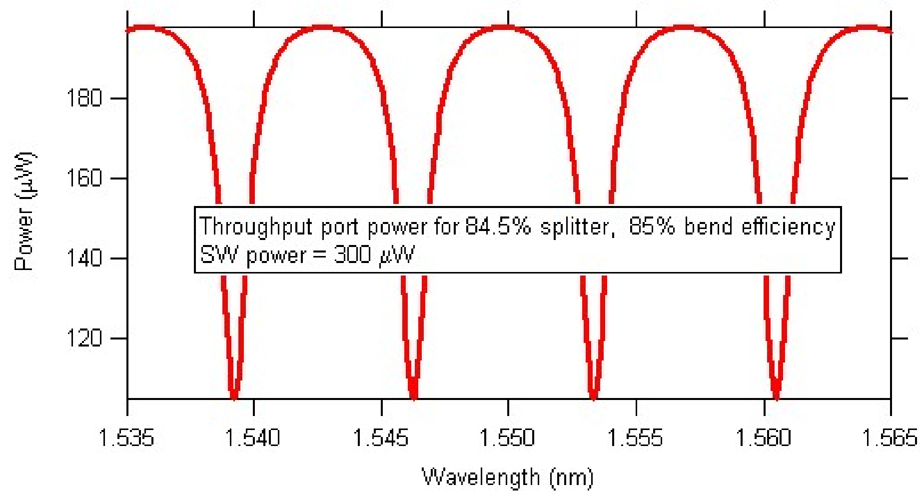

(b)

Figure 6.18 RR1 throughput port power (a) measured (b) calculated

This measured drop port power is in very close agreement with our calculation. The reason behind the shift in the peak of the drop wavelength is explained in Section 6.4.1. The device full width at half maximum (FWHM) is ~1.8 nm and the

Q factor is ~ 860. The insertion loss for the drop port is more than 10 dB. The measured throughput port power is lower than what is predicted by calculation. After microscope inspection, we found several particulates in the output waveguide responsible for lower power. However the extinction ratio, 2.5 dB, is in agreement with calculations.

The above analysis shows that our devices work in very close agreement to the analytical calculations. If we succeed in increasing the bend and splitter efficiency to 95%, the ring resonator will have a performance comparable or better than what is presented in the literature with considerable size advantage. Figure 6.19(a) and (b) and (c) show the analytical results for such a ring resonator. The insertion loss for drop port path is decreased to ~ 5dB while the FWHM is 0.75 nm and Q factor at 2066. The extinction ratio is over 7 dB.

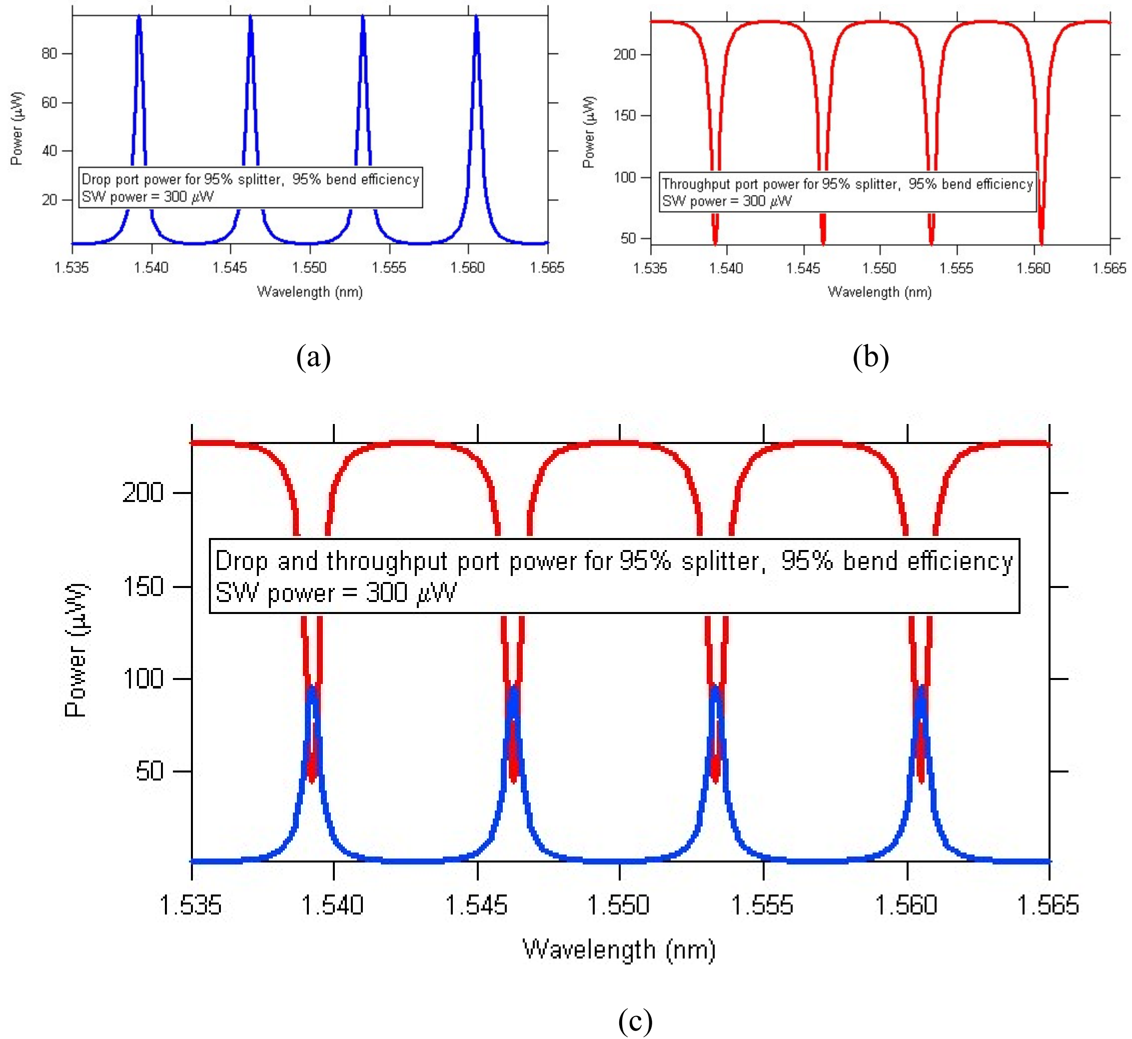

(a) (b)

(c)

Figure 6.19 calculated power for a 95% overall efficiency for splitters and bends (a) drop port (b) throughput port (c) both ports

6.5 Conclusion

We have demonstrated ultra compact ring resonators in PFCB polymers. We have compared the measured performance of the device to that of analytical calculations. The result shows that our devices behave as predicted while the amount of loss in drop and

throughput port is in agreement with our calculation considering the bend and splitter losses.

Future work will focus on the fabrication of ring resonators with improved bends and splitters. The improvements that we can readily make for the splitters are detailed in Section 5.4. We have been facing equipment issues in the lab which stopped further fabrication efforts

CHAPTER SEVEN

SUMMARY AND FUTURE WORK

The research presented in this dissertation is aimed at enabling higher integration of microphotonic devices for planar lightwave circuits. This is motivated by the need to reduce costs and size for practical applications. I have fabricated and characterized compact air-trench splitters that along with compact bends can dramatically reduce the size of PLC components such as ring resonators and Mach-Zehnder interferometers. I have demonstrated ultra compact ring resonators in PFCB. In this chapter I summarize the content of my dissertation and suggest areas for further development.

7.1 Summary

Planar lightwave circuits with higher integration, lower cost, and added functionality can reduce costs in optical network components. We chose Perfluorocyclobutyl polymers as a platform to demonstrate our ideas for compact devices in low index contrast (LIC) materials. The PFCB film characterization and waveguide propagation loss measurements were done prior to device fabrication and are detailed in Appendix A. In chapter 3 we presented the development of an anisotropic,

high aspect ratio ICP RIE etch for small features in PFCB on a silicon substrate. We observed an excessive lateral widening of features during the etch caused by stress in the PFCB film resulting from CTE mismatch with silicon substrate. We succeeded in etching deep (14 µm), and narrow (800 nm) highly vertical air trenches in an oxygen and carbon monoxide chemistry in ICP RIE in which extra carbon in CO promotes sidewall passivation. We suggested and incorporated stress relief trenches on either side of the main trench to be able to fabricate the desired width for the middle trench.

To avoid stress related problems caused by CTE mismatch between silicon substrate and PFCB film, we chose a new substrate with closer CTE to PFCB. In Chapter 4 we successfully demonstrated the PFCB small feature etch development on Ultem substrates.

In Chapter 5 we presented design, simulation and finally fabrication and measurement of air trench splitters in PFCB. Measurement results for a right angle splitter showed a 90.1 % efficiency (0.45 dB/splitter loss) with 86/14 splitting ratio which is in very close agreement with the 2-D FDTD simulation results.

We presented design, simulation, fabrication and characterization of ultra-compact ring resonators using the air trench splitters and bends in Chapter 6. We explained the measured performance of RR with comparison to analytically calculated performance with the same efficiency of building block splitters and bends. The ring resonator has a 70µm x 100µm footprint, a measured 7.2 nm FSR (as predicted), an 860 Q factor, and 1.8 nm FWHM. The performance degradation is a result of less than perfect bends and splitters.

7.2 Future Research

Future research is presented in a separate section for each main topic. Most of the further work presented below is readily doable and was not done mainly due to recent equipment problems in the clean room.

7.2.1 PFCB Small Feature Etch

The CO/O_2 ICP-RIE small feature etch developed in Chapter 3 has the desired aspect ratio and sidewall verticality required for an air trench splitter. However, the sidewall roughness could be one source for splitter losses. Experiments can be done for roughness reduction by possibly reducing CO in the mixture that results in less sidewall passivation and therefore possibly less roughness. The reduced passivation will also result in linewidth loss and verticality will be compromised. It is worth an effort, however, to investigate the etch parameters for a happy balance of less passivation for less roughness and conserved verticality.

Also more research can be done on the stress relief features by characterizing the widening as a function of the main etched feature's width and length as well as the distance from stress relief features.

7.2.2 Air Trench Splitters

A right angle air trench splitter with uneven splitting ratio was realized for use in ring resonators. We also have designed 50-50 splitters that have a 107.5^o angle. Splitter

devices were half way fabricated to measure efficiency and splitting ratio, but equipment issues interrupted the fabrication process. These devices can be fabricated with the exact same process as we used for 90 degree splitters. We do not have any reason to believe that these devices will have less efficiency or an unexpected splitting ratio compared to the 90 degree splitters.

On the other hand, we believe that air trench sidewall roughness is the main factor responsible for losses in the splitters. As suggested in Section 7.2.1 sidewall roughness reduction experiments can be conducted by changing etch parameters to slightly decrease sidewall passivation. Another possible path is to use the SF6/O2 etch developed in Chapter 3 to fabricate the splitters. This etch has smoother but thicker passivation sidewalls (100 nm or more). Even though the effect of the passivation on optical performance of the splitter is unknown, I believe it is a worthy subject to be investigated.

7.2.3 Ring Resonators and Mach-Zehnder Interferometers

The fabricated ring resonator presented in Chapter 6 is comprised of splitters and bends with an efficiency of approximately 85%. The next generation of fabricated splitters has a higher 90.1 efficiency, but fabrication of RR with those building blocks was put on hold because of lab equipment issues. The RR efficiency will be improved if it is realized with the already achieved higher splitter efficiency. The performance of such RR is shown in Chapter 6. Also if we succeed in increasing the splitter efficiency as suggested in Section 7.2.2, the FWHM will drop to 0.75 nm while the Q factor increases to 2066. The throughput port extinction ratio will be 7dB. This will bring us to a

performance comparable to what is reported in the literature while the size is reduced 1700 times compared to a conventional ring resonator in the same material system.

We also have designed MZIs using 50-50 splitters and 53.75^{o} bends. Once the performance of the 50-50 splitter is confirmed by measurement, the MZI devices can be fabricated. Symmetric and asymmetric MZI can be laid out on a mask to study the performance of the devices.

Once desirable RR and MZI performance is achieved, these devices can be activated by using electro-optic polymers or the thermoptic effect. RRs can be cascaded to achieve desirable band-pass filter characterization.

Appendix A

Initial PFCB Process Development and Characterization

In this appendix we present preliminary process development for PFCB polymers and follow with PFCB propagation loss measurement.

A.1 Introduction

To achieve our ultimate goal of fabricating various high efficiency Planar Lightwave Circuits (PLCs) in PFCB polymers, the first step is to achieve a high quality and uniform film of PFCB that has desired thickness and optical characteristics according to our device design. Optical integrated circuits of interest are waveguide devices in which light is carried in a rectangular core region surrounded by cladding material (channel waveguide). This requires two different formulations of PFCB for core and cladding layers. The refractive index contrast between the two layers is a deciding factor in the waveguide design and determines the minimum core size for single mode waveguide operation for a given wavelength. Then we need to have a precise process to achieve the desired film thickness based on our waveguide design. Section A.2 of this appendix focuses on film characterization including refractive index and film thickness measurement.

Another important factor in realizing PLCs is low waveguide propagation losses. We put together a measurement set up and discuss PFCB loss measurement using a racetrack method. We discuss the racetrack fabrication in Section A.3, while discussing the measurement set up and loss measurement results in Sections A.4 and A.5.

A.2 PFCB film Characterization

The waveguide design dictates under-clad, over-clad and the core film thickness. The PFCB film is made by spin casting liquid polymer on a silicon substrate. This film then needs to be cured in an inert nitrogen atmosphere until fully cross-linked. The following processes need to be optimized:

- A spinning process to cast a uniform film, fully covering the substrate surface.
- A curing process to fully cross-link the polymer to stabilize the refractive index.
- Fully characterize the film by
    - Measuring the refractive indices of the core and clad at device operation wavelengths for TE and TM polarized light
    - Making a spin curve for both core and cladding to achieve desired film thickness for each layer

In this section, we describe the process development effort to achieve a high quality PFCB core and clad film and the subsequent optical characterization of the film.

A.2.1 Initial PFCB Process Development

The first step in starting a fabrication process in a PFCB polymer was to achieve a uniform and transparent film on silicon through spin casting. The first iteration of the PFCB solution, supplied to us by Tetramer Tech. L.L.C., was a combination of BPVE/TVE copolymers. This solution turned cloudy after a few weeks of storage and after being spun and cured at 220°C on top of silicon, it did not form a film, but did form a few large drops as seen in Figure A.1(a). Our chemist colleagues at Tetramer Inc. suggested that solution cloudiness could be due to small amounts of a crystallized BPVE polymer component, which has a rigid molecular configuration and/or extra cross-linked (thus less soluble) material. The formation of large drops could be due to the fact that the less soluble/higher cross-linked material became insoluble before the rest of the material on evaporation of the solvent. To solubilize the higher cross-linked (higher molecular weight) portions, we heated the polymer while purging nitrogen in it to avoid any reaction with oxygen. This made the solution more homogeneous and reduced the problem but did not completely solve it (Figure A.1(b)). The next batch we received resulted in much better films, but there was some shrinking at the edges of the substrate after curing (Figure A.1(c)). This problem was later solved by increasing the molecular weight during the preparation of the polymer which makes a stronger film. Also the solvent percentage was reduced, giving a higher weight percentage of polymer (more viscous).

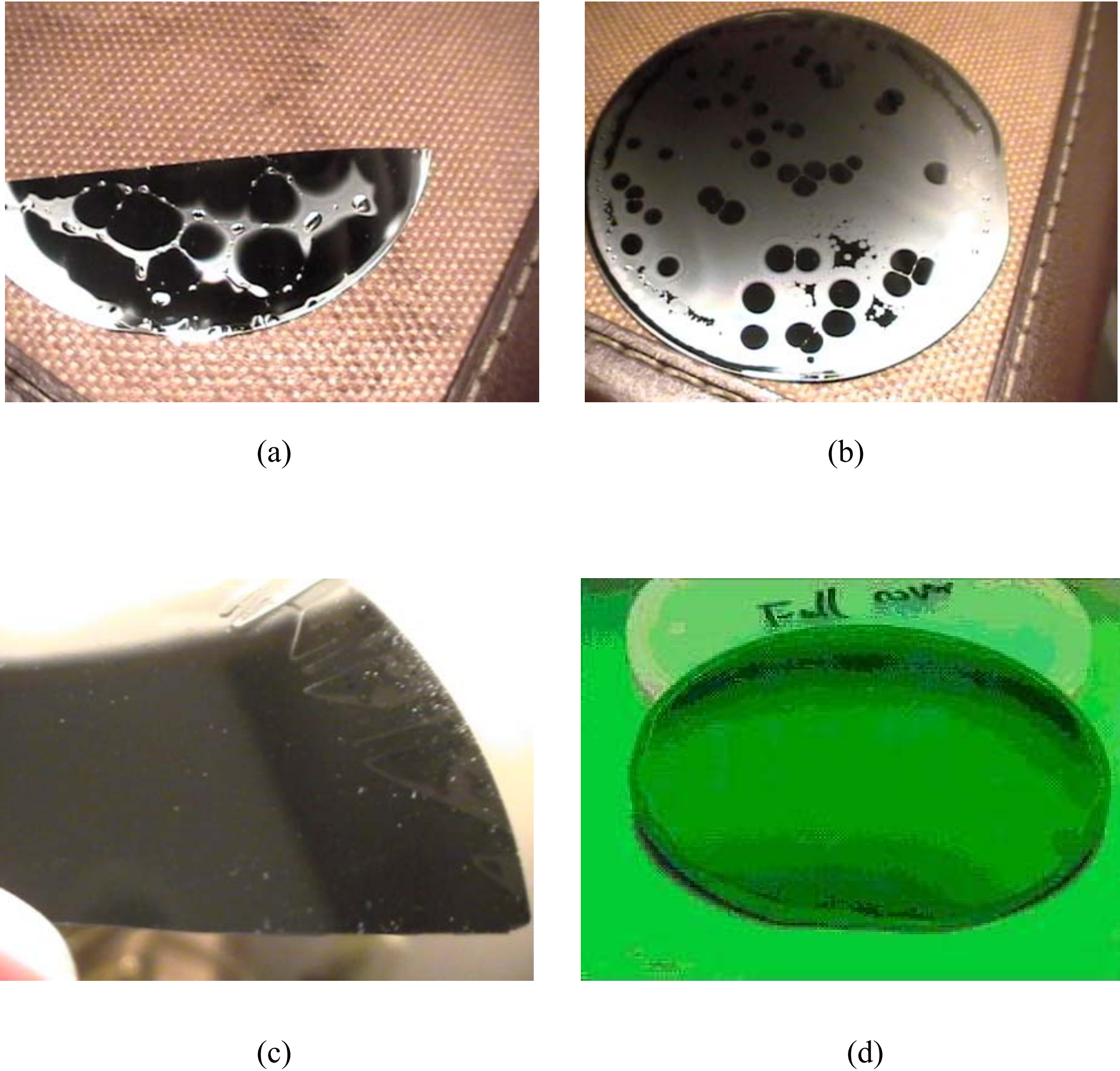

Figure A.1 progress of film quality (a) the first batch of PFCB (cloudy solution) (b) after solution was heated and stirred (c) new batch with some shrinking at the edges (d) higher molecular weight solution solving the shrinking problem

A.2.2 Optical Characterization

After successfully forming PFCB films on silicon substrates, the films were fully characterized to determine refractive indices for TE and TM light at a 1550 nm wavelength. Next the proper spin and cure process was determined to achieve the core and cladding thickness according to our waveguide design. Both refractive index and film thickness were measured using a prism coupler. Table A.1 shows measured refractive

indices of film cured at 220-230°C. All the presented studies were done on the first working batch of the PFCB we received in 2003. Thickness and refractive index characterization was repeated on every new supply of PFCB.

Table A.1 Refractive index measurement experiments for core and clad at 1550 nm wavelength (both TE and TM polarization)

S1 Measured at Tetramer, TE polarization, 2 hrs	1.478	1.464	0.95%
S1 Measured at NMDL, TE polarization, 2 hrs at 220o C	1.4785	1.4638	0.99%
S1 Measured at NMDL, TM polarization, 2 hrs at 220o C	1.4762	1.462	0.96%
S1 Dual film, Measured at NMDL, TE polarization, 2 hrs at 220o C	1.4791	1.464	1.02%
S1 Dual film, Measured at NMDL, TM polarization, 2 hrs at 220o C			
S2 (New PFCB) Measured at NMDL,TE, 2 hrs at 190 & 2 hrs at 230	1.481	1.466	1.01%
S2 (New PFCB) Measured at NMDL,TM, 2 hrs at 190 & 2 hrs at 230	1.479	1.4646	0.97%
S2 (Old PFCB) Measured at NMDL, TE, 2 hrs at 190 & 2 hrs at 230	1.481	1.4675	0.91%
S2 (Old PFCB) Measured at NMDL, TM, 2 hrs at 190 & 2 hrs at 230	1.479	1.4678	0.76%
S2 (Old PFCB) Measured at NMDL, TE, 2 hrs at 190 & 2 hrs at 230, on Kapton		1.4737	
S3 (New),Measured at NMDL,TE, 2 hrs at 225	1.48	1.4668	0.89%
S3 (New),Measured at NMDL,TM, 2 hrs at 225			
S3 (Old),Measured at NMDL,TE, 2 hrs at 225	1.48	1.4695	0.71%
S3 (Old),Measured at NMDL,TM, 2 hrs at 225			
S3 (New),Measured at NMDL,TE, 2.5 more hrs at 225 (4.5 hrs total)	1.4786	1.465	0.92%
S3 (New),Measured at NMDL,TM, 2.5 more hrs at 225 (4.5 hrs total)	1.4768	1.4628	0.95%
S3 (Old),Measured at NMDL,TE, 2.5 more hrs at 225 (4.5 hrs total)	1.4785	1.467	0.78%
S3 (Old),Measured at NMDL,TM, 2.5 more hrs at 225 (4.5 hrs total)	1.4763	1.4649	0.77%
S3 (New),Measured at NMDL,TE, 4 more hrs at 225 (8.5 hrs total)	1.478	1.464	0.95%
S3 (New),Measured at NMDL,TM, 4 more hrs at 225 (8.5 hrs total)	1.4762	1.4625	0.93%
S3 (Old),Measured at NMDL,TE, 4 more hrs at 225 (8.5 hrs total)	1.4778	1.4657	0.82%
S3 (Old),Measured at NMDL,TM, 4 more hrs at 225 (8.5 hrs total)	1.4761	1.464	0.82%
S4 (New),Measured at NMDC, TE, 4 hrs	1.4789		
S3,4 (New),Measured at NMDC, Dual film,TE,Clad 8.5 hrs & core 4 hrs	1.4789	1.464	1.01%
S3,4 (New),Measured at NMDC, Dual film,TE,Clad 8.5 hrs & core 4 hrs	1.4763	1.4626	0.93%
S3 (New),Measured at NMDL,TE, 17 more hrs at 225	1.4774	1.4636	0.93%
S3 (New),Measured at NMDL,TM, 17 more hrs at 225	1.475	1.4613	0.93%
S3 (Old),Measured at NMDL,TE, 17 more hrs at 225	1.4771	1.4649	0.83%
S3 (Old),Measured at NMDL,TM, 17 more hrs at 225	1.4745	1.4625	0.81%

For a $\Delta n = 0.95$, we found a 4 μm x 4 μm core insures single mode propagation. We found that spinning the core solution at 1800 rpm gives us a 4 μm thick film. We also found through simulation that 99.99 % of the mode is contained in a 7 μm radius around the center of the mode (core center). For the mode not to interact with air or the substrate, we needed thick enough cladding layers. For a 10 μm undercladding layer, we spun the solution at 2000 rpm, and for overcladding, we spun the clad at 1800 to achieve a 12 μm thick film to make up for the thickness that goes to planarizing the film after over 4 μm of waveguide etch. The refractive index and thickness measurements were redone after receiving every new batch of PFCB.

A.3 PFCB Loss Measurement Device Fabrication

A very important factor that makes a material system attractive as a platform for planar light wave circuits is low propagation losses. As discussed in the background section, PFCB material is partially fluorinated to reduce propagation losses in the communication wavelength window. Theoretical calculations predict losses lower than 0.1 dB/cm [11]. This section contains the propagation loss measurement effort for PFCB waveguides. In the first sub-section we examine our choices for loss measurement methods and explain the fabrication of racetrack waveguides, our preferred loss measurement approach. A measurement set up is then assembled and calibrated for various errors to insure reliable measurement data and then the propagation loss is measured and reported.

A.3.1 Propagation Loss Measurement Method

We examined our options to choose the best loss measurement method. One widely used approach is the “cut-back method” in which the output power is measured on the same waveguide while in each iteration the waveguide is cut back in length. The problems with using this approach for PFCBs are as follows:

1. Dicing PFCB is a low yield process as PFCB to silicon adhesion was not good at this point. Multiple dices increased the failure rate.
2. It is not easy to measure losses as low as 0.1 dB/cm. This is because the power change resulted from cutback steps of tens of millimeters are very small and fall into the detector noise range.
3. The exact same input fiber to waveguide coupling in consecutive measurements becomes very important. This is because we are seeking to measure very small changes in power and slightly different in-coupling can cause changes that mask the actual change we are trying to observe.

Another loss measurement approach is to fabricate two sets of waveguides, one of which is considerably longer than the other, so the power difference is easily observable even for a low loss waveguide. In the fabrication of straight waveguides, we are limited to the length of the wafer (3” in our case); therefore, we use a racetrack waveguide that curves several times to make a longer waveguide. The bend radius for our PFCB waveguide was calculated using BeamPROP to be 1.06 cm for a 0.005 dB turn loss. This

loss is much smaller than the expected 0.1 dB/cm propagation loss and therefore will not affect the loss measurement accuracy.

An optical mask was designed containing 9 racetrack and 18 straight waveguides. The die size is 5.57x 4 cm^2 and the racetrack length is 56.7 cm versus the 5.5 cm straight waveguide. To achieve an accurate loss measurement, we need a very high quality PFCB film in the die region, free of particulates. As the racetrack waveguide travels across a large area of the die, the probability of crossing a path with a film imperfection increases. This makes fabrication of a racetrack waveguide a high low process.

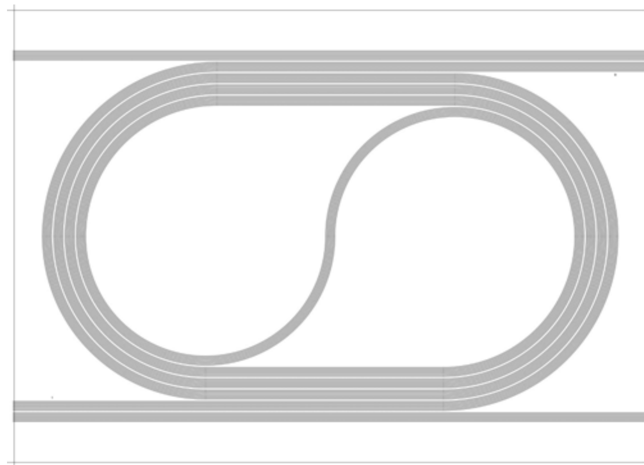

Figure A.2 Racetrack pattern: includes 9 straight waveguides in the input side, 9 in the output side and 9 racetracks in the middle

A.3.2 Racetrack Waveguide Fabrication

PFCB Racetrack waveguides were fabricated and tested. In this section the fabrication process and the main problems encountered during the process are presented as well as solutions to some of the problems.

The material used for making the racetrack was the PFCB solution received from Tertramer Tech. in Feb. 2004. Both clad and core were composed of copolymers 6F:TVE with ratio of 50:50 for the clad and 15:85 for the core. The refractive index difference between core and clad measured at Tetramer was Δn=0.95%. Since the racetrack design was highly sensitive to Δn, a close characterization of core and clad was needed. These refractive index characterizations were redone every time we received a new supply of PFCB. Core and clad samples were made and refractive indices of the films were measured using a prism coupler. The measured values were n_{core}=1.4780 and n_{clad}=1.4681 for TM polarization, resulting in a Δn = 0.68 %. A series of experiments was done to find the reason why Δn was so different and then attempt to solve the problem was performed.

Table A.2 Curing experiments to fix Δn at about 1 %

	n_{Core}	n_{Clad}	Δn
S1 measured at ~225 C, Tetramer (2 hrs)	1.4785	1.4671	0.77%
S1 measured at ~225 C, NMDL (over night)	1.4778	1.4644	0.90%
S1 measured at ~225 C, Tetramer (over night)	1.4784	1.4611	1.17%
S2 made at ~225 C (2 hrs)	1.4793	1.4689	0.70%
S2 made at ~225 C(over night)	1.4775	1.4657	0.80%
S1 Re-measured in 3 days	1.4784	1.4642	0.96%
S2 Re-measured in 3 days	1.4776	1.4658	0.80%
S3 made at ~220 C (2 hrs)	1.4783	1.4703	0.54%
S3 made at ~220 C measured right after cure (over night)	1.47745	1.465	0.84%
S3 Core on Clad (over night)	1.4763	1.465	0.76%
S3 made at ~220 C measured after 7 hrs (over night)	1.4779	1.4651	0.866%
S3 cured over night for the second time (Over clad on top of the core and clad)	?	1.4651	?
S3 cured over night for the second time (separate core and clad samples)	1.4777	1.4644	0.867%
S4 cured for 2 hrs		1.46945	
S4 cured over night (separate core and clad witness samples) / TE	1.48046	1.4656	1.00%
S4 cured over night (separate core and clad witness samples) / TM	1.478	1.4638	0.96%
S4 cured over night for the second time / TE	1.4804	1.4655	1.00%
Over clad (over night)		1.4656	
S4 cured over night for the second time / TM	1.4784	1.4633	1.00%

Table A.2 summarizes refractive index experiment results. To help read the table, notice that S1 refers to the samples made at Tetramer while S2-S4 to the ones made at NMDC labs. All refractive indices measured at NMDC are an average of 5 or more measurements and to assure the curing temperature at NMDC and Tetramer was the same, a thermocouple was sent to Tetramer to calibrate with their thermometer.

In several iterations, after changing the cure time from 2 hrs to an over night bake (~17 hrs) and dropping the temperature by 5° C (from 225°C to 220°C), a fixed Δn=1% was achieved.

The fabrication process to make the racetracks is schematically shown in Figure A.3. Each fabrication step requires attention to many critical details in order to have a final product appropriate for measurement.

To filter the clad and core polymer, a filtering tower was used with a 0.2 μm PTFE filter. The glass syringe and the vials were cleaned with acetone, methanol and iso-proponol and dehydrated in a class 100 cleanroom oven at 90° C for 30 minutes. **A** PFCB adhesion promoter was filtered with 0.2 μm PTFE and dispensed to cover the whole wafer surface with spin and bake parameters at pre-spin: 500 rpm/100 ramp/5 sec (to spread the polymer on the substrate at a low speed), spin: 3000/500/60 and bake for 4 minutes at 100° C on the hotplate. 2.5-3 grams of filtered cladding was dispensed in the middle of the wafer and every bubble or particulate was removed using a glass pipette. With the early supplies of PFCB such as the one used in this stage, every unremoved bubble or particulate resulted in a de-wetted region after curing if not removed. The cladding was spun at 500/100/5-2000/500/60 to get a ~12 μm thick film. The wafer was placed on an aluminum foil sheet, covered with a pyrex dish and placed in the oven to cure in a nitrogen atmosphere at 220°C for 17 hours. The oven must be cooled to under 100°C before taking out the sample. The core layer was then spun on top of clad film at 500/100/5- 1400/500/60 to achieve a 4 μm thick film. The baking process is the same as above and all the same precautions need to be taken.

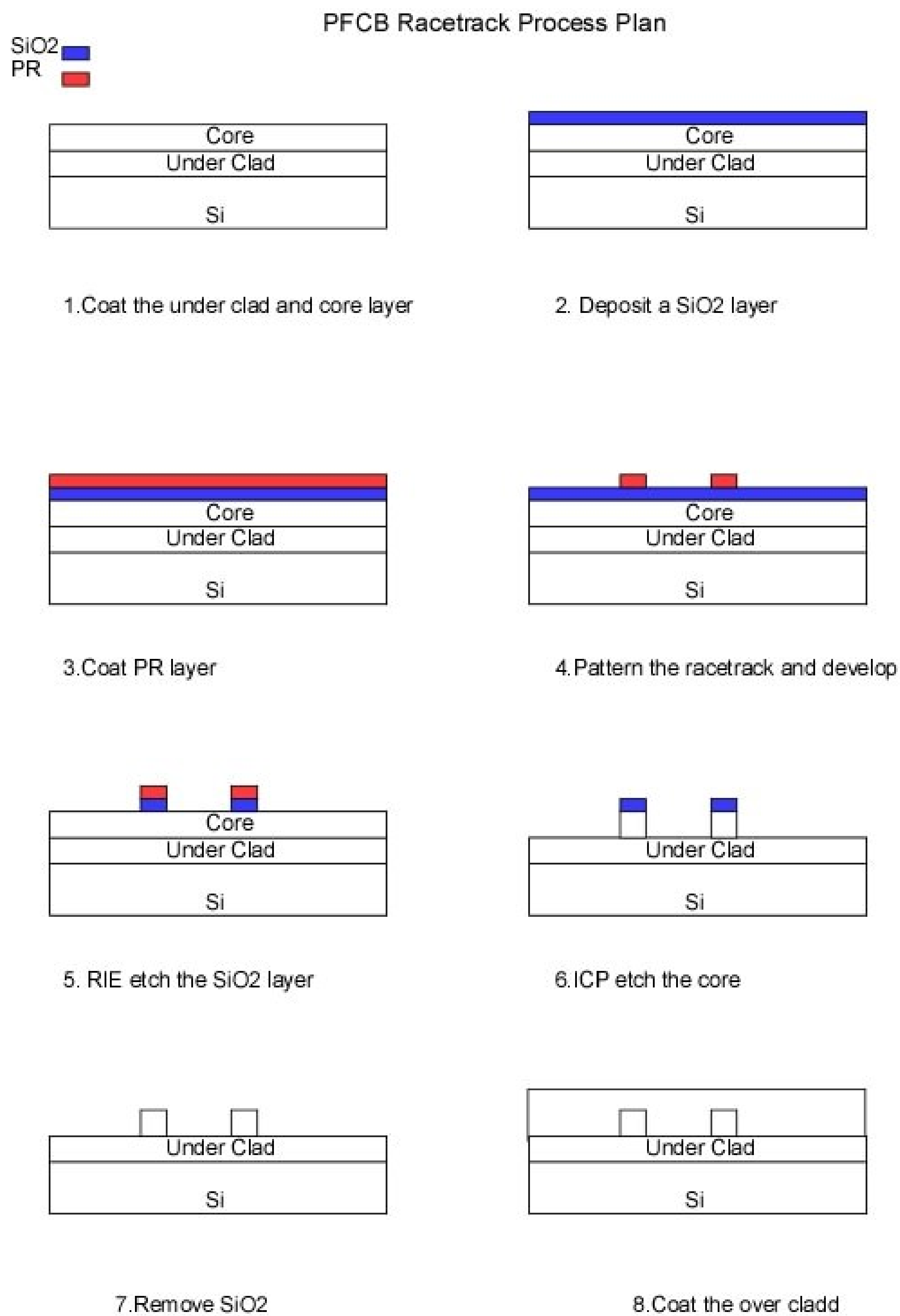

Figure A.3 PFCB racetrack fabrication process plan

The waveguide is patterned and then etched in the core layer using a Plasmatherm System 790 reactive ion etcher (RIE). The etch mask used for waveguide fabrication is a 150 nm thick film of RF sputtered SiO_2. A positive photoresist, AZ-MiR, was spun and baked. The photoresist film is then exposed with the racetrack mask, using the mask aligner. It is then developed in AZ 300 developer and rinsed with de-ionized water. A recipe for pulsed etching of small features was used to etch SiO_2 in the conventional RIE. This process floods the chamber with O_2 and He after a period of etch with O_2 and CHF_3. The flooding reduces the charges that build up during etching. A PFCB core was etched in a helium and oxygen chemistry. Figure A.4 shows the etched core profile with vertical sidewalls. The excess SiO_2 was then stripped in fresh buffered hydrofluoric acid solution (BOE). The last step was to cast the overcladding at 500/100/5-3000/500/60 to get a ~9 μm thick film cured at 220°C. Figure A.5 shows the fabricated racetrack. The sample was then diced into a 5.5 cm x 5.5 cm square to expose the input and output of the waveguides for fiber coupling.

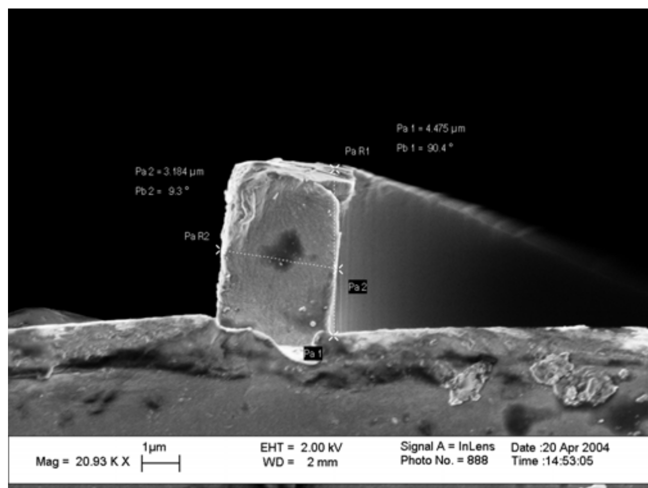

(a)

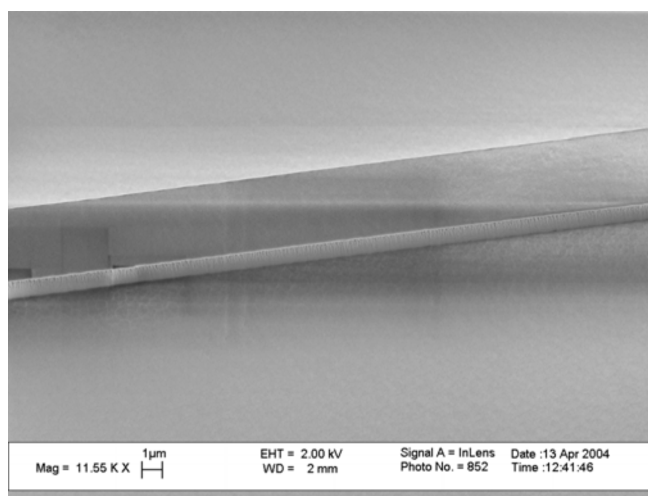

(b)

Figure A.4 PFCB core after PFCB etch (a) cross section (b) top view

Figure A.5 Fabricated PFCB racetrack on silicon substrate

During the full fabrication process, we encountered several complications. Some of the major complications along with the solutions we found to avoid them are presented to help a deeper understanding of the process development:

1. PFCB film creased and delaminated during the photoresist developing process in 50% of the samples. The problem always started from the middle of the film as shown in Figure A.6. We approached this problem with a guess as to its origin. There is a built in stress in the PFCB film as a result of its CTE mismatch with silicon substrate. This makes the film vulnerable to abrupt temperature change. The first thing we tried in terms of avoiding harsh temperature changes was waiting for the sample to reach room temperature after the curing process. Previously we took the sample out of the oven after it reached 100°C or less, as Tetramer suggested. After making this change, over 80% of the samples survived the developing step. Later, as we progressed to more complicated device fabrication processes, we lowered the curing temperature to 190°C for slower

cross-linking that resulted in less film stress. This lengthened the cure process considerably for refractive index stabilization and required a new full refractive index characterization.

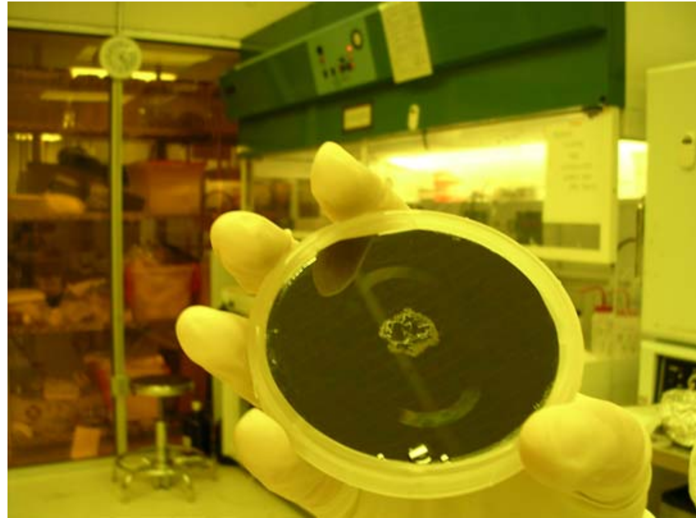

Figure A.6 PFCB delamination during developing

2. The original SiO_2 etch recipe in the RIE resulted in slanted SiO_2 sidewalls after etch as shown in Figure A.7(a). This could compromise the PFCB waveguide etch in terms of sidewall angle and feature size. This problem was likely caused by charge accumulating on the surface during a long SiO_2 etch. The problem was solved by breaking up the etch in shorter durations and purging the chamber in between etch steps. The improved results are shown in Figure A.7(b).

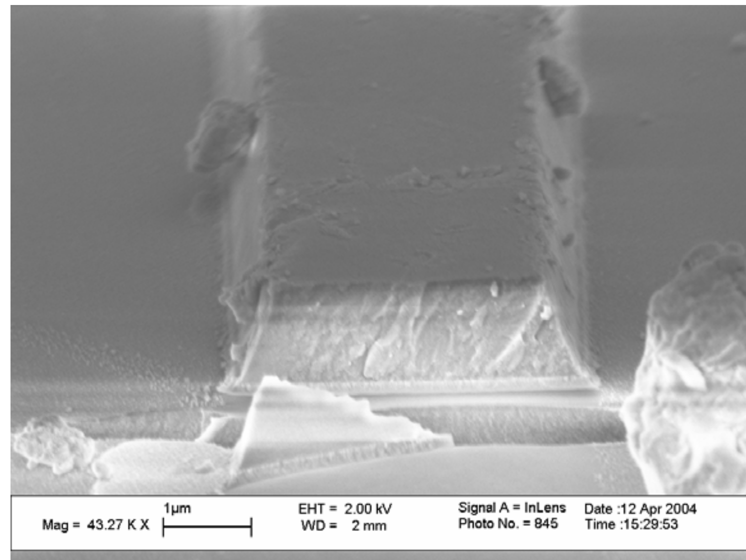

(a)

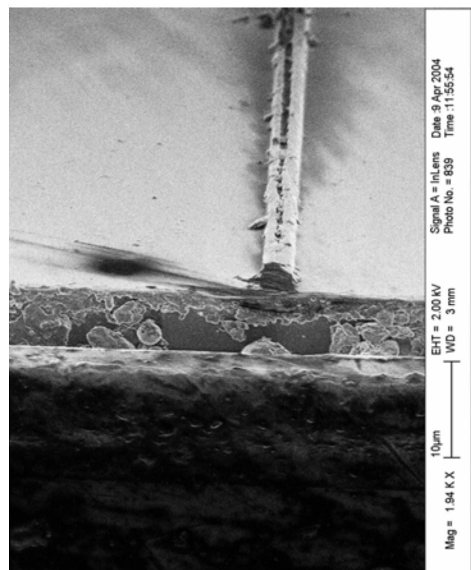

(b)

Figure A.7 SEM images of (a) SiO2 etched profile before pulsed etch was used (b) tilted top image etch profile after changing to etch to pulsed

3. The PFCB film delaminated from silicon during dicing. This delamination was sometimes so severe that the whole film peeled off the substrate and sometimes only at the edges which made in and out coupling difficult. We reported this

problem to our chemist colleagues at Tetramer. They worked to improve the adhesion promoter which had a great effect on adhesion.

Before measurement, we did a thorough optical microscope inspection of all waveguides to find the ones with the least number of defects. Also we made a defect map for each racetrack and straight waveguide to later match with top-view infrared images of light traveling in the waveguide. This will help us determine which kind of defects cause a lot of loss. Figure A.8(a)-(d) show general types of waveguide problems.

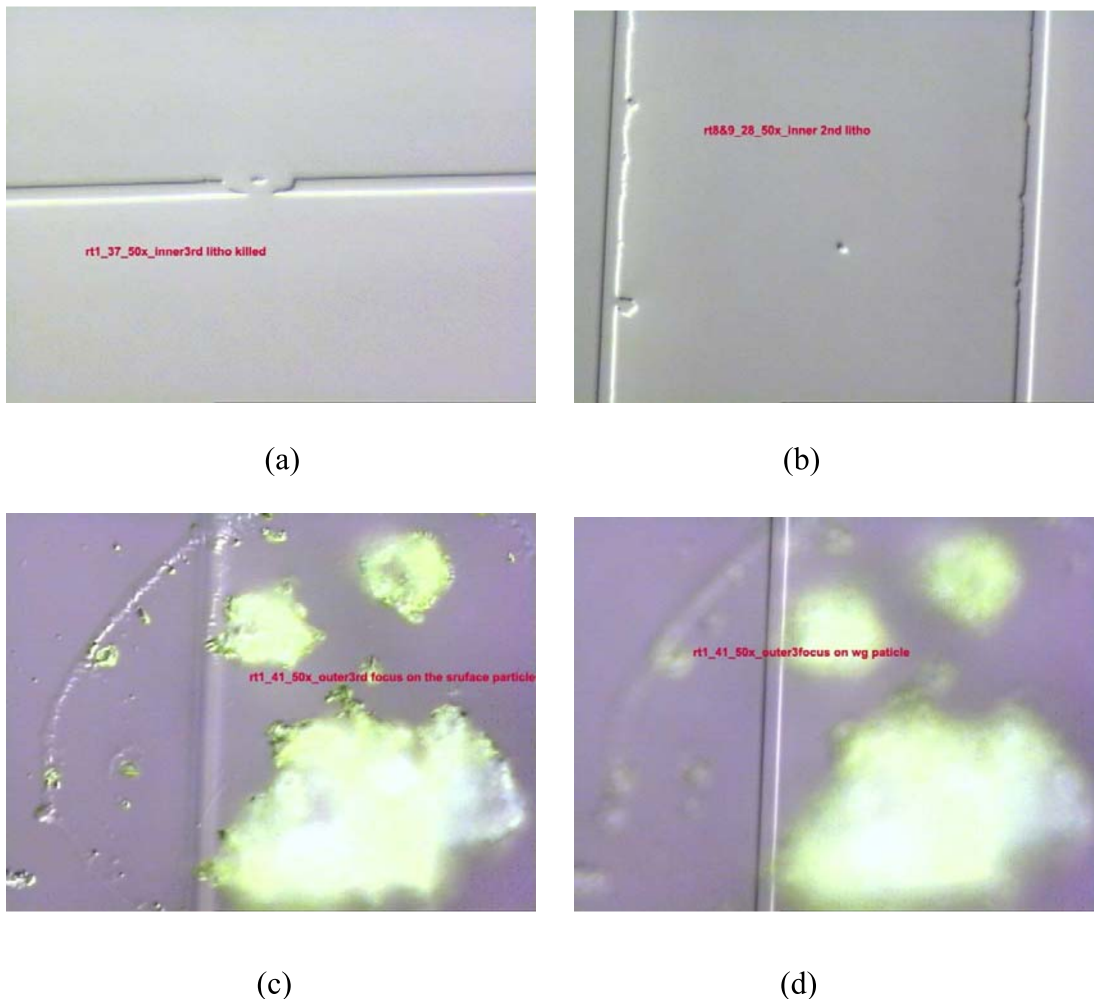

Figure A.8 Examples of different defects observed on the race track waveguides (a) broken waveguide, lithography problem (b) jagged edges and deformation, lithography problem (c) particle on the cladding with focus on particle (d) same as c with focus on waveguide

A.4 Measurement Set up

To measure the loss propagation using fabricated racetrack waveguides, we put together a measurement setup as seen in Figure A.9. We used two Elliot XYZ flexure stages with the added pitch and yaw module to align the input and output fiber to the waveguide. There is an 8 mm traveling range per axis. Light was butt coupled into the waveguide from a HP-8164A semiconductor laser source with polarization maintaining (PM) single mode fiber for polarization specific loss measurement. Initially, the rough fiber to waveguide alignment was done manually with moving the flexure stages and monitoring x alignment and z separation using a XTS series zoom stereo microscope. The waveguide output mode was imaged using an Alpha NIR camera and maximized by centering the fiber core and waveguide. After manual adjustments, output power was coupled into a single mode waveguide and measured with a HP detector. This measured power was normalized to the input power monitored by splitting the input power and feeding one branch of the fiber to a Thorlab detector via an FC connector. Thorlabs 3-axis piezo controller model MDT693 with 25 μm traveling range was used for the automated part of the alignment. Two National Instruments BNC-2110 data acquisition boards were used to facilitate communication between the automation program and the stages. The auto-align program was written using a NIDAQ, an Igor software (Wavemetrics, Inc.) tool and used a conical scan method to maximize the output power.

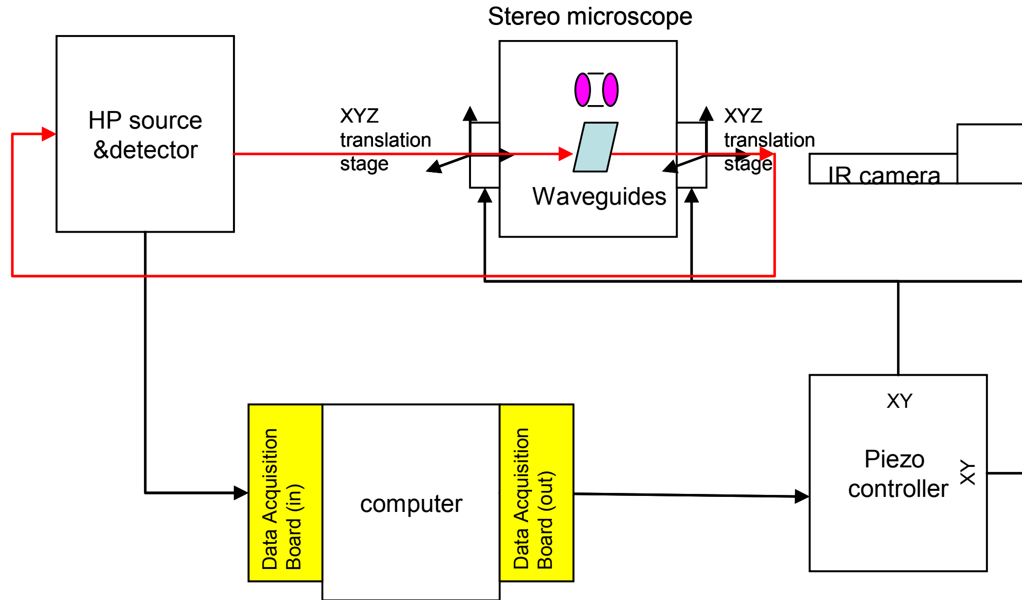

Figure A.9 Measurement set up schematic

We first calibrated the system for the variations introduced to waveguide output power by different changes in the measurement set up. We noticed unplugging and plugging of the fiber from the power monitor detector changes the waveguide output power. At first the bare end of fiber was sticking out of the connector. We maximized the monitor detector power, set the separation between the waveguide and fiber and scanned the output 25 times recording the power reading. The power monitor fiber was then disconnected and reconnected and the same test was done 5 times. We measured a 0.14% standard deviation for monitored power and 0.6% for waveguide output power. Next we improved the power variations by leveling the fiber end at the connector. The standard deviation of both measured powers was reduced to ~ 0.06 %. This showed that if the fiber is flush at the connector end, there are no serious power variations as a result of unplugging and plugging of the power monitor fiber.

Since the z separation between fiber and waveguide can only be set manually by visual methods, we looked into measurement variability as we tried to set the fiber at the same distance. It is very important for us to be able to repeatably set the z separation to the same point because if we are not able to couple the same amount of light into different waveguides, the change in the output is not just dependant on propagation loss. The input and output fibers were brought in manually to slightly touch the waveguide as a position reference and then moved back 8 μm using the piezo controllers. The maximum power was found and measured 25 times and averaged. The fibers were withdrawn and the same process was repeated 5 times and a standard deviation of 0.7% was measured.

Finally the Thorlab detector was tested for effects from the environment (piezo drive, light, vacuum pump). The results indicated that the environment did introduce variations to the noise level. As we reduced the integration time on the detector, more unwanted fluctuations were picked up. Averaging the detector input over a longer time has the benefit of smoothing these changes. The integration time was decreased and more fluctuations were observed on the noise level. A 20 ms integration time proved to be a good choice to reduce fluctuations.

A.5 Loss Measurement

The input light was set to the TE polarized (electric field in the plane of the substrate). This was done by maximizing the polarization maintaining (PM) fiber mode detected by the infrared camera passing through a polarizer set to a zero angle. The set up

is shown in Figure A.10. Light was then coupled into the racetrack with the fewest number of defects and the output mode was found using the IR camera as shown in Figure A.11. The output power was then measured by manually maximizing the light coupled to a single mode fiber connected to an HP detector. The power was then maximized. Power through a straight waveguide was also measured.

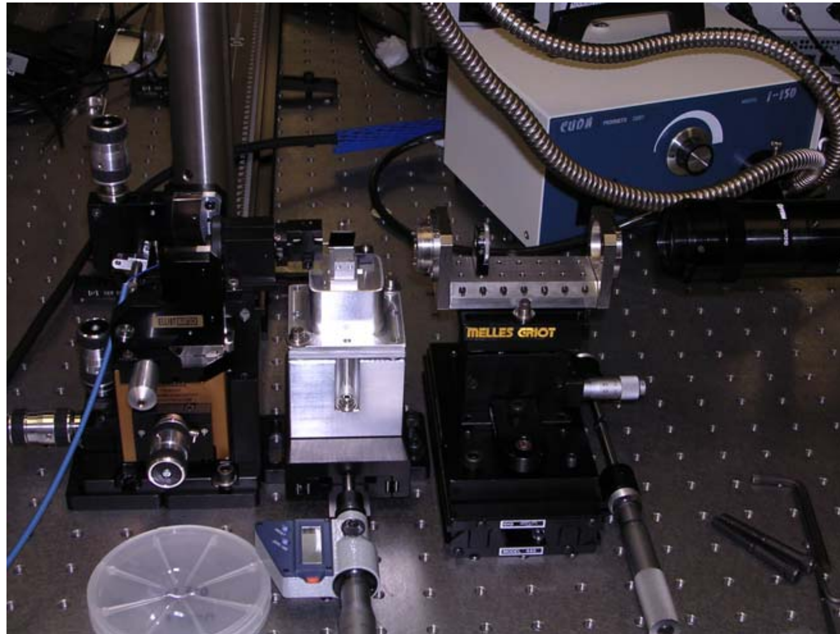

Figure A.10 Set up for input polarization adjustment

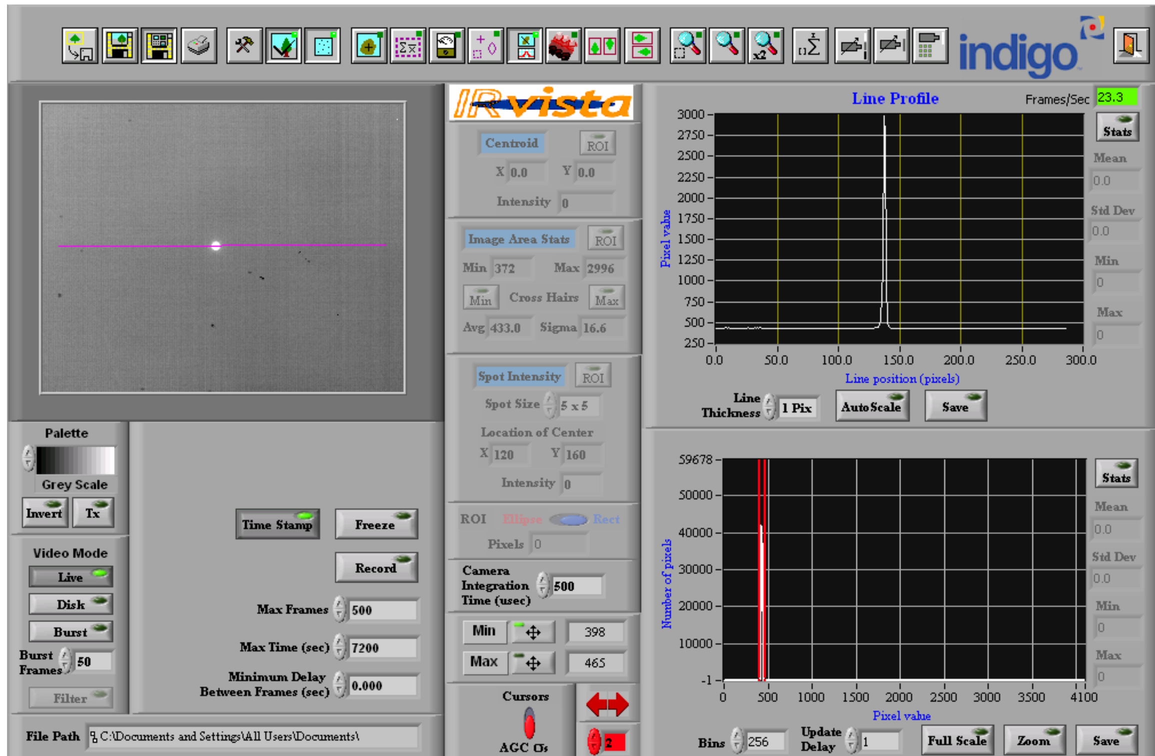

Figure A.11 Racetrack output mode detected by IR camera

An upper bound to PFCB propagation loss was determined as follows:

$$loss(dB/cm)=(loss_{racetrack}-loss_{straight\ wg})/(length_{racetrack}-length_{straight\ wg}) =$$

$$10*\log(P_r/P_s)/(56.27-5.56)= 0.394\ dB/cm,$$

where P_s and P_r are the powers from straight and racetrack waveguides. We believe this number represents an upper bound for PFCB waveguide propagation loss since there are other means of loss such as defects in the racetrack. Figure A.12(a) shows an infrared top image of the light traveling in the racetrack. There are clear spots of light escaping the waveguide. After comparing this image with the defect map, we found the defects

responsible for this extra loss. Figure A.12(b)-(d) show the defects that seem to have caused the bright spots in the IR image.

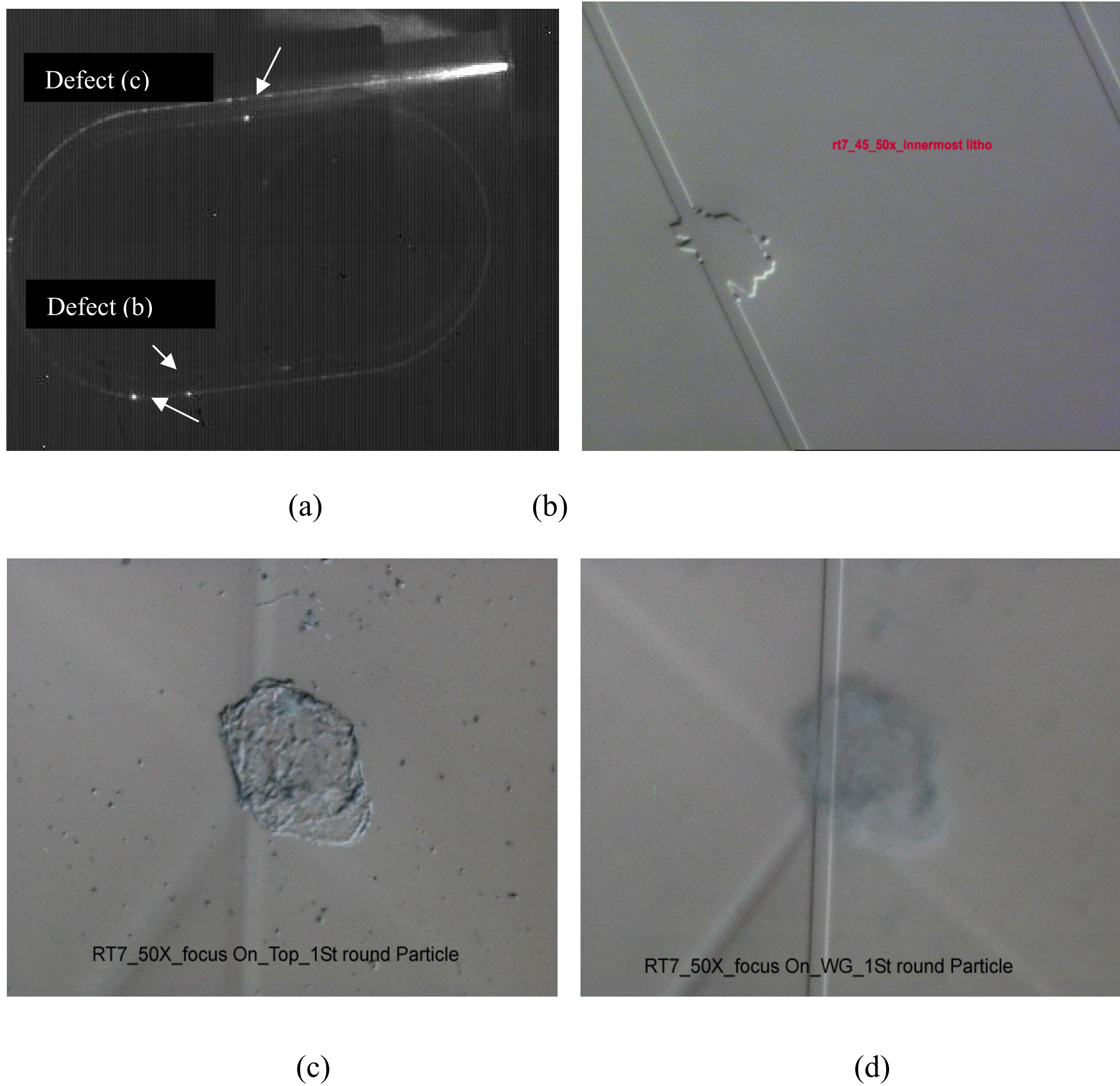

Figure A.12 Measured racetrack IR top images and some defects causing them (a) IR top image of racetrack (b) lithography problem (c) particle on over cladding with focus on surface (d) particle on over cladding with focus on the waveguide

Figure A.13 is taken of a different racetrack and is a more dramatic demonstration of the defect map matching the IR top image bright spots.

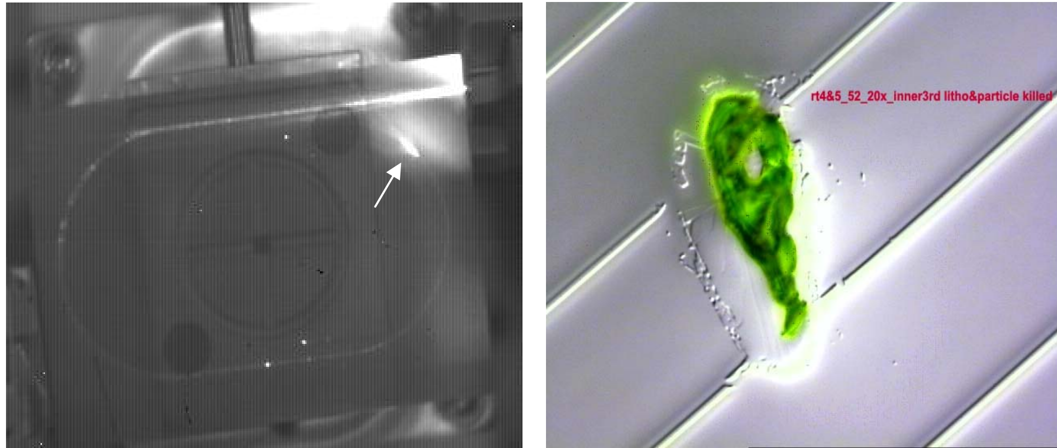

Figure A.13 Racetrack 4 IR top image and the defect causing big spray of light(a) IR top image of racetrack (a) broken waveguide causing the big splash of light

As indicated on Figure A.12(a), a particle on top of the cladding shown in A.12(c) and (d) seems to have caused the scattering which was not initially expected. We found out the reason why a surface damage caused losses using index matching fluid (IMF). Index matching fluid was used in the fiber/waveguide coupling points in both input and output sides to maximize coupling efficiency. It was observed that application of IMF resulted in about a 60% drop in the output power instead of an increase. A drop of oil was placed in the middle of the waveguide. Figure A.14 shows IR top images with and without IMF on top of the waveguide. This experiment showed that index matching fluid was coupling a fair amount of light out of the waveguide. This observation showed that our device cladding was not thick enough to completely contain the waveguide mode and the mode tail was beyond the over cladding. Since the refractive index of the IMF was greater than the cladding, light could couple into it and scatter. This adds another reason why the measured loss is only an upper bound.

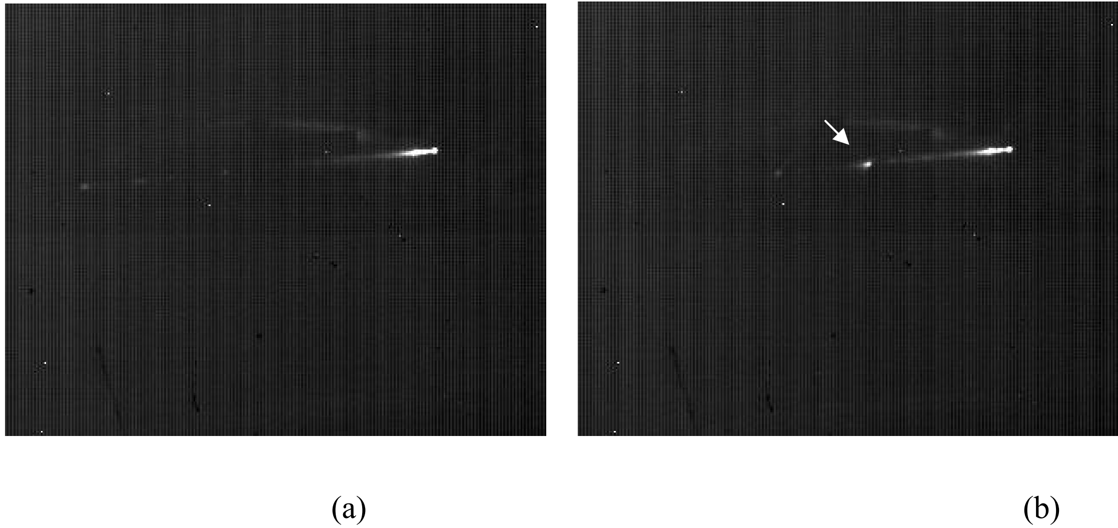

(a) (b)

Figure A.14 IR top image of straight waveguide (a) no IMF on top (b) a drop of IMF on waveguide coupling out light

A.6 Conclusion

In this chapter we have presented the initial PFCB process development as well as the PFCB propagation loss measurement. After achieving a high quality PFCB film, we set up and calibrated a measurement system to measure loss. A racetrack waveguide device was fabricated and an upper value of 0.39 dB/cm propagation loss was measured. In a later effort, the PFCB propagation loss was measured by the cut-back method using a Newport auto-align system in which we have a highly controllable waveguide to fiber alignment. The measurements using this method also resulted in a 0.4 dB/cm loss.

Appendix B

PFCB Air-trench Waveguide Splitter Fabrication Process Schematic

1- Spin and cure under-clad and core films on silicon substrate

2- Pattern patches with “PROTECT” mask

3- Deposit 5 nm/20 nm, Cr/Au film

4- Lift off to leave Au islands where EBL AM will be patterened

5- Deposit 150 nm SiO2 hard mask and spin AZMiR 701 positive PR

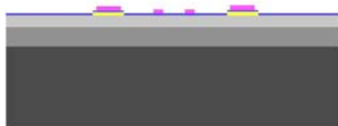

6- Pattern with “WAVEGUIDE” mask to layout waveguides and EBL AM on Au patches

7- Etch SiO2 in the ICP-RIE

8- Etch PFCB core in ICP-RIE

9- Remove excess SiO2 in BOE and spin and cure pver-cladding layer

10- Evaporate 100 nm Al etch mask, spin pos. PR and pattern with "OPENING" mask

11- Wet etch Al and etch the opening in the ICP-RIE to reveal the EBL AMs

12- Sputter 90 nm Al to increase etch mask thickness and cover opening sidewalls (to avoid charging)

13- Spin and cure E-beam pos. resist ZEP 520A and pattern trenches with EBL aligning the trenches to Au AMs

14- Etch Al and trenches in the ICP-RIE

15- Wet etch to remove excess Al

REFERENCES

[1] P. Rabiei, W. H. Steier, C. Zhang, and L. R. Dalton, “Polymer Micro-Ring Filters and Modulators” J. Lightwave. Techn., 20, 1968-1975, (2002)

[2] W.-Y. Chen, R. Grover, T. A. Ibrahim…..”High-Finesse Laterally Coupled Single-Mode Benzocyclobutene Microring Resonator”

[3] L. Zuo, H. Suzuki, K. Kong, J. Si, M.M. Aye, A. Watabe and S. Takahashi, “ Athermal silica based interferometer type planar lightewave circuits realized by a multicore fabrication method” Opt. Lett., 28, 1046-1048, (2003)

[4] T. P. White, C. M. de Streke, R.C. McPhedran, T. Huang, and L.C. Botton, “ Recirculation enhanced switching in photonic crystal Mach-Zehnder interferometers” Opt. Express, 12, 3035-3045, (2004)

[5] D.L. Lee,”Electromagnetic principles of integrated optics”, New York, John Wiley & Sons, (1986)

[6] C.T. Lee, M.L. Wu, “Apexes-Linked circle grating for low-loss waveguide bends”, IEEE photon. Technol. Lett., 13, 597-599, (2001)

[7] Pierre Pottier, Sara Masroiacovo, Richard M. De La Rue, “Power and polarization beam-splitters, mirrors and integrated interferometers based on air-hole photonic crystals and lateral large index-contrast waveguides”, Opt. Express, 12, 5617, (2006)

[8] Seunghyun Kim, Jianhua jiang, and Gregory P. Nordin, “Design of compact polymer Mach-Zender interferometer and ring resonator with air trench structures”, accepted in 2005 in Journal of Opt. Engineering

[9] Lixia Li, Gregory P. Nordin, Jennifer M. English, Jianhua Jiang, “Small-area bends and beamsplitters for lowindex-contrast waveguides”, Opt. Exp. Vol. 11, No. 3 (2003)

[10] Jaime Cardenas, Lixia Li, Seungyun Kim, Gregory P. Nordin, “ Compact low loss single air interface bends in polymer waveguides”, Opt. Express, 12, 5314-5324, (2004)

[11] John Ballato and Stephen H. Foulger, Dennis W. Smith, Jr.” Optical properties of perfluorocyclobutylpolymers. II. Theoretical and experimental attenuation” J. Opt. Soc. Am. B/Vol. 21, No. 5(2004)

[12] Michel Pons, Jacques Pelletier, and Olivier Joubert, “Anisotropic etching of polymers in SO_2/O_2 plasmas: Hypotheses on surface mechanisms”, J. Appl. Phys., Vol. 75, No. 9 (1994)

[13] http://www.clarycon.com/plasmaetchfundam.html

[14] Y. Lin, J. Cardenas, S. Kim, G.P. Nordin, “Reduced loss through improved fabrication for single air interface bends in polymer waveguides,” submitted to Op. Exp.

[15] Doo Gun Kim, Jae Hyuk Shin, Cem Ozturk, Jong Chang Yi, Younchul Chung, Nadir Dagli, “Total internal reflection mirror-base InGaAsP ring resonators Integrated with optical amplifiers”, IEEE photonics technology letters, 17, 1041-1135, (2005)

[16] Masayuki Izutsu, Yoshiharu Nakai, Tadasi Sueta, “Operation mechanism of the single-mode optical-waveguide Y junction”, Optics letters, 17, 136, (1982)

[17] K. K. Lee, D. R. Lim, L. C. Kimerling, J. Shin, and F. Cerrina, “Fabrication of ultralow-loss Si/SiO_2 waveguide by roughness reduction”, Opt.Lett., 26, 1888-1890, (2001)

[18] K.K. Lee, D. R. Lim, H. C. Luan, A. Anu, J.Foresi, L.C. Kimerling, “Effect of size and roughness on light transmission in a Si/SiO_2 Waveguide: Experiments and model”, Appl. Phys. Lett., 77, 1617-1619, (2000)

[19] C.Manolatou, Steven G. Johanson, Shanhui Fan, Pierre R. , Villeneuve, H. A. Haus, J. D. Joannopoulos, “High-Density Integrated Optics”, Lightwave Technology, 17, 1682, (1999)

[20] W. Lorattanaruangkit et al, Proc. Asia- Pacific Microwave Conference 1183, (2003)

[21] Shoji Akiyama, Milos A. Popovic, Peter T. Rakich, Kazumi Wada, Jurgen Michel, Hermann A. Haus, Erich P. Ippen, Lionel C. Kimerling, “Air trench bends and splitters for dense optical integration in low index contrast”, Lightwave technology, 23, 2271, (2005)

[22] Damian Goldring, Evgeny Alperovich, Uriel Levy, David Mendlovic, “Analysis of waveguide-splitter-junction in high-index Silicon-On-Insulator waveguides”, Opt. Express, 13, 2931, (2005)

[23] B. E. Little, S. T. Chu, W. Pan, D. Ripin, T. Kaneko, Y. Kokubun, and E. Ippen, “Vertically Coupled Glass Microring Resonator Channel dropping Filter,” Photonic Technology Letters, 21, 215 (1999)

[24] P. Rabiei, W. H. Steier, C. Zhang, and L. R. Dalton, “Polymer Micro-Ring Filters and Modulators,” *J. Lightwave. Techn.*, 20, 1968-1975, (2002).

[25] W. Y. Chen, R. Grover, T. A. Ibrahim, V. Van, W. N. Herman and P. T. Ho, “High Finesse Laterally Coupled Single-Mode Benzocyclobutane Microring Resonators, ” Photonic Technology Letters, 16, 470, (2004)

[26] Y.Lin, J.Cardenas, S.Kim, G.P. Nordin, “Reduced loss through improved fabrication for single air interface bends in polymer waveguides,” submitted to Op. Exp.

[27] L. Eldada,, L.W. Shacklette "Advances in polymer integrated optics", IEEE Journal of Selected Topics in Quantum Electronics 6 (1), 54 - 68 (2000).

[28] S.M. Garner, Sang-Shin Lee, V. Chuyanov, A. Chen, A. Yacoubian, W.H. Steier, L.R. Dalton, "Three-dimensional integrated optics using polymers", IEEE Journal of Quantum Electronics 35 (8), 1146 - 1155 (1999).

[29] U. Siebel, R. Hauffe, K. Petermann, "Polymer digital optical switch with an integrated attenuator", IEEE Photonics Technology Letters 13 (9), 957-959 (2001).

[30] Jae-Wook Kang; Jae-Pil Kim; Won-Young Lee; Joon-Sung Kim; Jae-Suk Lee; Jang-Joo Kim, "Low-loss fluorinated poly(arylene ether sulfide) waveguides with high thermal stability", Journal of Lightwave Technology 19 (6), 872-875 (2001).

[31] Dennis W. Smith Jr, Shengrong Chen, Suresh M. Kumar, John Ballato, Chris Toppind, Hiren V. Shah, and Stephen H. Foulger "Perfluorocyclobutyl Copolymers for Microphotonics", Advanced material 14 (21), 1585-1589 (2002).

[32] John Ballato, Dennis W. Smith, Jr, Stephen Foulger "Optical properties of perfluorocyclobutyl polymers", J. Opt. Soc. Am. 20 (9), 1838-18 43 (2003).

[33] Lixia Li, Gregory P. Nordin, Jennifer M. English, Jianhua Jiang, "Small-area bends and beamsplitters for low-index-contrast waveguides", Opt. Express 11**,** 282-290 (2003).

[34] D. Fuard, O. Joubert, L. Vallier, and M. Bonvalot "High density plasma etching of low k dielectric polymers in oxygen-based chemistries", J. Vac. Sci. Technol. B 19(2), 447-455 (2001).

[35] Con gchun Zhang, Chunsheng Yang and Duifu Ding "Deep reactive ion etching of commercial PMMA in O2/CHF3 and O2/Ar-based discharges", Journal of Micromechanics and Microengineering 14, 663-666 (2004).

[36] B. Schuppert, E. Brose, and K. Petermann "Anisotropic plasma etching of polymers using a cryo-cooled resist mask", J. Vac. Sci. Technol. A 18 (2), 385-387 (2000).

[37] Kwansoo Han, Junghee Kim, Woo-Hyuk Jang, "Evaluation of Halogenated Polyimide Etching for Optical Waveguide Fabrication by Using Inductively Coupled Plasma", Journal of Applied Polymer Science 79, 176-182 (2001).

[38] M. R. Baklanov, S. Vanhaelemeersch, H. Bender and K. Maex, "Effects of oxygen and fluorine on the dry etch characteristics of organic low-k dielectrics", J. Vac. Sci. Technol. B 17 (2), 372-379 (1999).

[39] R. R. A. Syms and J. Cozens, *Optical Guided Waves and Devices*, New York: McGraw Hill, ch. 6, 120-144, (1992).

[40] J. Cai, G. P. Nordin, S. Kim, and J. Jiang, "Three-dimensional analysis of a hybrid photonic crystal-conventional waveguide 90° bend," Appl. Opt., 43(21), 4244-4249, (2004).

[41] W. –Y. Chen, R. Grover, T. A. Ibrahim, V. Van, W. N. Herman, and P. –T. Ho, "High-Finesse Laterally Coupled Single-Mode Benzocyclobutene Microring Resonators," IEEE Photon. Tech. Lett., 16, 470-472, (2004).

[42] L. Zuo, H. Suzuki, K. Kong, J. Si, M. M. Aye, A. Watabe, and S. Takahashi, "Athermal silica-based interferometer-type planar light-wave circuits realized by a multicore fabrication method," Opt. Lett., 28, 1046-1048, (2003).

[43] W. M. J. Green, R. K. Lee, G. A. DeRose, A. Scherer, and A. Yariv, "Hybrid InGaAsP-InP Mach-Zehnder Racetrack Resonator for Thermooptic Switching and Coupling Control," Opt. Express, 13, 1651-1659, (2005).

[44] Kiyat, A. aydinli, and N. Dagli, "High-Q silicon-on-insulator optical rib waveguide racetrack resonators," Opt. Express, 13, 1900-1905, (2005).

[45] Vorckel, M. Monster, W. Henschel, P. H. Bolivar, and H. Kurz, "Asymmetrically coupled silicon-on-insulator microring resonators for compact add-drop multiplexers," IEEE Photon. Technol. Lett., 15, 921-923, (2003).

[46] Yeniay, R. Gao, K. Takayama, R. Gao, and A. F. Garito, "Ultra-low-loss polymer waveguides," J. Lightwave Techn., 22, 154-158, (2004).

[47] W. Bogaerts, D. Taillaert, B. Luyssaert, P. Dumon, J. V. Campenhout, P. Bienstman, D. V. Thourhout, and R. Baets, "Basic structures for photonic integrated circuits in Silicon-on-insulator," Opt. Express, 12, 1583-1591, (2004).